Molecular catalytic system for efficient water splitting

Joya, K.S.

Molecular Catalytic System for Efficient Water Splitting

Khurram Saleem Joya

Molecular Catalytic System for Efficient Water Splitting

Khurram Saleem Joya

Printed by Wöhrmann Print Services, Zutphen

ISBN:

Molecular Catalytic System for Efficient Water Splitting

Proefschrift

ter verkrijging van
de graad van Doctor aan de Universiteit Leiden,
op gezag van Rector Magnificus prof. mr. P. F. van der Heijden,
volgens besluit van het College voor Promoties
te verdedigen op woensdag 21 december 2011
klokke 10.00 uur

door

Khuram Saleem Joya
geboren te Lahore, Pakistan
in 1979

Promotiecommissie

Promotor:	Prof. dr. H.J.M. de Groot
Overige leden:	Prof. dr. J. Brouwer Prof. dr. M.T.M. Koper Dr. F. Buda Prof. dr. J.N.H. Reek (University of Amsterdam)

This research work was performed with financial support of the Higher Education Commission (HEC), Government of Pakistan.

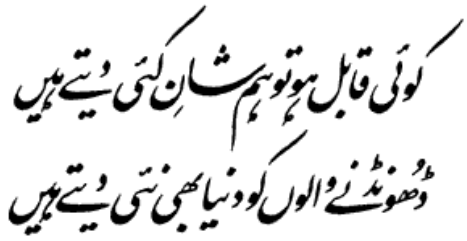

On him who merits well, We set the brightest diadem,
And those who truly questing come, a new world waits for them.

(Dr. M. Iqbal)

To my mother and my father

With love to my family

Table of Contents

Chapter 1

Introduction to Molecular Complexes for Catalytic Water Splitting

ABSTRACT

During the last few decades, the scientific community has been striving hard to develop new and alternative sources for renewable energy and fuel. Hydrogen or carbon neutral fuels obtained from catalytic water splitting using sunlight offer an attractive solution for a cleaner and greener future. In this pursuit, to establish a simple and superior catalytic system for efficient water oxidation is considered to be a bottleneck, hampering the design, implementation and exploitation of electrochemical and photo-electrochemical devices for light driven energy conversion into hydrogen or low carbon based storable fuels. From metal oxides to composite materials, noble metal complexes to transition metal organometallics, multinuclear to mono site catalysts, various water oxidation complexes (WOC) have been investigated both in a homogeneous environment and on surfaces in photo- or electrochemical conditions. However, a true catalytic system for efficient water splitting, operating with four consecutive proton coupled electron transfer (PCET) steps to generate oxygen and hydrogen with high turnover number (TON) and frequency (TOF) is yet to be achieved. In this introductory chapter an overview is presented for molecular complexes that have been investigated for water oxidation catalysis in homogeneous solution using chemical oxidants, or as heterogeneous species in catalytic electrochemical systems.

Based on: K.S. Joya and H.J.M. de Groot, *Int. J. Hydrogen Energy*, **2011** (*in revision*)

1.1. BACKGROUND

Renewable energy in connection with global environmental change has become an increasingly vital and burning subject, both in political communities and in science, in recent years [1-4]. Growth of the global population and the world economy is expected to double the world's power consumption by 2050 from the present demand of 13 TW [5-7]. On the other hand, the current level of CO_2, a green house gas, has exceeded 387 ppm due to increase in the combustion of carbon based fossil fuels in automobiles and power generation systems [8-10]. Petroleum, coal and natural gas are the primary energy carriers, while at the same time they are the principle sources of CO_2 emissions into the atmosphere [9,11].

Normally, electrons and protons are required to make renewable fuels and they can be obtained from oxidation of water, which is the one and only truly plentiful and attractive candidate to be used as a raw material. Therefore, the best possibility is to utilize abundant solar energy for the production of hydrogen and oxygen from catalytic water splitting [12-14]. At present, there is no efficient system available that makes use of solar energy effectively to produce hydrogen from water catalysis [15-18]. The most intricate task is to develop an easy accessible oxidation catalyst from earth abundant materials that is capable of multielectron water splitting and dioxygen generation at tremendous rate and activity [19,20].

Photosynthesis offers an excellent model for designing an artificial solar energy conversion system for clean fuel generation, where a tetra manganese oxygen evolving complex (OEC) is involved in the process of four electron water oxidation to generate dioxygen and release of four protons in a four step consecutive proton coupled electron transfer cycle. The overall four electron water oxidation reaction is given in Eq. (1):

$$2H_2O_{(l)} \rightarrow 4e^- + 4H^+_{(aq)} + O_{2(g)} \quad (1)$$

Electrons are provided to the reaction center of the photosystem II (PS-II) and ultimately appear as reduced carbon derived products by this process, which is the origin of all biological activities [21]. Thermodynamically, the overall free energy change for the four steps in the tetraelectron water splitting process amounts to 4.92 eV, and the ideal catalyst would exhibit a Gibbs free energy change (ΔG) of 1.23 eV for each step [22]. Assuming the water as the zero point of the energy scale, the Gibbs energies for HO*, O*, and HOO* intermediates (where * represents the catalytic site) generated during ideal catalysis, would be 1.23 eV, 2.46 eV, and 3.69 eV respectively [22,23].

In acidic medium in contact with the catalytic site, the water oxidation proceeds according to the following mechanism (Eqs. 1.1-1.4):

$$2H_2O_{(l)} + [Cat\text{-}(OH_2)]^{2+} \rightarrow [Cat\text{-}(OH)]^{2+} + 2H_2O_{(l)} + H^+ + e^- \quad (1.1)$$

$$\rightarrow [Cat(=O)]^{2+} + 2H_2O_{(l)} + 2(H^+ + e^-) \quad (1.2)$$

$$\rightarrow [Cat\text{-}(OOH)]^{2+} + H_2O_{(l)} + 3(H^+ + e^-) \quad (1.3)$$

$$\rightarrow [Cat\text{-}(OO)]^{2+} + H_2O_{(l)} + 4(H^+ + e^-) \rightarrow [Cat\text{-}(OH_2)]^{2+} + O_{2(g)} + 4(H^+ + e^-) \quad (1.4)$$

Variation of the pH changes the chemical potential of the protons at the catalytic site, and in an alkaline environment the reaction proceeds according to following pathway (Eqs. 1.5-1.8):

$$4OH^- + [Cat\text{-}(OH_2)]^{2+} \rightarrow [Cat\text{-}(OH)]^{2+} + H_2O_{(l)} + 3OH^- + e^- \quad (1.5)$$

$$\rightarrow [Cat(=O)]^{2+} + 2H_2O_{(l)} + 2OH^- + 2e^- \quad (1.6)$$

$$\rightarrow [Cat\text{-}(OOH)]^{2+} + 2H_2O_{(l)} + OH^- + 3e^- \quad (1.7)$$

$$\rightarrow [Cat\text{-}(OO)]^{2+} + 3H_2O_{(l)} + 4e^- \rightarrow [Cat\text{-}(OH_2)]^{2+} + O_{2(g)} + 2H_2O_{(l)} + 4e^- \quad (1.8)$$

A recent X-ray analysis of the photosystem-II has revealed some new structural features showing a water network around PS-II possibly involved in proton channeling from the manganese cluster to the reduction site [24]. Getting inspired from natural principles, there is a continuous effort to design an artificial

photosynthetic assembly based upon harnessing the solar energy and capable of utilizing it efficiently to generate oxygen and hydrogen for water splitting [25,26]. A major task is to establish an efficient and stable oxygen evolving catalyst that displays multielectron oxidation activity for hundred thousands of cycles [27]. There are many water splitting systems based on noble metal complexes, organometallics and inorganic metal oxide catalysts, but none of them have proven good overall efficiency for water splitting [28,29].

In this opening introductory chapter, the advent of molecular catalysts, both mono-site and multi nuclear organometallic complexes, is described, for water oxidation in homogeneous solution, as heterogeneous species using a chemical oxidant and in catalytic electrochemical systems on inert electrode surfaces.

1.2. MOLECULAR COMPLEXES FOR WATER SPLITTING

1.2.1. Early Evolution of Water Oxidation Complexes

The photosynthetic oxygen evolving complex is known to consist of a tetramanganese-oxo cluster active site that is responsible for efficient catalytic water splitting and rapid evolution of oxygen [30]. A number of structures of PS II has been reported, down to 2.9 A° resolution [31-33]. These structures have provided new information on the arrangement of protein subunits and cofactors, but the resolution is not sufficient to reveal the intimate details of the catalytic water splitting centre. The most detailed structure of the OEC of PS II reveals five oxygen atoms serving as oxo-bridges connecting five metal atoms (four Mn and one Ca) and four water molecules bound to the Mn_4CaO_5 cluster [24]. About 1300 water molecules were found in PS-II, providing extensive hydrogen-bonding networks that may serve as channels for protons, water or oxygen molecules.

The quest for a synthetic catalytic water oxidation system began in the 70's with photochemical studies on a di-μ-oxo bridged dinuclear manganese (Mn^{III}-Mn^{IV}) 2,2′-bipyridine (bpy) complex by M. Calvin (Fig. 1.1a), who was awarded

the Noble Prize in chemistry for the discovery of the Calvin-Benson Cycle, in 1961 [34].

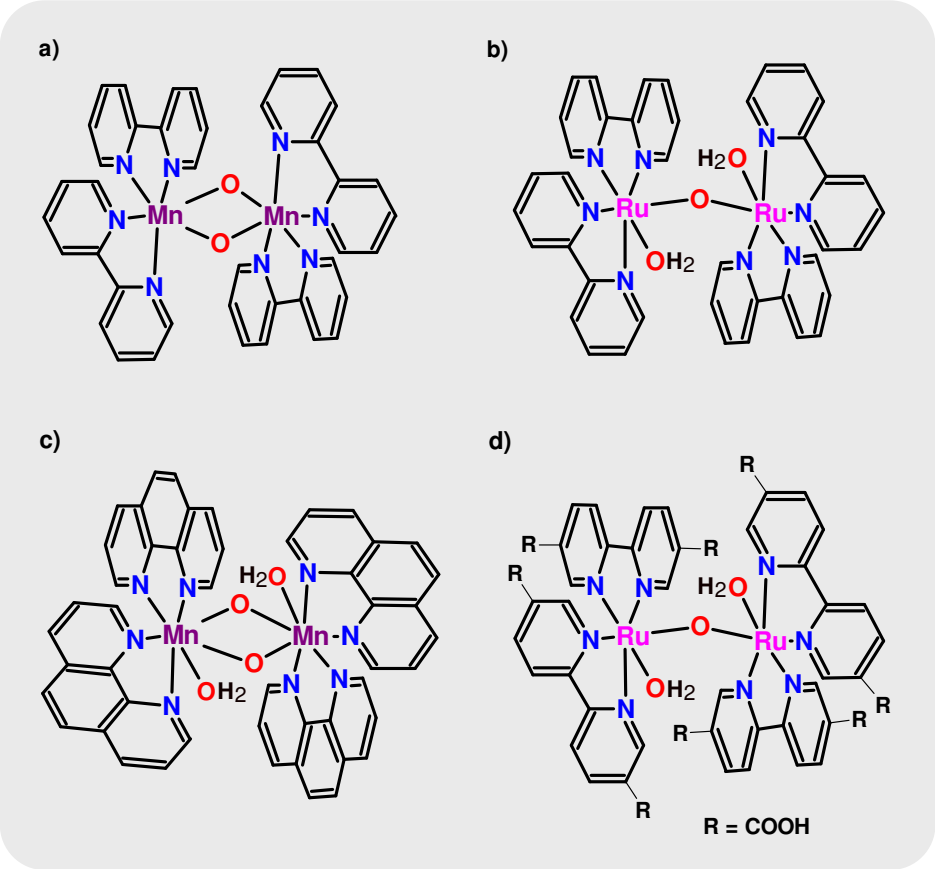

Figure 1.1. Molecular complexes that were proposed as water splitting catalysts at an early stage: **(a)** A binuclear bpy-manganese dimer $[(bpy)_2Mn^{III}(\mu\text{-}O\text{-})_2Mn^{IV}(bpy)_2]^{3+}$; **(b)** the blue dimer $[(bpy)_2Ru^{III}(\mu\text{-}O\text{-})\ Ru^{III}(bpy)_2]^{4+}$, (bpy = 2,2′-bipyridine); **(c)** a phenanthroline di-manganese complex $[(phen)_2Mn^{III}(\mu\text{-}O\text{-})_2Mn^{IV}(phen)_2]^{3+}$ (phen = 1,10-phenanthroline) and **(d)** the dicarboxy-bpy derived $[(R_2\text{-}bpy)_2Ru^{III}(\mu\text{-}O\text{-})Ru^{III}(R_2\text{-}bpy)_2]^{4+}$ binuclear ruthenium catalyst (R_2-bpy = 5,5′-dicarboxy-2,2′-bipyridine).

Later, it was realized that oxygen might have diffused from the atmosphere into the reaction vessel across the Teflon membrane and sensed by the oxygen electrode. As a result, the evidence of oxygen evolution by the manganese dimer complex, which was synthesized two years before as a novel antiferromagnetic

material, remained unclear [35,36]. This first effort was followed by the synthesis of a few dinuclear ruthenium and manganese based oxygen evolving complexes in the next decade (Fig. 1.1) with the same chemical composition of the dinitrogen ligands for the manganese and ruthenium catalysts [37].

1.2.2. Water Oxidation by Manganese Complexes

A well characterized synthetic tetra manganese complex, $Mn_4O_4L_6$ (L = diphenylphosphinate), with a Mn_4O_4 ($2Mn^{III}$, $2Mn^{IV}$) cubane-like core offered a new model of the active site of the photosynthetic water oxidation cluster [38]. It was followed by a synthetic di-terpyridine dimanganese complex, $[(terpy)(H_2O)Mn(\mu\text{-}O)_2Mn(terpy)(H_2O)]^{3+}$, the Mn-terpy dimer, (terpy = 2,2′:6′,2″-terpyridine), and was reported for homogeneous oxygen evolution (Fig. 1.2) in the presence of sodium hypochlorite [39,40]. The maximum turnover number of the di-terpyridine dimanganese complex for oxygen evolution was very low, and a TON=4 was determined in a solution containing sodium hypochlorite (NaClO) and using a one-electron Ce(IV) oxidant that ultimately led to the decomposition of the Mn dimer and the formation of permanganate ions after 6 hours of catalysis [39].

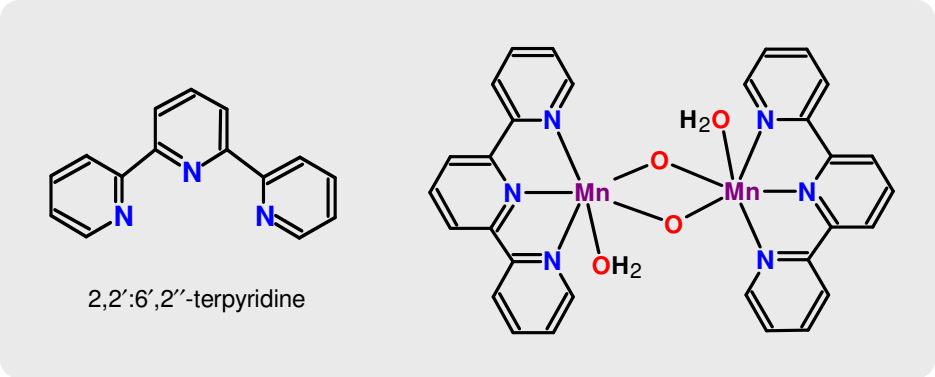

Figure 1.2. A 2,2′:6′,2″-terpyridine (terpy) derived di-μ-oxo di-terpy dimanganese diaqua water oxidation complex, $(terpy)(H_2O)Mn(\mu\text{-}O)_2Mn(terpy)(H_2O)]^{3+}$ (Mn-terpy dimer).

The water oxidation catalyzed by the Mn-terpy dimer complex in an aqueous phase using a Ce(IV) oxidant was also investigated by other groups, but no oxygen

evolution was observed [41,42]. The electrochemical oxidation of the Mn-terpy dimer leads to the formation of an inactive tetranuclear complex from the Mn^{IV}–Mn^{IV} state of the di-manganese catalyst, which confirms that it cannot act as a homogeneous catalyst for water oxidation [43]. Later, Yagi and Narita found that Mn-terpy dimer complexes in the presence of the Ce(IV) oxidant catalytically produce oxygen from water only when adsorbed on kaolin or mica [41]. The maximum TON's for oxygen evolution in heterogeneous conditions were 15-17, obtained in 4 days of continuous catalysis operation of the mica and kaolin adsorbed synthetic terpy-Mn-(μ-O)$_2$-Mn-terpy complex.

1.2.3. Ruthenium Based Water Oxidation Catalysts

A bi-ruthenium tetra aqua tetrakis-bipyridine $[(bpy)_2(H_2O)Ru^{III}(\mu\text{-}O)Ru^{III}(H_2O)(bpy)_2]^{4+}$ with a $Ru^{III}(\mu\text{-}O)Ru^{III}$ core, also known as blue dimer (Fig. 1.1b), is widely considered as the first genuine synthetic homogeneous water oxidation catalyst and was reported by Meyer's group in the early 1980s [44]. Its carboxylic acid substituted derivatives (Fig. 1.1d) are also found to be active for oxygen evolution [45,46]. The turnover frequency and TON's of the blue dimer were reported to be 4.2×10^{-3} per second [47] and 13.2 [48], respectively.

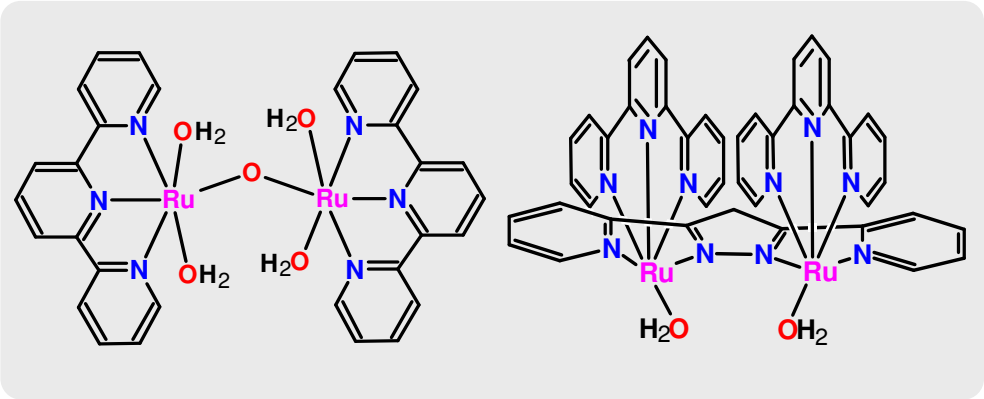

Figure 1.3. (left) A μ-oxo bridged di-terpyridine diruthenium complex, $[(terpy)(H_2O)Ru(\mu\text{-}O)Ru(terpy)(H_2O)]^{4+}$ (terpy = 2,2′:6′,2″-terpyridine) and **(right)** a di-terpyridine diruthenium complex with Hbpp bridging ligand $[Ru_2^{II}(bpp)(terpy)_2(H_2O)_2]^{3+}$, [(Hbpp = 2,2′-(1H-pyrazole-3,5-diyl)bis(pyridine)), for homogeneous water oxidation.

A tetra aqua Ru-terpy dimer $[(terpy)(H_2O)_2Ru(\mu\text{-}O)Ru(terpy)(H_2O)_2]^{4+}$ was synthesized and characterized for homogeneous water splitting in 1998 [49]. The structure was similar to that of the manganese analogue [39] except that it contained only one μ-oxo bridge between two ruthenium centers. Each metal center was ligated to two water molecules and the catalyst deactivated already after 1 turnover (Fig. 1.3). The first structurally and electrochemically well-characterized dinuclear Ru complex with a Hbpp type bridging mode, the terpy-Ru-bpp dimer $[Ru_2^{II}(bpp)(terpy)_2(H_2O)_2]^{3+}$ (Hbpp = 2,2′-(1H-pyrazole-3,5-diyl)bis(pyridine), instead of a Ru-O-Ru motif, was introduced by Llobet and co-workers (Fig. 1.3). Here two Ru metals were deliberately placed in close proximity using a double dinucleating ligand [50].

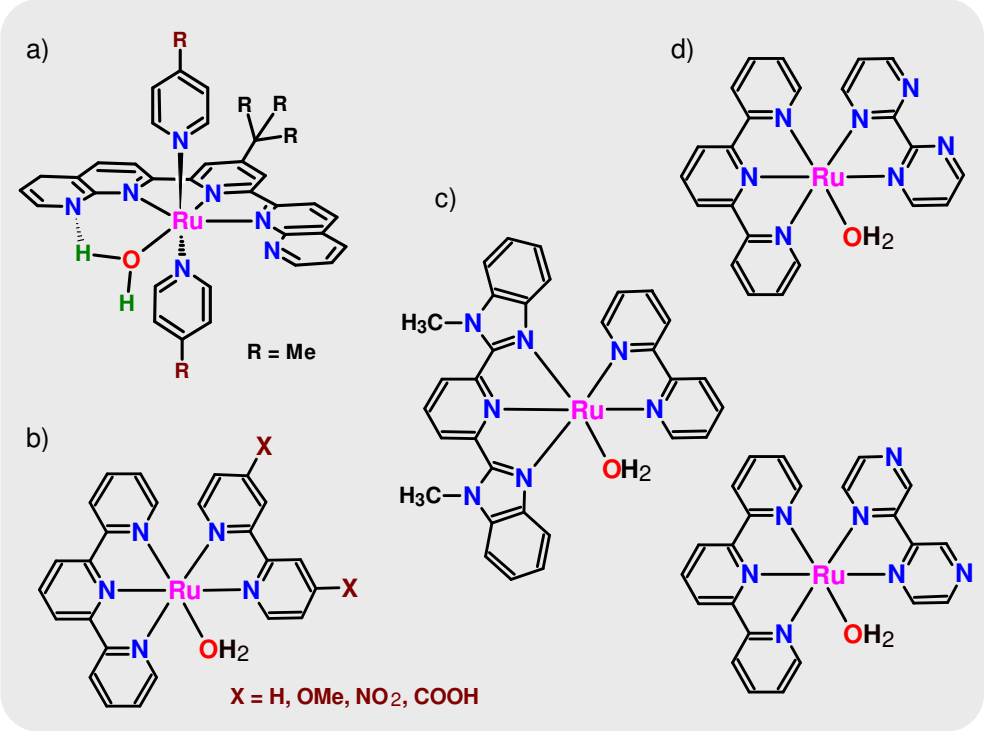

Figure 1.4. (a) A mono ruthenium 4-*tert*-Butyl-2,6-di([1′,8′]-naphthyrid-2′-yl)pyridine based complex introduced in 2005 followed by **(b)** terpy-Ru derived substituted bpy type single Ru catalysts; **(c)** replacement of the terpy ligand with a more bulky 2,6-bis(1-methylbenzimidazol-2-yl)-pyridine (Mebimpy) ligand and **(d)** introduction of tetraaza bpm (2,2′-bipyrimidine) and bpz (2,2′-bipyrazine) type ligands to the Ru-terpy motifs [51-54].

The absence of the μ-oxo bridge in the terpy-Ru-bpp dimer avoids the decomposition and makes it more active than the blue dimer for homogeneous oxygen evolution. Thummel *et al.* introduced a new type of binuclear [51] and a variety of single site ruthenium derived water oxidation complexes [51,52]. A TON up to 600 was achieved in homogeneous solution using a chemical oxidant. In contrast, detailed mechanistic analyses of single-site catalysts with Ru-terpy containing 2,2′-bipyrimidine (bpm), 2,2′-bipyrazine (bpz) motifs [53] and with a 2,6-bis(1-methylbenzimidazol-2-yl)-pyridine (Mebimpy) ligand instead of terpy [54] showed that the TON does not exceed 15 in solution phase catalysis (Fig. 1.4).

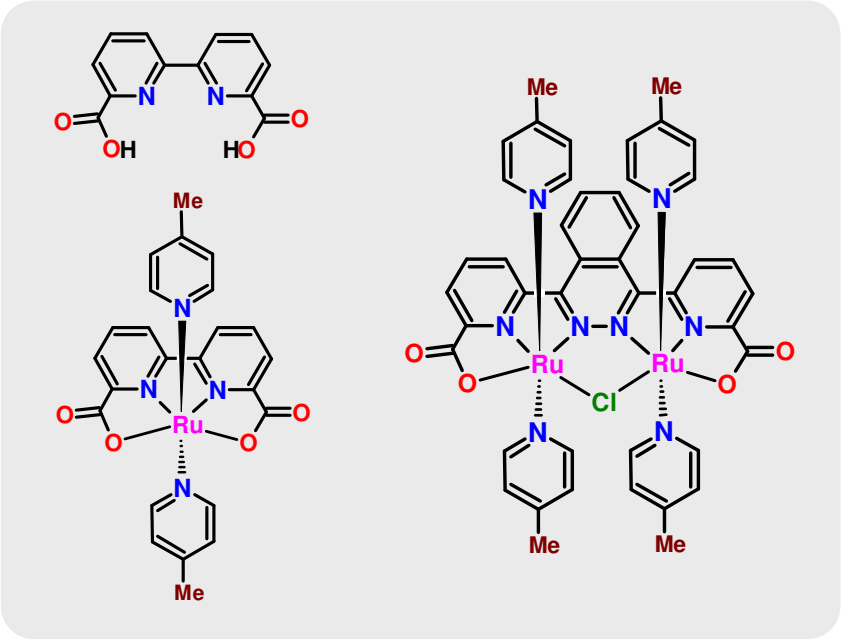

Figure 1.5. (left) A H_2dcabpy ligand derived mono site [(H_2dcabpy)Ru^{II}-(pic)] complex, (H_2dcabpy is 2,2′-bipyridine-6,6′-dicarboxylic acid; pic is 4-picoline) and **(right)** a dinucleating dicarboxylic modified ligand bis(capyptz) based dimeric ruthenium catalyst [bis(capyptz) = 1,4-bis(6′-COOH-pyrid-2′-yl)phthalazine)] [55,56].

Mono ruthenium complex with dicarboxylic acid substituted 2,2′-bpy and 1,10-phenanthroline (phen) ligands were recently studied using Ce(IV), and TON's up to 340 were obtained with TOF's of ~0.1 sec^{-1} [55]. The extended versions of the mono centre complex containing two ruthenium sites were also recently reported

for both chemical and light-driven water oxidation in homogeneous phase (Fig. 1.5). In the presence of an excess amount of Ce(IV), the dinuclear ruthenium complex bis(capyptz)-Ru_2-$(pic)_2$, [bis(capyptz) = 1,4-bis(6′-COOH-pyrid-2′-yl)phthalazine and pic is 4-picoline], produced 10,400 turnovers while generating approximately 20.7 µmol of molecular oxygen in 20 hours reaction time [56]. This is by far, the best TON obtained for a molecular ruthenium catalyst in homogeneous solution.

1.2.4. Iridium Complexes for Water Oxidation

A series of iridium organometallic complexes with general formula cis-$[Ir^{III}(L)_2(H_2O)_2]^+$, [L=2-(2-pyridyl)phenylate anion (2-ph-py)], and related ligands were reported to efficiently catalyze the water oxidation. Up to a TON of 2500 was obtained in the presence of Ce(IV) oxidant in acidic solution (pH <1), though the rate was lower than for the ruthenium analogues [57].

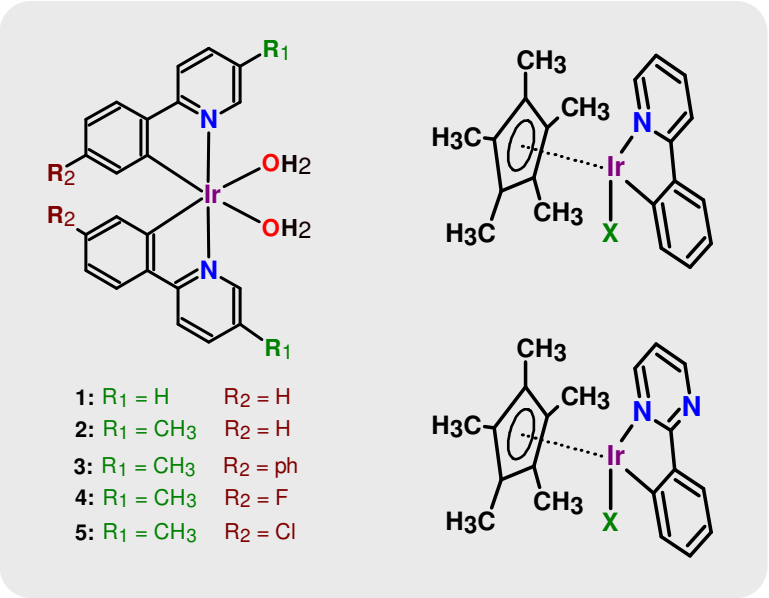

Figure 1.6. (left) Iridium derived $[Ir^{III}(L)_2(H_2O)_2]^+$ [L=2-(2-pyridyl)phenylate anion (2-ph-py)] water oxidation catalysts and **(right)** mono-site half sandwiched Cp*-iridium catalysts for homogeneous water oxidation (X = OTf or Cl).

Recently, Brudvig and Crabtree have prepared single site half sandwiched iridium complexes by combining relatively strong donating Cp* ligands (Cp* is pentamethylcyclopentadiene) with a 2-(2-pyridyl)phenylate type ligand (Fig. 1.6). With this new system, an oxygen generation rate of 0.9 sec^{-1} was achieved in the homogeneous phase [58]. In the next step the 2-ph-py type ligand was replaced with dinitrogen 2,2′-bipyridine, 2,2′-bipyrimidine and 1,10-phenanthroline ligands. To produce a catalytic complex the iridium centre was mono halogenated [59]. In such systems, the chloride at the metal catalytic site may get oxidized and OCl^{-5} or Cl_2 can be formed that may trigger O_2 evolution [58-61].

1.2.5. Other Molecular Oxygen Evolving Complexes

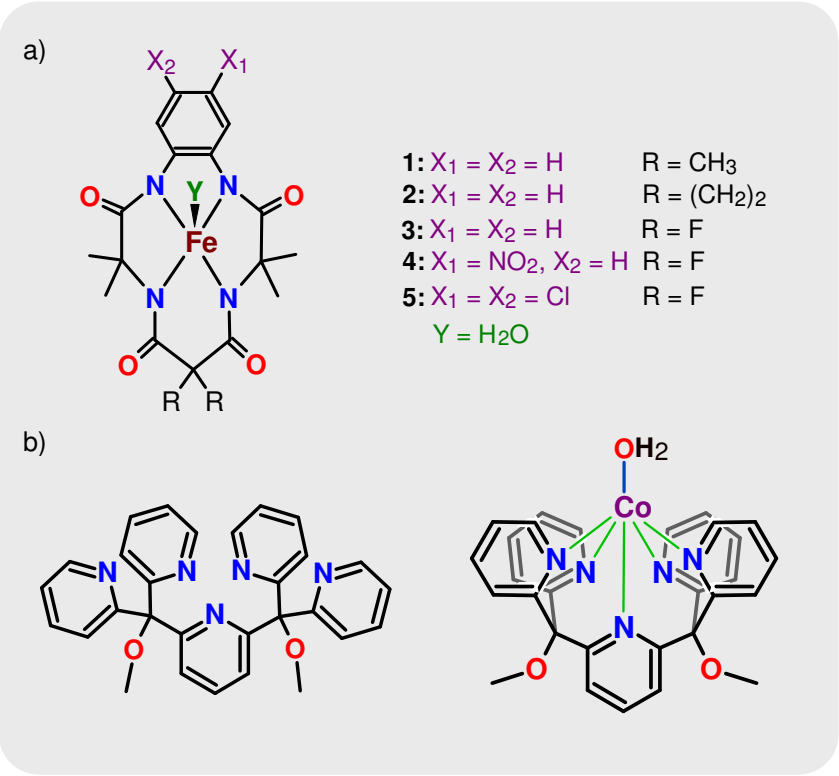

Figure. 1.7. A structural representation of **(a)** Fe^{III}-TAML (TAML = tetraamido macrocyclic ligand) derived complexes; **(b)** 2,6-(bis(bis-2-pyridyl)methoxy-methane)-pyridine (Py5) ligand and a mono cobalt-Py5 $[Co^{II}(Py5)(OH_2)]^{2+}$ complex.

Besides manganese, ruthenium and iridium derived molecular water splitting catalysts, other common transition metal based complexes have also been described that offer effective catalysis for oxygen generation in homogeneous systems [62]. A tetraamido macrocyclic ligand (TAML) based iron-centered complex Fe^{III}-TAML efficiently catalyzes the oxidative conversion of water to molecular oxygen in combination with ceric ammonium nitrate and reaches a turnover frequency of 1.3 per second [63]. A mono cobalt aqua complex with an oxidatively stable pentadentate Py5 ligand $[Co(Py5)(OH_2)](ClO_4)_2$, [Py5 = 2,6-(bis(bis-2-pyridyl)methoxy-methane)-pyridine], has shown catalytic activity for water oxidation in alkaline media (Fig. 1.7). Cyclic voltammetry analysis reveals that the mono cobalt system $[Co^{II}–OH_2]^{2+}$ proceeds by two consecutive PCET conversion steps, first into $[Co^{III}–OH]^{2+}/[Co^{II}–OH_2]^{2+}$ and then to $[Co^{IV}=O]^{2+}/[Co^{III}–OH]^{2+}$ redox couples. The mechanism of O-O bond formation was not yet resolved and is under investigation [64].

1.3. ELECTRO-ASSISTED CATALYTIC SYSTEMS FOR WATER SPLITTING

While there are many reports on solution phase homogeneous water oxidation catalysis, the number of studies involving surface electro-assisted water oxidation assemblies, which have applications in operational electrocatalytic or photo-electrocatalytic devices, is limited [54,65]. The first example of an electrode bound molecular complex appeared almost a decade ago, when a bis(ruthenium–hydroxo) complex, bearing a novel bridging type ligand, 1,8-bis(2,2′:6′,2″-terpyridyl)anthracene (btpyan), was employed in anodic water oxidation experiments (Fig. 1.8). The electrochemical investigation was conducted with the catalyst adsorbed on an indium-doped tin oxide (ITO) electrode at +1.7 V (vs. Ag/AgCl) in a pH=4 solution. More than 33,500 turnovers were obtained in 40 hours of electrolysis [66]. The initial current density was 0.12 mA/cm^2, which dropped significantly during the course of the experiment, indicating breakdown of the electrocatalytic complex [67]. More recently, a Ru(μ-O)Ru terpy dimer

modified with a phosphonate group for anchoring on oxide electrodes, $[(PO_3H_2\text{-terpy})(H_2O)_2Ru^{III}(\mu\text{-}O)Ru^{III}(H_2O)_2(PO_3H_2\text{-terpy})]^{4+}$, ($PO_3H_2$-terpy = 4′-phosphonato-2,2′:6′,2″-terpyridine), was synthesized for electrocatalytic studies of Ru-dimer-based water oxidation chemistry [49,68].

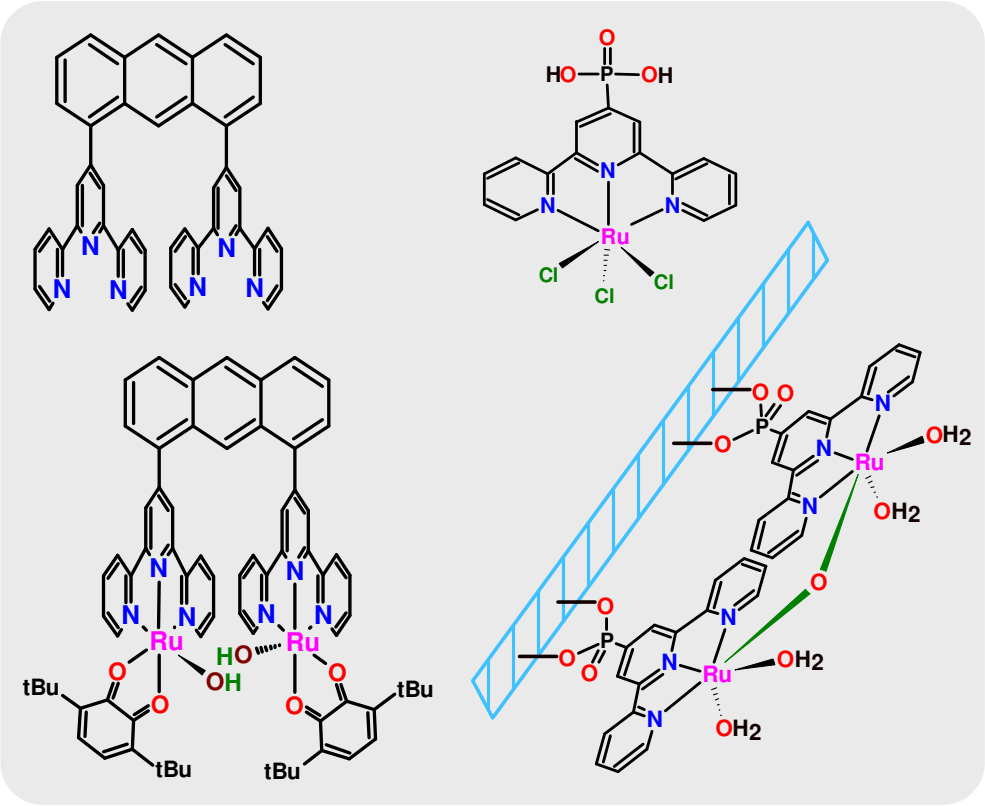

Figure 1.8. (left) A bis(ruthenium–hydroxo) complex, bearing a novel bridging type ligand 1,8-bis(2,2′:6′,2″-terpyridyl)anthracene (btpyan) and **(right)** a surface anchored Ru-terpy dimer $[(PO_3H_2\text{-terpy})(H_2O)_2Ru^{III}(\mu\text{-}O)Ru^{III}(H_2O)_2(PO_3H_2\text{-terpy})]^{4+}$ (PO_3H_2-terpy = 4′-phosphonato-2,2′:6′,2″-terpyridine) for electrocatalytic water oxidation.

The electrocatalytic water oxidation was carried out on catalyst modified ZrO_2 films on fluorine-doped tin oxide (FTO) at 1.5 or 1.25V (vs. Ag/AgCl) and a maximum TON of 3 was obtained with the complex in buffer solution at pH=6.

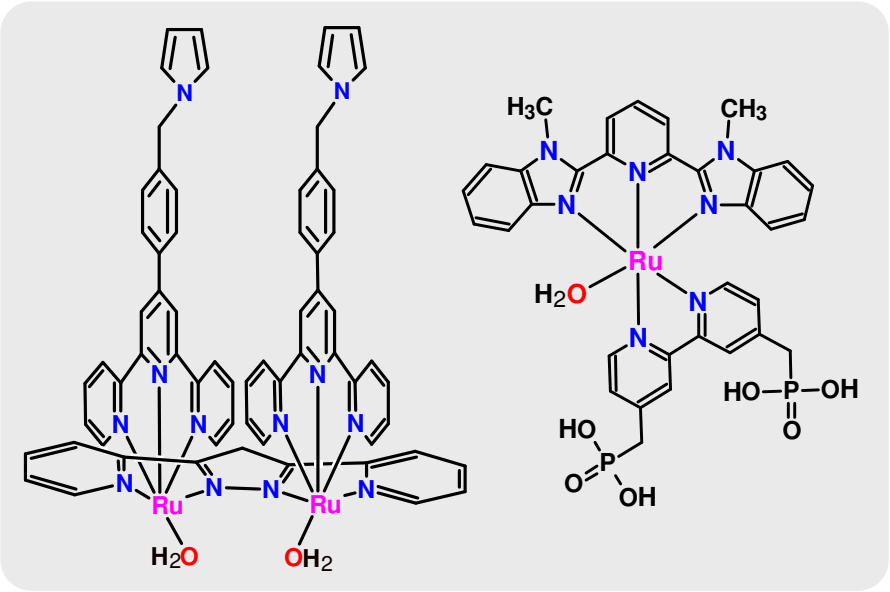

Figure 1.9. (left) A 4′-(para-pyrrolylmethylphenyl)-2,2′:6′,2″-terpyridine (t-terpy) based diruthenium complex with a Hbpp bridging ligand $[Ru_2^{II}(bpp)(t\text{-}terpy)_2(H_2O)_2]^{3+}$,(Hbpp = 2,2′-(1H-pyrazole-3,5-diyl)bis(pyridine), and **(right)** a mono site 2,6-bis(1-methylbenzimidazol-2-yl)-Pyridine (Mebimpy) ligand derived ruthenium complex for electrochemical water oxidation.

Meanwhile, Llobet and co-workers also extended their Hbpp-Ru terpy dimer with an electropolymerizable alkyl pyrrole linker to make a 4′-(para-pyrrolylmethylphenyl)-2,2′:6′,2″-terpyridine (t-terpy) based catalyst for electrochemical water oxidation (Fig. 1.9). The system was relatively efficient, with TON's exceeding 120 at 1.17 V potential (vs. Ag/AgCl) in 0.1 M aqueous triflic acid solution [69]. The extension of the Ru-bpy complex with a 2,6-bis(1-methylbenzimidazol-2-yl)-pyridine ligand was undertaken with the introduction of a 4,4′-dialkyl phosphonate (4,4′-$(H_2O_3PCH_2)_2$-bpy) as a catalytic linker to the 2,2′-bipyridine ligand (Fig. 1.9). Electrochemical water oxidation was detected at 1.85 V (vs. NHE) in pH=5 buffer. Very low turnover rate 0.004 sec^{-1} was observed, with a correspondingly low oxygen yield of 6.5 μmol during 30,000 seconds of the electrolysis run [54].

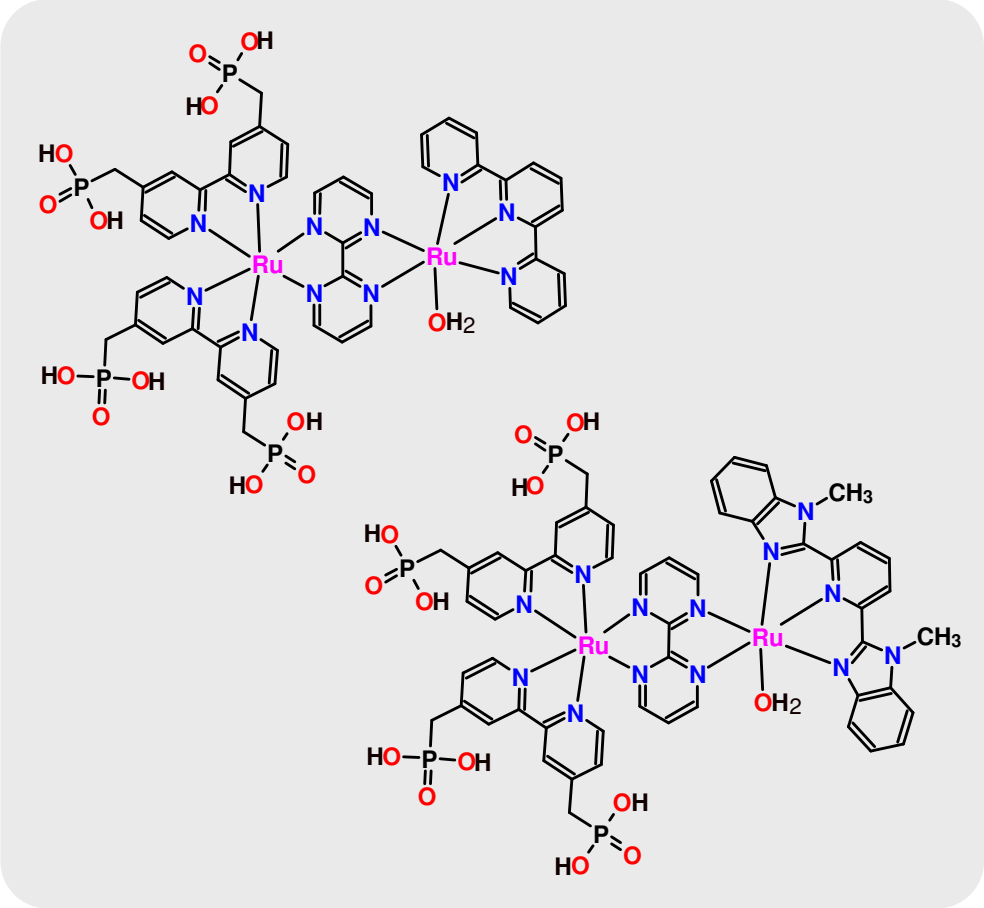

Figure 1.10. A 4,4′-$(H_2O_3PCH_2)_2$-bpy with Ru-tris-bpy type redox mediator modified **(left)** [(bpm)Ru^{II}(terpy)-(OH_2)] complex and **(right)** a [(bpm)Ru^{II}(Mebimpy)-(OH_2)] catalysts for the electrochemical water oxidation [70].

The incorporation of the 4,4′-$(H_2O_3PCH_2)_2$-bpy linker modified Ru-tris-bpy type redox mediator enhances the efficiency of the [(bpm)Ru^{II}(terpy)-(OH_2)] and [(bpm)Ru^{II}(Mebimpy)-(OH_2)] catalytic sites towards water oxidation (Fig. 1.10). In acidic medium at *ca*. 1.80 V (vs. NHE), 28000 turnovers were obtained for the [{4,4′-$(H_2O_3PCH_2)_2$-bpy}$_2$(bpm)Ru^{II}(Mebimpy)-(OH_2)]$^{4+}$ complex on ITO in 1.0 M aqueous $HClO_4$ at turnover rates of 0.6 sec^{-1} with very low current density >50 $\mu A/cm^2$ [70]. Very recently, a Cp*-Ir aqua or hydroxo catalyst (blue layer) was generated by anodic deposition in aqueous solution showing current densities up to

1.4 mA/cm^2 at ~1.4 V (vs. NHE) for water oxidation in 0.1M KNO_3 (pH=6) electrolyte solution [71]. This work suggested that organometallic species may be employed as useful precursors in electro-deposition of inorganic heterogeneous catalysts on a fluorine-doped tin oxide electrode for water oxidation. Scanning electron microscopic (SEM) analysis reveals that the thickness of such electrodeposited films is between 1 and 2 μm, and the formation of oxides of iridium on the electrode during electro-deposition and the water oxidation cycle cannot be excluded and requires further experimentation.

1.4. MECHANISM OF WATER OXIDATION

1.4.1. Natural Photosynthesis

The formation of molecular oxygen in natural photosynthesis is realized by the extraction of four electrons and protons in a four-step proton coupled electron transfer regime from two water molecules at the Mn_4CaO_5 cluster embedded in the photosystem-II [72,73]. Before the oxygen is released, a stepwise increase of the oxidation state of the Mn^{n+} ions permits the accumulation and confinement of the required four oxidizing equivalents. There is no evidence for partial oxidation of water at an early stage in the reaction cycle [74-76]. The consecutive PCET steps enable the accumulation of four redox equivalents while avoiding high energy intermediates during the multi-electron water oxidation cycle [77,78]. Hence the PCET mechanism at the Mn-cluster in the PS-II is a key element for separating electrons and protons from water to produce oxygen with a low overpotential at a high rate for hundred thousands of cycles [78-80].

1.4.2. Artificial Oxygen Evolving Complexes

For mononuclear water oxidation catalysts the oxygen evolution activity is thought to be constrained by a minimum overpotential of ~0.4 V due to a fixed difference of 3.2±0.1 eV in the affinity between the HOO* and the HO* intermediates [22,72]. While many artificial water oxidation catalysts have been scrutinized for

dioxygen generation, detailed mechanistic insight into the reaction mechanisms is still lacking [81-83].

Scheme 1.1. Catalytic water oxidation pathway and dioxygen evolution mechanism by mono nuclear [(terpy)-Ru-(bpm)], [(terpy)-Ru-{$(H_2O_3PCH_2)_2$-bpy}] and [(Mebimpy) -Ru-{$(H_2O_3PCH_2)_2$-bpy}] complexes [54,89]. [terpy = 2,2′:6′,2″-terpyridine, bpm = 2,2′-bipyrimidine, $H_2O_3PCH_2)_2$-bpy = 4,4′-$(H_2O_3PCH_2)_2$-2,2′-bipyridine and Mebimpy = 2,6-bis(1-methylbenzimidazol-2-yl)-pyridine].

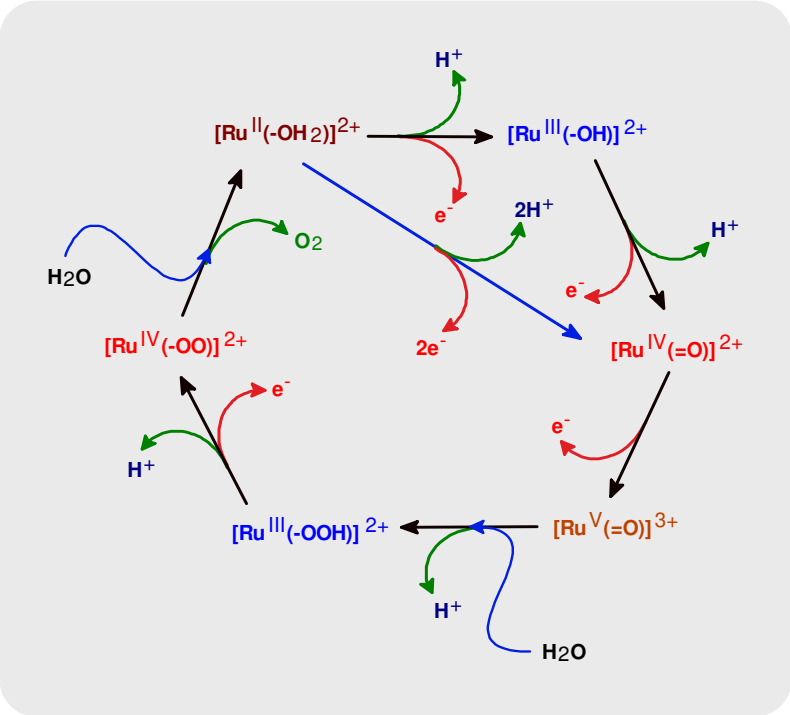

For example, several manganese complexes have been described but the mechanism of O-O bond formation is not yet clear [84-86]. In binuclear ruthenium systems the formation of oxygen is realized either by intramolecular O-O bond formation through oxo-oxo coupling at two catalytic sites without HOO* generation, which is prone to catalytic deactivation after a few cycles [87], or by nucleophilic OH_2 attack, generating a higher energy HOO* intermediate in a non-PCET step [88]. Recently reported mono-site ruthenium catalysts are not able to operate along a four step PCET reaction coordinate [18]. The HOO* intermediate

is formed at high overpotential from $[Ru^{V}=O]^{3+}$ type complex (Scheme 1.1) that is generated by an electron removal from $[Ru^{IV}=O]^{2+}$ in a non-PCET rate limiting step [54,89]. Moreover, in the few reports on iridium derived complexes for homogeneous water oxidation catalysis only speculative oxygen formation pathways have been put forward due to lack of experimental evidence, and more investigation is needed to provide insight into the mechanisms of operation [59,90].

1.5. CURRENT SCENARIO AND CHALLENGES

Catalytic water splitting offers an attractive potential solution for the production of environmentally clean energy carriers obtained from renewable materials and abundant solar energy [91,92]. Synthesis and design of complex water oxidation structures, and implementation in a stable four-electron transfer catalytic system, running at high catalytic turnover number and frequency for oxygen evolution, with low activation barrier, moderate overpotential and high current density, remain major challenges in this field [92-95]. A key issue is to devise a molecular complex that exhibits a consecutive proton coupled electron transfer regime during the multi-electron water oxidation cycle. It should be able to efficiently separate electrons and protons from water to produce oxygen with a high rate and sustain production for many hundred thousands of catalytic cycles [94-97]. In addition, the available immobilized oxygen evolving assemblies perform the water oxidation at high overpotential with very small current densities. This hampers their exploitation in electrolysis assemblies and photocatalytic devices for fuel generation [98,99].

1.6. AIM AND STRUCTURE OF THIS THESIS

The aim of this dissertation is to construct and explore artificial oxygen evolving complexes that are synthetically accessible, stable, functionally robust and efficient. To achieve this, a class of mono metal water splitting catalysts is introduced in this manuscript and exploitation of these complexes in homogeneous catalysis and in electrochemical studies with surface immobilized catalyst assemblies has been discussed. The catalysts are comprised of a single centre ruthenium or iridium metal core coordinated to a dinitrogen ligand and stabilized by a cyclic conjugated hydrocarbon (Figs. 1.11-1.13). Homogeneous catalytic water oxidation is performed with a chemical oxidant as catalyst activator. For electro-assisted experiments, the catalyst complexes are functionalized with carboxylic or phosphonic acid linker units on the dinitrogen ligand that serve as anchoring sites for deposition on conducting oxide electrodes.

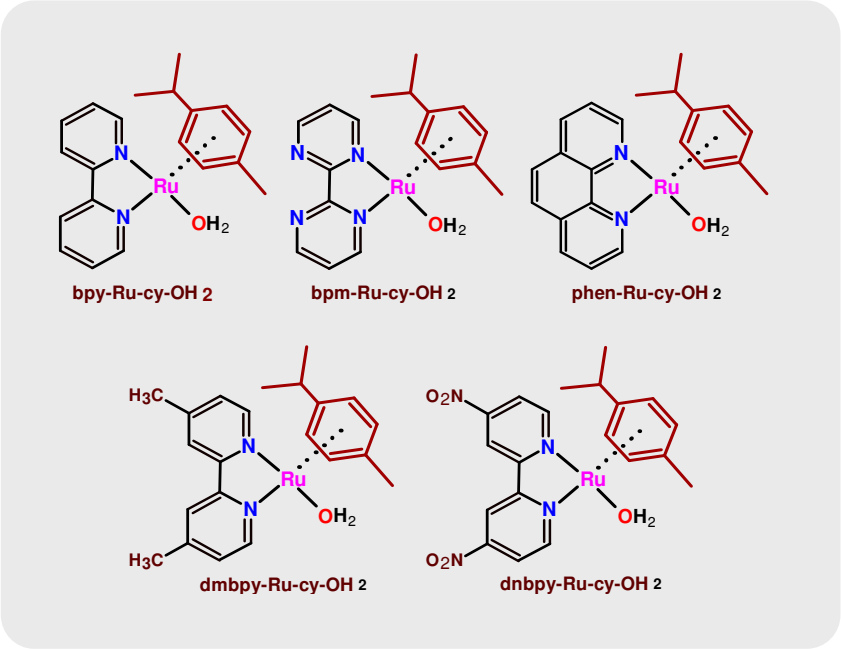

Figure 1.11. Ruthenium *p*-cymene (cy) derived simple and 4,4′-disubstituted-2,2′-bipyridine, 1,10-phenanthroline and 2,2′-bipyrimidine mono nuclear complexes.

The electrochemical methods for water oxidation are described in ***Chapter 2***. The Rotating Ring-Disk Electrode method and On-Line Electrochemical Mass Spectrometry technique, complemented with Surface-Enhanced Raman Spectroscopy, are employed to perform a model study for an existing catalytic system based on Ru-red in solution or adsorbed on the electrode surface.

In ***Chapter 3***, a set of mono site molecular ruthenium complexes is synthesized for homogeneous water splitting catalysis (Fig. 1.11). The complexes are easily accessible, stable in light and air, and appear to follow a four-step proton coupled electron transfer pathway for dioxygen formation.

The extension of the work regarding mono nuclear ruthenium complexes for surface immobilized electrocatalytic water splitting assemblies is described in ***Chapter 4*** (Fig. 1.12). The pH-dependent electrochemical characteristics and the enhancement of oxygen evolution efficiency and rate with the applied electrode potential are also discussed.

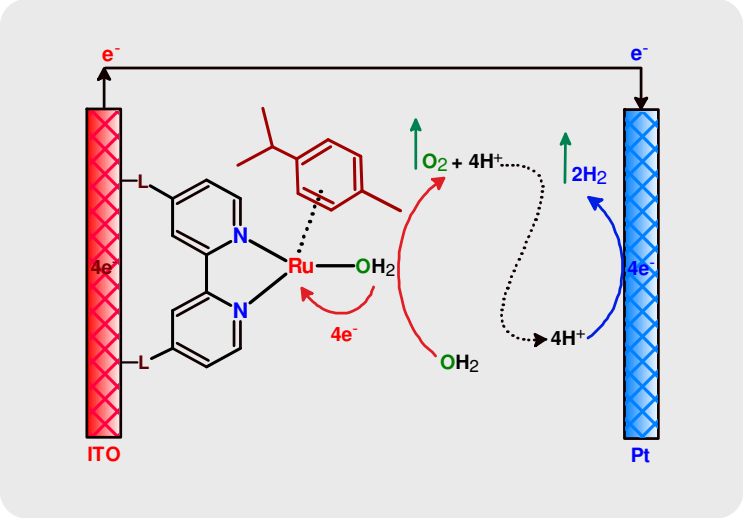

Figure 1.12. A schematic representation of the *p*-cymene-Ru derived 2,2′-bipyridine complexes for water oxidation. The catalyst (Cat.**Ru**–PO_3H_2 or Cat.**Ru**–COOH) is anchored on a conducting oxide surface via linker molecules (L = COOH or PO_3H_2) to drive electro-assisted water oxidation.

Chapter 5 shows the synthesis and catalytic properties of mono iridium complexes, both for homogeneous oxygen evolution catalysis and for surface anchored electro-assisted water oxidation on inert oxide electrodes (Fig. 1.13).

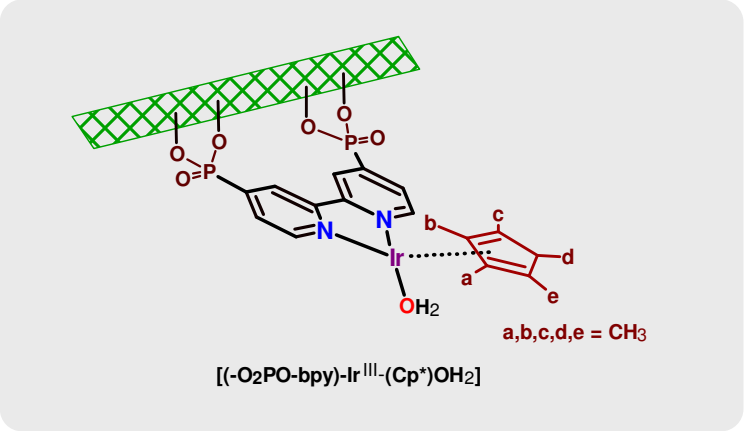

Figure 1.13. A mono iridium-Cp* complex immobilized on a conducting oxide surface (ITO) with linker (L = PO_3H_2) for electro-assisted water oxidation.

Chapter 6 at the end of the thesis describes how this project leads to a future perspective on water splitting catalysis systems for solar fuels generation. Several possibilities, such as the implementation of dinuclear catalysts, or a chromophore sensitized water oxidation system and integrated stand-alone assembly, the "Artificial Leaf", are proposed as future scenarios for the further extension and development of this work. This discussion is followed by a short summary of this dissertation.

REFERENCES

01- A. J. Bard and M. A. Fox, *Acc. Chem. Res.* **1995**, *28*, 141–145.

02- J. Chow, R. J. Kopp and P. R. Portney, *Science* **2003**, *302,* 1528–1531.

03- T. N. Verziroglu and F. Barbir, *Int. J. Hydrogen Energy* **1992**, *17*, 391–404.

04- N. S. Lewis, *Nature* **2001**, *414,* 589–590.

05- J. E. Funk, *Int. J. Hydrogen Energy* **2001**, *26*, 185–190.

06- N. S. Lewis and D. G. Nocera, *Proc. Natl Acad. Sci. USA* **2006**, *103*, 15729–15735.

07- R. M. N. Yerga, M. C. l. Galván, F. del Valle, J. A. V. de la Mano and J. L. G. Fierro, *ChemSusChem* **2009**, *2*, 471–485.

08- J. G. Canadell, C. Le Quéré, M. R. Raupach, C. B. Field, E. T. Buitenhuis, P. Ciais, T. J. Conway, N. P. Gillett, R. A. Houghton and G. Marland, *Proc. Natl. Acad. Sci. USA* **2007**, *104*, 18866–18870.

09- E. Brook, *Nature* **2008**, *453*, 291–292.

10- S. Piao, P. Ciais, P. Friedlingstein, P. Peylin, M. Reichstein, S. Luyssaert, H. Margolis, J. Fang, A. Barr, A. Chen, A. Grelle, D. Y. Hollinger, T. Laurila, A. Lindroth, A. D. Richardson and T. Vesala, *Nature* **2008**, *451*, 49–52.

11- G. Marland, T.A. Boden and R. J. Andres. **2007**. Global, Regional, and National CO_2 Emissions. In Trends: A Compendium of Data on Global Change.

12- L. Schlapbach, *Nature* **2009**, *460*, 809–811.

13- E. E. Barton, D. M. Rampulla and A. B. Bocarsly, *J. Am. Chem. Soc.* **2008**, *130*, 6342–6342.

14- T. J. Meyer, *Nature* **2008**, *451*, 778–779.

15- J. K. Hurst, *Coord. Chem. Rev.* **2005**, *249*, 313–328.

16- J. P. McEvoy and G. W. Brudvig, *Chem. Rev.* **2006**, *106*, 4455–4483.

17- P. Ritterskamp, A. Kuklya, M.-A. Wüstkamp, K. Kerpen, C. Weidenthaler and M. Demuth, *Angew. Chem. Int. Ed.* **2007**, *46*, 7770–7774.

18- Z. Deng, H.-W. Tseng, R. Zong and R. Thummel, *Inorg. Chem.* **2008**, *47*, 1835-1848.

19- M. M. Najafpour, T. Ehrenberg, M. Wiechen, M. and P. Kurz, *Angew. Chem. Int. Ed.* **2010**, *49*, 2233–2237.

20- A. Kudo and Y. Miseki, *Chem. Soc. Rev.* **2009**, *38*, 253–278.

21- M. Yagi and M. Kaneko, *Chem. Rev.* **2001**, *101,* 21–35.

22- J. Rossmeisl, K. Dimitrievski, P. Siegbahn and J. K. Nørskov, *J. Phys. Chem. C* **2007**, *111*, 18821–18823.

23- J. Rossmeisl, Z. W. Qu, H. Zhu, G.-J. Kroes and J. K. Nørskov, *J. Electroanal. Chem.* **2007**, *607*, 83–89.

24- Y. Umena, K. Kawakami, J.-R. Shen and N. Kamiya, *Nature* **2011**, *473*, 55-60.

25- J. T. Muckerman, D. E. Polyansky, T. Wada, K. Tanaka and E. Fujita, *Inorg. Chem.* **2008**, *47*, 1787–1802.

26- Á. Valdés, Z.-W. Qu, G.-J. Kroes, J. Rossmeisl and J. K. Nørskov, *J. Phys. Chem. C* **2008**, *112***,** 9872–9879.

27- L. Tong, L. Duan, Y. Xu, T. Privalov and L. Sun, *Angew. Chem. Int. Ed.* **2011**, *50*, 445–449.

28- L. Hammarström and S. Styring, *Phil. Trans. R. Soc. B* **2008**, *363*, 1283–1291.

29- C.W. Cady, R. H. Crabtree and G. W. Brudvig, *Coord. Chem. Rev.* **2008**, *252*, 444–455.

30- A. Guskov, J. Kern, A. Gabdulkhakov, M. Broser, A. Zouni and W. Saenger, *Nat. Struct. Mol. Biol.* **2009**, *16*, 334–42.

31- K. N. Ferreira, T. M. Iverson, K. Maghlaoui, J. Barber and S. Iwata, *Science* **2004**, *303***,** 1831–1838.

32- B. Loll, J. Kern, W. Saenger, A. Zouni and J. Biesiadka, *Nature* **2005**, *438* 1040–1044.

33- P. Joliot, *Photosyn. Res.* **2003**, *76*, 65–72.

34- M. Calvin, *Science* **1974**, *184*, 375–381.

35- M. Calvin, *Science* **1974**, *185*, 376.

36- P. M. Plaksin, R. C. Stoufer, M. Mathew, and G. J. Palenik, *J. Am. Chem. Soc.*, **1972**, *94*, 2121–2122.

37- H. Yamazaki, A. Shouji, M. Kajita and M. Yagi, *Coord. Chem. Rev.* **2010**, *254*, 2483–2491.

38- W. F. Ruettinger, C. Campana and G. C. Dismukes, *J. Am. Chem. Soc.* **1997**, *119,* 6670–6671.

39- J. Limburg, J. S. Vrettos, L. M. Liable-Sands, A. L. Rheingold, R. H. Crabtree and G.W. Brudvig, *Science* **1999**, *283*, 1524–1527.

40- J. Limburg, J. S. Vrettos, H. Y. Chen, J. C. de Paula, R. H. Crabtree and G. W. Brudvig, *J. Am. Chem. Soc.* **2001**, *123*, 423–424.

41- M. Yogi and K. Narita, *J. Am. Chem. Soc.* **2004**, *126*, 8084–8085.

42- P. Kurz, G. Berggren, M. F. Anderlund and S. Styring, *Dalton Trans.* **2007**, 4258–4258.

43- C. Baffert, S. Romain, A. Richardot, J.-C. Lepretre, B. Lefebvre, A. Deronzier and M.-N. Collomb, *J. Am. Chem. Soc.*, **2005**, *127*, 13694–13704.

44- S. W. Gersten, G. J. Samuels and T. J. Meyer, *J. Am. Chem. Soc.* **1982**, *104*, 4029–4032.

45- F. P. Rotzinger, S. Munavalli, P. Comte, J. K. Hurst, M. Graetzel, F.-J. Pern and A.J. Frank, *J. Am. Chem. Soc.* **1987**, *109*, 6619–6623.

46- P. Comte, M. K. Nazeeruddin, F. P. Rotzinger, A. J. Frank and M. Graetzel, *J. Mol. Catal.* **1989**, *52*, 63–69.

47- K. Nagoshi, S. Yamashita, M. Yagi and M. Kaneko, *J. Mol. Catal. A: Chem.* **1999**, *144*, 71–83.

48- J. P. Collin and J. P. Sauvage, *Inorg. Chem.* **1986**, *25*, 135–145.

49- E. L. Lebeau, S. A. Adeyemi and T. J. Meyer, *Inorg. Chem.* **1998**, *37,* 6476–6484.

50- C. Sens, I. Romero, M. Rodrıguez, A. Llobet, T. Parella and J. Benet-Buchholz, , *J. Am. Chem. Soc.*, **2004**, *126*, 7798–7799.

51- R. Zong and R. P. Thummel, *J. Am. Chem. Soc.* **2005**, *127*, 12802–12803.

52- H.-W. Tseng, R. Zong, J. T. Muckerman and R. Thummel, *Inorg. Chem.* **2008**, *47*, 11763–11773.

53- J. J. Concepcion, J. W. Jurss, J. L. Templeton and T. J. Meyer, *J. Am. Chem. Soc.*, **2008**, *130*, 16462–16463.

54- Z. Chen, J. J. Concepcion, J. W. Jurss and T. J. Meyer, *J. Am. Chem. Soc.* **2009**, *131*, 15580–15581.

55- (a) L. Duan, A. Fischer, Y. Xu and L. Sun, *J. Am. Chem. Soc.* **2009**, *131*, 10397–10399; (b) L. Tong, L. Duan, Y. Xu, T. Privalov and L. Sun, *Angew. Chem. Int. Ed.*, **2011**, *50*, 445 –449.

56- Y. Xu, A. Fischer, L. Duan, L. Tong, E. Gabrielsson, B. Akermark and L. Sun, *Angew. Chem. Int. Ed.* **2010**, *49*, 8934 –8937.

57- N. D. McDaniel, F. J. Coughlin, L. L. Tinker and S. Bernhard, *J. Am. Chem. Soc.* **2008**, *130*, 210–217.

58- J. F. Hull, D. Balcells, J. D. Blakemore, C. D. Incarvito, O. Eisenstein, G. W. Brudvig and R. H. Crabtree, *J. Am. Chem. Soc.* **2009**, *131*, 8730–8731.

59- J. D. Blakemore, N. D. Schley, D. Balcells, J. F. Hull, G. W. Olack, C. D. Incarvito, O. Eisenstein, G. W. Brudvig and R. H. Crabtree, *J. Am. Chem. Soc.* **2010**, *132*, 16017–16029.

60- J. A. Gilbert, D. S. Eggleston, W. R. Murphy, D. A. Geselowitz, S. W. Gersten, D. J. Hodgson and T. J. Meyer, *J. Am. Chem. Soc.* **1985**, *107*, 3855–3864.

61- M. Yagi, E. Tomita and T. Kuwabara, *J. Electroanal. Chem*. **2005**, *579*, 83–88.

62- D. K. Dogutan, R. McGuire and D. G. Nocera, *J. Am. Chem. Soc*. **2011**, *133*, 9178–9180.

63- W. C. Ellis, N. D. McDaniel, S. Bernhard and T. J. Collins, *J. Am. Chem. Soc*. **2010**, *132*, 10990–10991.

64- D. J. Wasylenko, C. Ganesamoorthy, J. Borau-Garcia and C. P. Berlinguette, *Chem. Commun.* **2011**, *47*, 4249–4251.

65- N. S. Lewis, *Nature*, **2001**, *414*, 589–590.

66- T. Wada, K. Tsuge and K. Tanaka, *Angew. Chem., Int. Ed. Engl.* **2000**, *39*, 1479–1482.

67- T. Wada, K. Tsuge and K. Tanaka, *Inorg. Chem.* **2001**, *40,* 329–337.

68- F. Liu, T. Cardolaccia, B. J. Hornstein, J. R. Schoonover and T. J. Meyer, *J. Am. Chem. Soc*. **2007**, *129*, 2446–2447.

69- J. Mola, E. Mas-Marza, X. Sala, I. Romero, M. Rodriguez, C. Viñas, T. Parella and A. Llobet, *Angew. Chem. Int. Ed*. **2008**, *47*, 5830–5832.

70- J. J. Concepcion, J. W. Jurss, P. G. Hoertz and T. J. Meyer, *Angew. Chem. Int. Ed*. **2009**, *48*, 9473–9476.

71- J. D. Blakemore, N. D. Schley, G. W. Olack, C. D. Incarvito, G. W. Brudvig and R. H. Crabtree, *Chem. Sci*. **2011**, *2*, 94–98.

72- H. Dau, C. Limberg, T. Reier, M. Risch, S. Roggan and P. Strasser, *ChemCatChem* **2010**, *2*, 724–761.

73- J. Yano, J. Kern, K. Sauer, M. J. Latimer, Y. Pushkar, J. Biesiadka, B. Loll, W. Saenger, J. Messinger, A. Zouni and V. K. Yachandra, *Science* **2006**, *314*, 821–825.

74- I. Zaharieva, J. M. Wichmann and H. Dau, *the Journal of Biological Chemistry* **2011**, *286*, 18222–18228.

75- L. Hammarström and S. Styring, *Phil. Trans. R. Soc. B* **2008**, *363*, 1283–1291.

76- H. Dau and M. Haumann, *Coord. Chem. Rev.* **2008**, *252*, 273–295.

77- M. H. V. Huynh and T. J. Meyer, *Chem. Rev.* **2007**, *107*, 5004–5064.

78- C. Costentin, M. Robert and J.-M. Savéant. *Acc. of Chem. Res*. **2010**, *43*, 1019–1029.

79- J. M. Mayer, *Ann. Rev. Phys. Chem*. **2004**, *55*, 363–390.

80- C. Costentin, *Chem. Rev*. **2008**, *108,* 2145–2179.

81- T. R. Cook, D. K. Dogutan, S. Y. Reece, Y. Surendranath, T. S. Teets, and D. G. Nocera, *Chem. Rev*. **2010**, *110,* 6474–6502.

82- T. J. Meyer, M. H. V. Huynh and H. H. Thorp, *Angew. Chem. Int. Ed*. **2007**, *46*, 5284–5304.

83- C. Herrero, B. Lassalle-Kaiser, W. Leibl, A. W. Rutherford and A. Aukauloo, *Coord. Chem. Rev.* **2008**, *252*, 456–468.

84- S. Mukhopadhyay, S. K. Mandal, S. Bhaduri and W. H. Armstrong, *Chem. Rev*. **2004**, *104,* 3981–4026.

85- W. Rttinger and G. C. Dismukes, *Chem. Rev*. **1997**, *97*, 1–24.

86- C. W. Cady, R. H. Crabtree and G. W. Brudvig, *Coord. Chem. Rev.* **2008**, *252*, 444–455.

87- S. Romain, F. Bozoglian, X. Sala and A. Llobet, *J. Am. Chem. Soc*. **2009**, *131*, 2768–2769.

88- J. J. Concepcion, M.-K. Tsai, J. T. Muckerman and T. J. Meyer, *J. Am. Chem. Soc*. **2010**, *132*, 1545–1557.

89- D. J. Wasylenko, C. Ganesamoorthy, M. A. Henderson, B. D. Koivisto, H. D. Osthoff and C. P. Berlinguette, *J. Am. Chem. Soc*. **2010**, *132*, 16094–16106.

90- N. D. Schley, J. D. Blakemore, N. K. Subbaiyan, C. D. Incarvito, F. D'Souza, R. H. Crabtree and G. W. Brudvig, *J. Am. Chem. Soc*. **2011**, *133*, 10473–10481.

91- C. S. Mullins and V. L. Pecoraro, *Coord. Chem. Rev*. **2008**, *252*, 416–443.

92- W. J. Youngblood, S.-H. A. Lee, K. Maeda and T. E. Mallouk, *Acc. Chem. Res.* **2009***, 42*, 1966–1973.

93- I. Romero, M. Rodriguez, C. Sens, J. Mola, M. R. Kollipara, L. Francas, L. Mas-Marza, E. Escriche and A. Llobet, *Inorg. Chem.* **2008**, *47*, 1824–1834.

94- M. W. Kanan and D. G. Nocera, *Science* **2008**, *310*, 1019–1021.

95- F. Jiao and H. Frei, *Angew. Chem. Int. Ed.* **2009**, *48*, 1841–1844.

96- K. Sivula, R. Zboril, F. L. Formal, R. Robert, A. Weidenkaff, J. Tucek, J. Frydrych and M. Grätzel, *J. Am. Chem. Soc.* **2010**, *132*, 7436–7444.

97- B. Neumann, P. Bogdanoff and H. Tributsch, *J. Phys. Chem. C* **2009**, *113*, 20980–20989.

98- Y. Ling, G. Wang, D. A. Wheeler, J. Z. Zhang and Y. Li, *Nano Lett.* **2011**, *11*, 2119–2125.

99- K. Maeda and K. Domen, *J. Phys. Chem. Lett.* **2010**, *1*, 2655–2661.

Chapter 2

Electrochemical Methods for Studying Catalytic Water Splitting: A Ru-red Model Study

ABSTRACT

To study the possibility of water oxidation by Ru-red, $[(NH_3)_5Ru\text{-}O\text{-}Ru(NH_3)_4\text{-}O\text{-}Ru(NH_3)_5]Cl_6$, and ruthenium oxide in acidic media, oxygen evolution measurements are performed with the electrochemical rotating ring-disk electrode (RRDE) and on-line electrochemical mass spectrometry (OLEMS), and are complemented by spectro-electrochemical investigations during water splitting catalysis with *in situ* surface enhanced Raman spectroscopy (SERS). Ru-red dispersed in acid electrolyte and immobilized on a gold surface without Ru-red in solution has been subjected to anodic water oxidation experiments. The catalytic behaviour of electrodeposited ruthenium oxide thin film on the Au disk was also studied for oxygen generation and the results were compared with Ru-red. On a gold electrode in sulphuric acid solution containing Ru-red, we observe one electron oxidative conversion to a higher oxidation state ruthenium compound, Ru-brown $[(NH_3)_5RuORu(NH_3)_4ORu(NH_3)_5]^{7+}$ at *ca.* 0.74 V (vs. NHE), which was supported by *in situ* SERS experiments. RRDE analyses produce oxygen detection signals at the ring around 1.25 V (vs. NHE). However, the oxygen formation is not validated by the OLEMS analysis. In contrast, a Ru-red functionalized gold electrode in same electrolyte solution without having Ru-red gives rise to the water oxidation signal and the oxygen onset potential is just above 1.45 V (vs. NHE). Oxygen reduction signals are present on the RRDE current-potential profile, which were confirmed for oxygen evolution by real time oxygen detection in OLEMS set up. The data provide evidence for water oxidation close to the equilibrium potential of 1.23 V (vs. NHE) in sulphuric acid by an immobilized ruthenium based molecular catalyst.

Based on: K.S. Joya, H.J.M. de Groot and M.T.M. Koper (*to be submitted*)

2.1. INTRODUCTION

The introduction of renewable energy [1] carriers based on solar energy and using water as a raw material is stimulated by the worries for global warming and decreased availability of oil and gas [2-6]. Efficient water oxidation is challenging from a catalytic standpoint, and the most critical hurdle is to design and make a stable multi-electron transfer catalyst that can split water at high turnover rates [7]. The Mn_4O_4Ca cluster in natural photosystem-II is an inspiring model of an oxygen evolving complex that catalyzes four electron water oxidation with a moderate activation energy and electrochemical overpotential [8-13]. This has fueled scientific interests towards the construction of artificial water splitting catalytic systems that attempt to mimic closely the natural catalyst in terms of configuration and efficiency [14-21]. Various ruthenium and manganese complexes as discussed in the previous chapter have been considered as "artificial" water splitting catalysts, and a maximum turnover number up to 1500 is obtained [21-26]. Generally, these systems are investigated by using chemical oxidants to promote four electron water oxidation [27].

Ru-red, a di-μ-oxo-bridged trinuclear ruthenium amine complex $[(NH_3)_5RuORu(NH_3)_4ORu(NH_3)_5]Cl_6$ (Fig. 2.1) has been shown to be catalytically active for water splitting [28]. While this system has also been studied in an electrochemical environment, the mechanism of electrocatalytic oxygen evolution on Ru-red was not studied in much detail [28-34]. On a basal plane pyrolitic graphite electrode (PGE) in 0.1 M H_2SO_4 aqueous solution, Ru-red was found to undergo one electron conversion into Ru-brown and ultimately to water oxidation and dioxygen formation, which was detected by gas chromatography combined with mass spectrometry (GC-MS) [28,32]. In acidic and aqueous solutions at room temperature, the oxo-bridges are not stable, which facilitates thermal and photo-induced decomposition of Ru-red into monomeric ruthenium compounds [28,34]. On the other hand, Ru-brown was reported to be unaffected by thermal or photochemical decomposition in 0.05 M nitric acid [35].

Combined spectral and electrochemical studies of a solution containing Ru-red did not reveal any decomposition of the complex during the electrochemical process [32,34]. It has also been reported that the anodic oxidation of Ru-red led to the formation of ruthenium-brown without the formation of RuO_2 [28]. In addition, there is only scant direct evidence that Ru-red did not convert into RuO_2 before or during water splitting. This issue is especially relevant as RuO_2 is an extremely potent catalyst for oxygen evolution [36]. *In situ* visible absorption spectroscopy experiments by Ramaraj and Kaneko showed that Ru-brown is unstable when conditions for homogeneous water oxidation are applied, while incorporation in a heterogenous Nafion membrane stabilizes the complex against decomposition and exhibits catalytic activity [32,37].

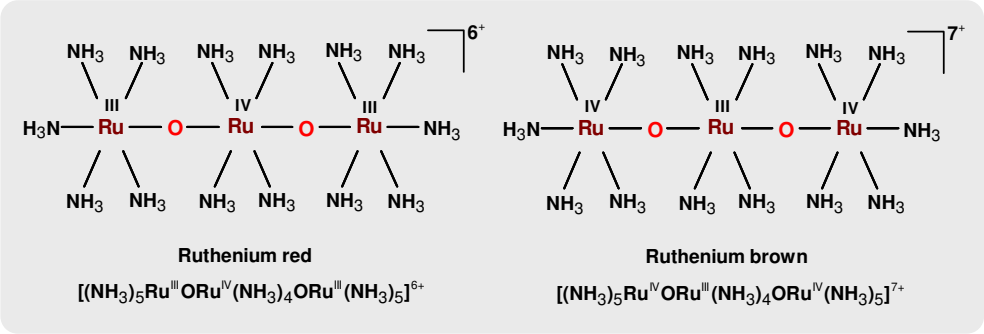

Figure 2.1. Chemical structural formula of (**left**) Ru-red and (**right**) Ru-brown showing ruthenium and oxygen architecture and metal oxidation states. Three Ru nuclei are connected by two oxo-bridges in amine ligands surrounding.

This chapter follows up on the observation by Kaneko *et al*. [30] that Ru-red immobilized on gold and platinum [38,39] electrodes is also active for electrocatalytic water oxidation. As Ru-red on polycrystalline gold disk (Au_{disk}) is one of the simplest examples of a surface modified with a molecular catalyst for water oxidation, it is of interest to study the electrochemical and spectroelectrochemical characteristics of this system. In addition, the Ru-red/Au_{disk} system enables the application of two established (spectro-)electrochemical techniques for its further characterization that will be used in this chapter.

First of all, application of the RRDE technique allows for the *in situ* detection of oxygen generated at the Ru-red/Au_{disk} electrode by a platinum ring (Pt_{ring}) biased for oxygen reduction. The RRDE technique, which has been used for the study of oxygen evolution by oxidic catalysts and oxygen reduction [40-43], has been applied very rarely in electrochemical studies of molecular catalysts for water oxidation. Second, using gold as a substrate for Ru-red permits the application of SERS to probe the vibrational signatures of the catalyst system at the metal-electrolyte interface. Using these two techniques, water oxidation catalyzed by Ru-red was investigated for a bare Au_{disk} electrode in contact with a sulphuric acid electrolyte solution containing Ru-red, and for a Ru-red functionalized gold electrode, without Ru-red in the electrolyte solution. In parallel, we compare the properties of Ru-red on gold with those of another well known Ru-based water oxidation catalyst, ruthenium oxide (RuO_x), by using the same experimental conditions as for Ru-red. The main objectives of this work are thus to apply the RRDE for sensitive and direct oxygen measurements, and validating its data using an OLEMS set up, along with the SERS investigation for interfacial vibrational characterization during water splitting catalysis by the molecular complexes, and comparing the activities of the Ru-red and the RuO_2 catalysts.

2.2. RESULTS AND DISCUSSION

2.2.1. RRDE Studies

Figure 2.2 summarizes the results obtained with the RRDE setup for three different experiments: oxygen evolution on a bare gold disk electrode (dash-dotted line), water oxidation on a clean Au electrode with Ru-red in solution (solid line), and oxygen evolution on an Au electrode functionalized with Ru-red (dashed line) in deoxygenated and Ar-saturated 0.1 M H_2SO_4 aqueous solution as explained in the section 2.4 of this chapter. Figure 2.2a shows the disk current density (J_D), while the lower panel displays the corresponding ring current density (J_R). Both J_D and J_R are obtained simultaneously at a rotation rate of 700 rpm by cycling the potential of

the Au_{disk} between 0.50 and 2.10 V (vs. NHE) at a scan rate of 20 mVs^{-1}, while the Pt_{ring} was kept at 0.44 V (vs. NHE). For this ring potential, the oxygen reduction on the polycrystalline Pt_{ring} is limited by mass transport [44,45]. Figure A2.1 (Appendix A2) shows voltammetric scans at the platinum ring for different gold disk potentials for the validation of oxygen evolution during the oxidation process at high disk potentials.

It is evident from Figure 2.2a that on a bare Au electrode, oxygen evolution starts just above 1.80 V, which is in good agreement with the results reported by Vergé *et al.* [43]. The corresponding reduction current at the ring is indeed due to the oxygen reduction provided that no oxidation products are coming from the gold disk that can be reduced or detected at the ring under given conditions (Fig. 2.2b). The collection efficiency ($N=-I_{Ring}/I_{Disk}$) is lower than the theoretical value, *i.e.* $N_{exp} \approx 0.025$ vs. $N_{theo} = 0.256$ (see Materials and Methods section). The deviation corroborates observations made by Vergé *et al.* using a gold ring as well as by various other authors employing the RRDE technique to investigate the oxygen evolution reaction [Ref. 43 and references therein]. The low collection efficiency is attributed to the formation of oxygen bubbles at the anode catalyst, which is difficult to assess during the potential scanning on a disk electrode in the RRDE system.

The formation of gold oxides and oxygen evolution occur simultaneously at higher potential of the Au_{disk} electrode. Hence, the measured anodic current for oxygen evolution at the Au electrode is the sum of the gold oxide growth current and the water oxidation current, which dominates at higher potential [43]. Although the difference between the experimental and theoretical values prevents a quantitative analysis of the results, the RRDE provides unequivocal detection of oxygen formed by the catalytic water oxidation on the disk electrode. RRDE analyses reveal that both Ru-red systems (*i.e.* one with Ru-red in solution and one with Ru-red immobilized on the Au disk but not present in solution) exhibit a significantly lower overpotential for water oxidation than the bare gold electrode.

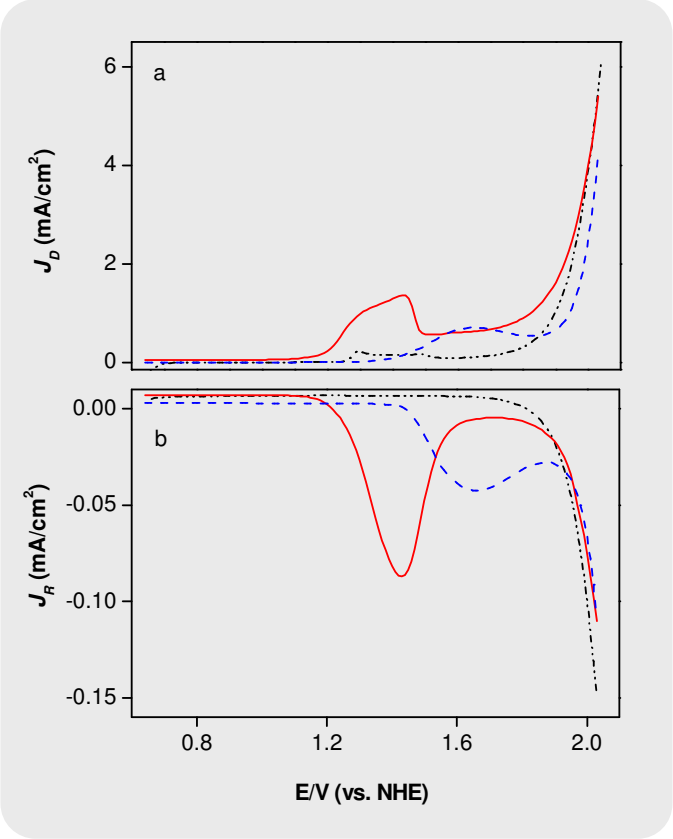

Figure 2.2. Forward potential scans for oxygen evolution current densities (J_D); (**a**) for the bare Au_{disk} (dash dotted line), the bare Au_{disk} in 0.1 M H_2SO_4 solution containing 0.035 mM Ru-red (solid line) and a gold disc functionalized with Ru-red (dashed line) in deoxygenated 0.1 M H_2SO_4 electrolyte solution, and (**b**) corresponding oxygen reduction current densities (J_R) on the Pt_{ring} for the RRDE assembly in 0.1 M H_2SO_4 aqueous solution. Rotation rates were 700 rpm, scan rates 20 mV/sec and the ring potential was 0.44 V (vs. NHE).

With Ru-red in solution, the onset of oxidation is at a potential as low as 1.23 V (vs. NHE), mirrored by oxygen reduction current at the Pt_{ring} (Fig. 2.2b) assuming that no adsorption or electrodeposition of the catalyst on the Pt_{ring} occurs and no simultaneous formation of the Ru-red oxidation products at the gold disk which may get in contact with the ring during rotation at 700 rpm. To show that the current measured at the ring is indeed due to oxygen coming from the disk, we have investigated the voltammetry at the ring while keeping the disk potential at ~1.35 V (Fig. A2.2). The oxygen reduction wave was not observed around 0.44 V,

at the Pt ring, but a current wave appeared at <0.15 V, when the disk potential kept at 1.23 V, which becomes more positive when the potential rises. This current might be associated with the oxygen detection at less positive potential on the Pt_{ring} that is in contact with the Ru-red in the electrolyte solution. This could block the ring surface for effective oxygen reduction.

On the other hand, the collection efficiency for this experiment, *ca*. 0.05, is less than the theoretical value. The low collection efficiency is in line with the formation of oxygen and oxygen bubbles at the disk electrode, and this renders a detailed quantitative interpretation of the RRDE results unfeasible. The oxygen evolution ability reaches a maximum at *ca*. 1.44 V and then drops, reflected by a similar decrease in reduction current on the ring. This loss in catalytic activity at higher potentials may be ascribed to over-oxidation of the Ru-based catalyst. Similar disk and ring voltammetry is observed in subsequent scans, although overall currents decrease with each scan, indicating a gradual loss of the catalytic performance of Ru-red for water oxidation. Variation of the catalyst concentration by four to five times did not have a significant effect on the catalytic activity of Ru-red, regardless of whether the catalyst was dissolved in 0.1 M H_2SO_4 or adsorbed on the Au_{disk}.

Interestingly, oxidation wave on the Ru-red functionalized Au electrode starts at *ca.* 1.44 V (vs. NHE), approximately 210 mV higher than the experiment with Ru-red in solution (Fig. 2.2). In this case, the current at the ring cannot be due to another process than oxygen reduction, as there is virtually no Ru-red in the solution. No colouring of the solution was observed due to free Ru-red during potential scanning of the RRDE at 700 rpm, indicating that there was no detachment of Ru-red from the Au_{disk} during cycling at this rotation rate. The experimental collection efficiency, *ca*. 0.05, is still lower than the theoretical value, but similar to the system with Ru-red in solution. Also this system exhibits a maximum in catalytic activity within one scan, and a decrease in catalytic activity with each subsequent voltammetric scan, pointing again to instability of the Ru-red catalyst at higher potential. Cycling the potential of the ring, while the potential of

the Au_{disk}, functionalized with Ru-red, was kept around 1.45 V, reveals a reduction current at the ring in the oxygen detection regime when the catalyst was not present in the solution (Fig. A2.3). The current increases with rising potential and this indicates the formation of oxygen at *ca*. 1.44 V for the Au functionalized Ru-red system.

Kaneko *et al*. has reported the electrochemistry of Ru-red in 0.1 M H_2SO_4 aqueous solution at a poly(styrene sulphonate)-coated basal plane pyrolitic graphite (BPG) electrode. They observed the conversion of Ru-red into Ru-brown (Eq. 2.1) and cyclic voltammogram exhibited redox features during the oxidative scan and proposed that the Ru^{V}-O-Ru^{V}-O-Ru^{V} (Ru^{V}-Ru^{V}-Ru^{V}) state releases oxygen [34]. The oxidative transitions take place at 1.08 V for Ru^{IV}-Ru^{IV}-Ru^{IV}/Ru^{IV}-Ru^{III}-Ru^{IV}, 1.19 V for to Ru^{IV}-Ru^{V}-Ru^{IV}/Ru^{IV}-Ru^{IV}-Ru^{IV}, 1.32 V for Ru^{V}-Ru^{IV}-Ru^{V}/Ru^{IV}-Ru^{V}-Ru^{IV} and 1.40 V for Ru^{V}-Ru^{V}-Ru^{V}/Ru^{V}-Ru^{IV}-Ru^{V} (vs. NHE). In our study on a gold electrode in 0.1 M H_2SO_4, we were unable to resolve these oxidation peaks for Ru-red conversion into Ru-brown and its higher oxidation states.

$$\underset{\text{(Ru-red)}}{Ru^{III}\text{-O-}Ru^{IV}\text{-O-}Ru^{III}} \underset{\text{Neutral/OH}^-,\ +e^-}{\overset{\text{Acid (H}^+\text{), -e}^-}{\rightleftharpoons}} \underset{\text{(Ru-brown)}}{Ru^{IV}\text{-O-}Ru^{III}\text{-O-}Ru^{IV}} \qquad (2.1)$$

In order to compare the activity of the Ru-red-Au system with RuO_2, a hydrous ruthenium oxide ($RuO_x \cdot nH_2O$) film was electrodeposited on a roughened Au_{disk} surface in the RRDE assembly. Oxygen evolution on the RuO_x-modified Au electrode starts close to 1.30 V and drops dramatically at *ca*. 1.45 V (Figure 2.3), nearly identical to the oxygen evolution characteristics of a solution containing Ru-red in contact with gold electrode (Fig. 2.2). This also implies the possibility of the oxidative decomposition of the Ru-red near 1.25 V at gold disk to form some oxide of ruthenium. *In situ* SERS analyses for Ru-red and electrodeposited ruthenium oxide are conducted for further elucidation (see section 2.2.3). The electrodeposited oxide of ruthenium on the gold surface leads to higher currents for

water oxidation compared to Ru-red, but this may be simply due to a higher number of active catalytic sites on the Au electrode.

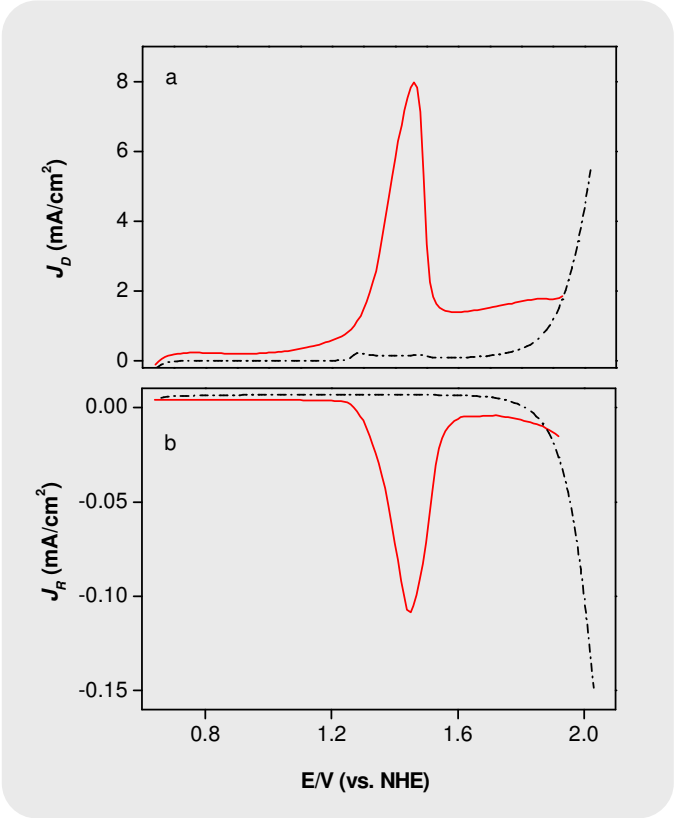

Figure 2.3. (**a**) Forward potential scans for oxygen evolution current densities (J_D) for the bare Au_{disk} electrode (dash dotted line) and for electrodeposited ruthenium oxide on Au_{disk} in deoxygenated Ar-saturated 0.1 M H_2SO_4 electrolyte solution (solid line), and (**b**) corresponding oxygen reduction current densities (J_R) on the Pt_{ring} in the RRDE assembly in 0.1 M H_2SO_4 aqueous solution. Rotation rates were 700 rpm, scan rates 20 mV/sec and the ring potential was 0.44 V (vs. NHE).

Similar to the systems shown in Figure 2.2, the experimental collection efficiency of the RRDE assembly consisting of a RuO_x-modified Au electrode and a Pt_{ring} is again significantly below the theoretical value suggesting oxygen bubble formation at the Au anode along with the possibility of higher metal oxide generation. Previous RRDE studies of oxygen evolution of Ru-oxide have shown that RRDE techniques may be used to detect both oxygen and Ru corrosion

products, such as RuO_4 but we did not attempt to detect the oxidation products [41,46].

Comparing the oxidation current on the gold disk with the reduction current on the platinum ring, it is observed that the oxidation current at the onset of the peak, between *ca*. 1.0 and 1.22 V (Fig. 2.3), is not due to oxygen evolution. This oxidation current must therefore be ascribed to the further oxidation of the Ru deposits. A similar observation was made by Wohlfahrt-Mehrens and Heitbaum, who followed the oxygen evolution by a ruthenium film electrode in sulphuric acid employing differential electrochemical mass spectrometry (DEMS) [47]. Their experiment shows an oxidation current between 1.1 and 1.4 V (vs. NHE) that is not accompanied by the detection of oxygen in the DEMS, whereas the high oxidation current for potentials higher than 1.4 V (vs. NHE) leads to a significant detection of oxygen in the online mass spectrometer. In a recent study, cyclic voltammetry of uncalcined and calcined (350–550° C) RuO_2 deposits in 1 M H_2SO_4 at 20 mV/sec has shown irreversible current peaks at *ca*. 0.70 V (vs. NHE). These current peaks have been assigned to the valence state change of the ruthenium in oxide matrices from Ru^{III} to Ru^{IV} [48]. However in this study, the current-potential profile of the electrodeposited RuO_x on Au is almost a smooth curve, without significant voltammetric features (Fig. 2.3a).

In another set of experiments, Ru-red immobilization and ruthenium oxide electrodeposition was performed on a basal plane graphite disk. The results for oxygen evolution are compared with those obtained on Au substrate. The oxygen onset occurs above 1.37 V (vs. NHE) on the BPG-RuO_x matrix as indicated by reduction currents at the ring. Interestingly, the BPG modified Ru-red electrode displays the oxygen evolution wave beyond 1.65 V (vs. NHE) reflected by the ring detection current (Fig. 2.4). No oxygen reduction currents were observed for the bare BPG up to the limiting potential of the experimental setup. Later, the oxygen generation was confirmed by employing a calibrated oxygen sensor connected with an oxy-meter [23]. The reason for different activity of Ru-red on

Au and graphite electrodes is not clear at present and further experiments need to be done to address this question.

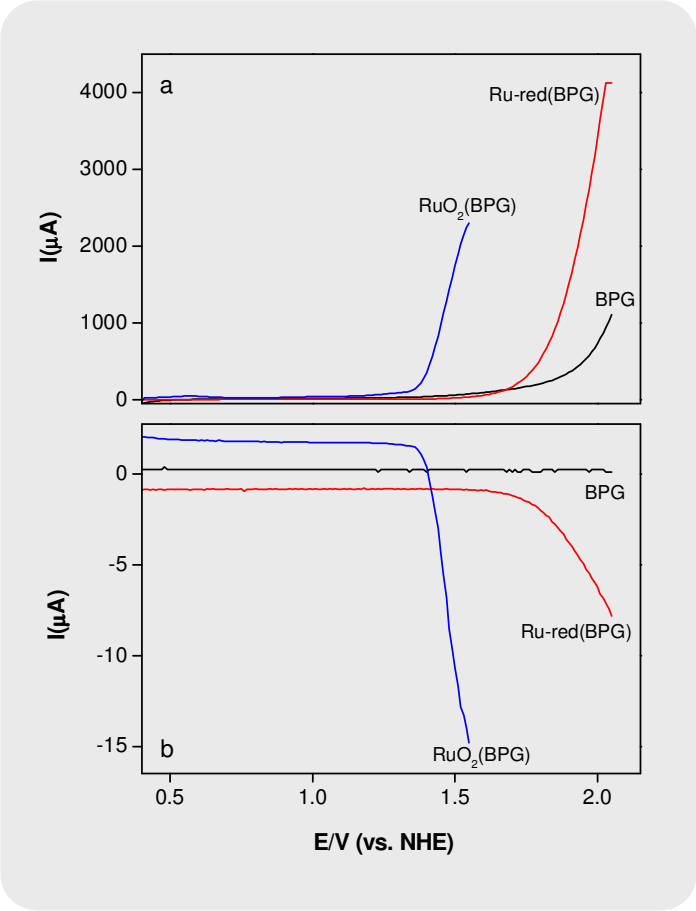

Figure 2.4. Forward potential scans for oxygen evolution currents: (**a**) for the bare BPG disk, the BPG functionalized with Ru-red and for electrodeposited RuO_x on BPG disk in deoxygenated 0.1 M H_2SO_4 electrolyte solution, and (**b**) corresponding oxygen reduction currents on the Pt_{ring} for the RRDE assembly in 0.1 M H_2SO_4 aqueous solution. Rotation rates were 700 rpm, scan rates 20 mV/sec and the ring potential was 0.44 V (vs. NHE).

2.2.2. OLEMS Analysis

Oxygen confirmation experiments on gold disk in contact with the tri ruthenium catalyst were conducted using online electrochemical mass spectrometry measurements in acidic medium. Real-time oxygen generation and detection

analyses were performed during linear sweep voltammetric scans, from the Au electrode immersed in the electrolyte solution containing Ru-red and the gold disk functionalized with the catalyst without Ru-red in the solution. The Au_{disk} functionalized with Ru-red and without Ru-red in the solution reveals oxygen detection by the OLEMS measurements between 1.50 and 1.60 V vs. NHE (Fig. 2.5a), thus verifying the RRDE studies (Fig. 2.2). No attempts were made to record the oxygen while scanning back from ~1.9 V in the same experiment.

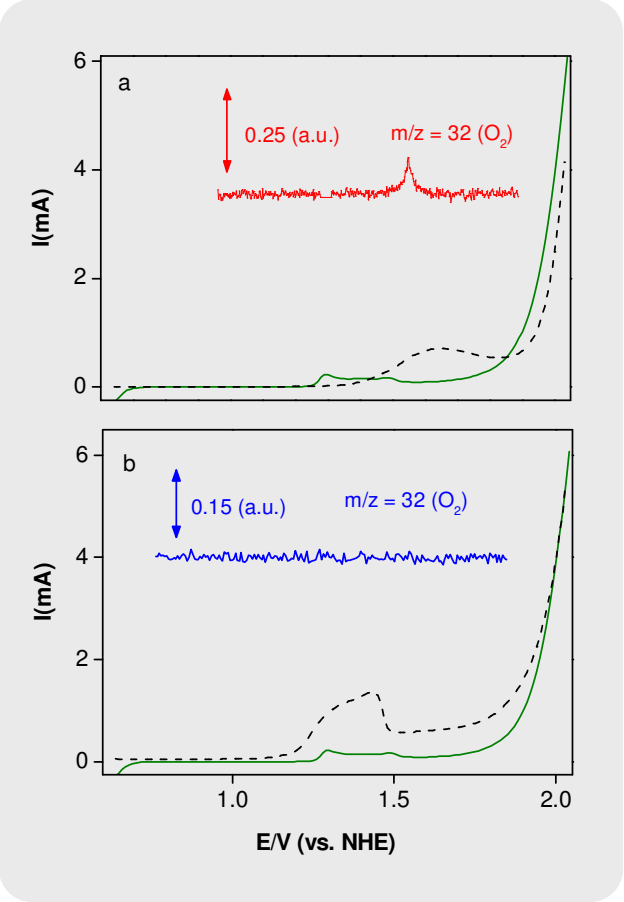

Figure 2.5. Forward potential voltammetry showing the oxygen evolution current and corresponding real time OLEMS measurements (red and blue curves) for (**a**) the gold disk functionalized with Ru-red in deoxygenated 0.1 M H_2SO_4 solution containing no Ru-red and (**b**) a bare gold disk in 0.1 M H_2SO_4 solution containing 0.035 mM Ru-red (1.0 mV/sec). The green solid lines in both panels are the CV's of the bare Au disk 0.1 M H_2SO_4 solution.

There is no evidence from the OLEMS analysis for the possible generation of peroxide intermediates during water oxidation and the final catalytic phase involved in the dioxygen evolution from Ru-red as detected by OLEMS [28,34]. The oxygen detection peak suddenly declines and flattens at a potential of ~1.63 V suggesting decomposition or/and instability of Re-red on the gold surface. This corroborates our inference from RRDE that the current regime above 1.71 V does not involve the formation of oxygen (Fig. 2.2). Surprisingly, no oxygen (m/z = 32) formation was detected between 1.23 – 1.65 V (vs. NHE) for the bare Au in contact with the solution containing Ru-red (Fig. 2.5b), which does not validate our inferences obtained from RRDE experiments (Fig. 2.2). A preliminary controlled-potential electrolysis experiment was performed for the gold disk functionalized with the catalyst without Ru-red in the solution, but the catalyst was found to be unstable for longer time exposure in the aqueous sulfuric acid.

2.2.3. Electrochemical SERS Investigations

In situ SERS experiments were conducted as described in section 2.4. Figure 2.6a shows the *in situ* SER spectra of Ru-red on gold at selected potentials when Ru-red was present in solution and Figure 2.6b shows the same spectra for Ru-red immobilized on gold (RRA) without Ru-red in solution. Various Raman shifts were observed for the trinuclear ruthenium-amine catalyst and peak assignments can be made by comparison with the data reported in the literature. Table 1.1 gives the Raman shifts (cm^{-1}) for Ru-red and Ru-brown in the 100-1000 cm^{-1} region, which is the finger print region of Ru-red and Ru-brown [49,50]. In the solid state Ru-red has a nearly linear backbone structure with octahedral surroundings of the metal ions and near C_{4v} symmetry due to packing effects on the molecular skeleton [51]. Raman data have indicated that Ru-red adopts a near D_{4h} symmetry in solution, with the octahedrons aligned along the backbone, albeit without perfect inversion symmetry, and that Ru-brown has a similar structure [50,52-54]. For the D_{4h} symmetry 6 modes are Raman active, which have been assigned in a series of investigations (Table 1.1) [50,54].

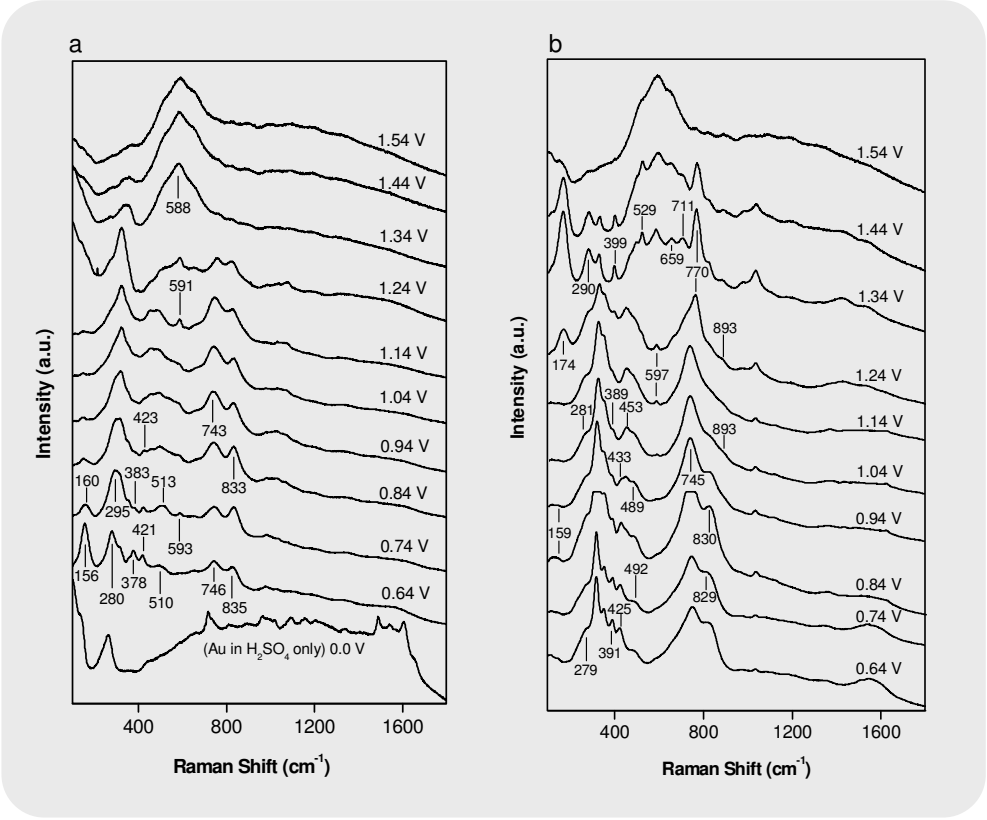

Figure 2.6. Selected potential-dependent *in situ* electrochemical SER spectra for (**a**) the freshly roughened Au_{disk} electrode in deoxygenated 0.1 M H_2SO_4 aqueous solution containing 0.035 mM Ru-red and (**b**) Ru-red functionalized freshly roughened Au_{disk} electrode in deoxygenated Ar-saturated 0.1 M H_2SO_4 aqueous solution. The starting potential was 0.6 V and it was increased to 1.5 V (vs. NHE) in successive 0.1 V increments.

The deviation from the D_{4h} is apparent from the observation of a strong antisymmetric mode at 825 nm in Ru-red. Although the principal Raman characteristics of Ru-red and Ru-brown are very similar, the ν_1, ν_5, ν_6, and ν_7 bands for Ru-brown are all shifted to higher frequency compared to the corresponding vibrations in Ru-red, by 34, 13, 21 and 15 cm^{-1}, respectively, indicating a stiffening of the backbone when Ru-red is converted into Ru-brown [54]. Incomplete conversion of Ru-red into Ru-brown was found to produce smaller shifts [50,54]. However, in particular the frequency of the ν_1 Ru-O symmetric stretch involving the two oxygen adjacent to the central Ru ion is very sensitive to the Ru-red to Ru-

brown transition, which is thought to be related to the removal of an electron from an antibonding orbital located on the Ru-O-Ru-O-Ru backbone [54]. These spectral features allow the detection of the Ru-red to Ru-brown transition, which is one of the aims of our spectro-electrochemical experiment (Figs. 2.6, Table 1.1).

Table 1.1. Raman Shifts (wavenumbers cm^{-1}) for Ru-red in solution.

Compound		Raman Shifts (wavenumbers cm^{-1})*	
Ru-red	Ru-brown	Assignment	
157	178	ν_6	Ru-O
281	294	ν_5	O-Ru-N
376	390	$\nu_{2,3,4,8,9}$	Ru-N
396			
438	424		
486			
540			
744	778	ν_1	Ru-O
780			NH_3
825	840	ν_7	Ru-O

*in accordance with Ref. 49-51.

In Figure 2.6a, at low potential (0.64 V), the spectrum clearly indicates the presence of Ru-red near or on the electrode surface. The band at 156 cm^{-1} has been attributed to the ν_6 Ru-O stretching frequency; the same vibration in Ru-brown has been observed at 178 cm^{-1} [50], while it is not observed in the spectrum at 0.64 V. The feature at 280 cm^{-1} has been assigned to the O-Ru-N bending vibration, and it supposedly shifts to higher wavenumbers (*ca.* 294 cm^{-1}) for Ru-brown. The smaller features at 378, 421 and 510 cm^{-1} could correspond to Raman shifts observed for either Ru-red or Ru-brown, but the pair of features observed at 746 and 835 cm^{-1} appears as characteristics for Ru-red. Both modes are Ru-O

stretching modes, reported at 744 and 825 cm^{-1} for Ru-red in solution (the corresponding modes for Ru-brown are at 778 and 840 cm^{-1}). Considering the dominance of the modes at 156, 280, and 746 cm^{-1}, which are all characteristic of Ru-red (see also Table 1.1), we derive that the species most prominently observed at 0.64 V is Ru-red.

As the electrode potential is stepped positively, some important spectral changes are observed as shown in Figure 2.6. In general, changes in intensity and frequency may be related to three different effects: a change in identity of the species (*e.g.* a conversion from Ru-red to a Ru-brown type species) as a result of a change in electrode potential, a change in orientation or structure of the adsorbed Ru-red (or Ru-brown), or an electrochemical Stark tuning effect in which the electric field existing at the interface leads to changes in the vibrational frequencies and the intensity of the SERS lines of the adsorbed species [55]. As stated earlier, the SER spectra of Ru-red in Figure 2.6a show predominantly Ru-red features at the start of the positive potential scan (0.64 V). The band at 280 cm^{-1} shifted to a higher wavenumber *ca.* 295 cm^{-1} at 0.74 V (vs. NHE) indicating the possible formation of Ru-brown or similar species near the Au electrode at this potential, though the 156 and 745 cm^{-1} bands seem to be unaffected. However, the 156 cm^{-1} band decreases in intensity with the positive-rising potential. In spite of the continued dominance of the spectral pair at 740 and 835 cm^{-1} at higher potentials, which we ascribe to Ru-red, the disappearance of the band at 157 cm^{-1} and the shift of the band at 280 to 295 cm^{-1}, may indicate the formation of a (small) amount of Ru-brown or a similar species at potentials higher than ca. 0.7 V (vs. NHE).

In a previous report by the Kaneko group, the transition of Ru-red to Ru-brown has been observed by *in situ* electrochemical visible absorption spectral studies in a phosphate buffer solution at pH=7.4 on a thin layer ITO electrode during oxidative scans from 0.42 to 0.75V (vs. NHE) [32]. Although the SER spectra in Figure 2.6a contribute to converging evidence for the Ru-red conversion into the Ru-brown at this potential [28,32-34], some features attributable to Ru-red remain present even at this potential. The RRDE experiment revealed that water oxidation may occur at

low overpotential (Fig. 2.2) catalyzed by Ru-red, suggesting the formation of higher oxidation state Ru species like Ru^{V}-O-Ru^{V}-O-Ru^{V} or similar intermediates and their possible involvement in water oxidation process. Above this potential, gold oxide species (as indicated by a broad Raman band at 588 cm^{-1}) are observed similar to bare gold in the same electrolyte but without Ru-red in the solution (see Fig. A2.4).

Figure 2.6b shows the SER spectra obtained at selected potentials on the Ru-red functionalized Au electrode (RRA) without Ru-red in solution. Raman bands at 281, 745 and 829 cm^{-1} and a small broad band at *ca.* 159 cm^{-1} at low potential (0.64 V) suggesting the presence of (adsorbed) Ru-red on the Au_{disk} (Table 1.1). At 1.24 V (vs. NHE), the Raman bands at *ca.* 159 cm^{-1} and 745 cm^{-1} have shifted to *ca.* 174 cm^{-1} and 770 cm^{-1} respectively, providing evidence for formation of a Ru-brown type species at this potential. However, no profound changes were observed in the 281 cm^{-1} band. Compared to SER spectra on the gold electrode with Ru-red in the solution (Fig. 2.6a), the SERS analysis of RRA (without Ru-red in the electrolyte solution) shows a delayed appearance of the formation of Ru-brown signals (Fig. 2.6b) suggesting a different catalytic behaviour of Ru-red for the two systems deposited on the roughened gold electrode, in agreement with the different applied electrode potentials at which the two systems show catalytic characteristics for oxygen evolution (Fig. 2.2).

With more than 1.34 V applied to the RRA, additional Raman peaks are observed at *ca.* 529, 659, and 711 cm^{-1}. These modes may be associated with the formation of decomposition products in the catalyst [50]. Gold oxide vibrations can be discerned in the Raman spectra at potentials above 1.44 V. In order to compare the Ru-red features with the ruthenium oxide during water oxidation, a thin hydrous film of electrodeposited ruthenium oxide ($RuO_x \cdot nH_2O$) was also investigated by spectro-electrochemical Raman experiments. The SER spectra of a hydrous ruthenium oxide freshly electrodeposited on a roughened gold disk electrode were collected in a 0.1 M H_2SO_4 aqueous electrolyte without Ru-red or free Ru in the solution (Fig. A2.5).

Raman shifts observed at wavenumber 522, 665 and 742 cm^{-1} would be indicative of the presence of ruthenium oxide as it is found to be Raman active in the range of 450-800 cm^{-1} as vibrational modes [56,57]. The intensities of these bands gradually decrease by increasing the potential to more positive values, suggesting the conversion or loss of the ruthenium oxide species on the gold surface. The SER spectra show that the features ascribable to the electrodeposited ruthenium oxide ($RuO_x \cdot nH_2O$) on the Au_{disk} are present until 1.24 V, (Fig. A2.5), essentially just before the water oxidation sets in (as seen in the RRDE experiment in Fig. 2.3). For potentials above 1.24 V, the ruthenium oxide features disappear and a broad band at 597 cm^{-1} due to the formation of gold oxide on the surface dominates the spectrum (See also Fig. A2.4).

Summarizing, the Raman spectra of Ru-red on bare gold with Ru-red in solution, of the Ru-red functionalized gold electrode, and of Ru-oxide modified gold electrode, all show different and distinctive features. For the two systems with Ru-red, the Raman data suggest a transition from Ru-red to a Ru-brown type species with increasing potential, and the transition appears to take place at significantly more positive potentials when Ru-red is only on the surface and not in solution. The delay in oxidation behaviour is mirrored by the activity for water oxidation, which also occurs at significantly more positive potentials for the Ru-red functionalized gold electrode without Ru-red in solution. In particular for the latter system, Raman active modes are observed close to the onset of oxygen evolution. These modes show some resemblance to the Raman features observed for ruthenium oxide. Such features are not clearly observed for the system with Ru-red in solution, while the catalytic activity of the system is similar to that of the gold electrode modified with Ru-oxide.

2.3. CONCLUSIONS

In this chapter, catalytic oxidation of water by Ru-red in acidic media with successfully employing the electrochemical rotating ring-disk electrode (RRDE), online electrochemical mass spectrometry (OLEMS), and *in situ* surface enhanced Raman spectroscopy (SERS) for spectro-electrochemical investigations during water splitting catalysis, is discussed. Oxygen evolution and detection experiments using Ru-red and electrodeposited ruthenium oxide were conducted on RRDE, revealing oxygen evolution currents complemented by a corresponding reduction current at the platinum ring electrode. OLEMS measurements validate the RRDE findings for the Ru-red functionalized gold electrode that displays water oxidation just above 1.45 V (vs. NHE). In contrast, with deposition on a bare gold electrode in sulphuric acid solution containing Ru-red, the onset of oxygen evolution seems to start at ~1.23 V (vs. NHE) but not supported by the OLEMS analysis. SERS experiments show that Ru-red undergoes electro-induced oxidative conversion to a higher oxidation state ruthenium compound, probably a form of Ru-brown, at *ca*. 0.74 V (vs. NHE). The Ru-brown type species subsequently loses three more electrons and, ultimately, oxidizes water to make dioxygen [28-32]. In another set of experiments on the electrodeposited ruthenium oxide film on the Au_{disk}, the onset of oxygen evolution is observed at *ca*. 1.30 V (vs. NHE). Thus, electrochemical methods to test catalytic water oxidation using a commercially available trinuclear ruthenium complex are described here. The RRDE method is exploited to study oxygen evolution and detection experiments and results are validated with the OLEMS measurements.

2.4. MATERIALS AND METHODS

Potassium ferricyanide ($K_3[Fe(CN)_6]$), $RuCl_3.nH_2O$ and Ru-red ($[(NH_3)_5Ru\text{-}O\text{-}Ru(NH_3)_4\text{-}O\text{-}Ru(NH_3)_5]Cl_6$) were of reagent grade, obtained from Sigma-Aldrich Co., and used as received. All the solutions were prepared in ultra-pure water (Millipore MilliQ® A10 gradient, 18.2 MΩ cm, 2–4 ppb total organic content). All

solutions were purged with high-purity argon (Linde Gas, 6.0) for at least 30 min before each measurement to minimize the oxygen interference during electrochemical investigations. An argon atmosphere was maintained both in and above the solution during the electrochemical measurements to make sure that no air/oxygen was entering and intervening with the electrochemical system.

All glassware and cells were cleaned by boiling in a 1:1 mixture of concentrated nitric acid and sulfuric acid (for 2 hours and left overnight). Next, the glassware was washed and boiled in ultra-pure water and dried in an oven at 65° C. The cell was boiled and washed thoroughly with ultra-pure water before each experiment. All the electrochemical work was conducted in a conventional single-compartment three-electrode glass cell and RRDE experiments were performed in a home-made RRDE glass cell. A three electrode configuration spectro-electrochemical glass cell, having an optical quartz window at the bottom parallel to the gold working electrode, was employed for the electrochemical SERS investigation.

A polycrystalline gold and basal plane graphite disks (diameter d=5mm) were used as working electrode (WE) in voltammetry. A platinum disk (diameter d=5mm) was employed in the collection efficiency experiment. The working electrode in the SERS experiments was a roughened polycrystalline gold disk (diameter d=5mm) embedded in a PTFE shroud. A platinum wire (thickness: 1 mm), was used as a counter electrode (CE) and the reference electrode (RE) was a mercury–mercury sulfate electrode (MMSE: $Hg/Hg_2SO_4/K_2SO_4$). However, all potentials are referred to the normal hydrogen electrode (NHE). Rotating ring-disk electrode measurements were carried out on the RRDE-system with an AFMSRX rotator and a MSRX speed controller (Pine Instrument Company, Grove City, PA, USA). For oxygen detection measurements, the RRDE setup consisted of a mirror finished polished polycrystalline Au_{disk} (radius $r_1 = 0.250$ cm, area $A_{disk}=0.196$ cm^2) and a concentric Pt_{ring} (inner radius $r_2 = 0.325$ cm; outer radius $r_3 = 0.375$ cm; area $A_{ring}=0.11$ cm^2). The theoretical collection efficiency, N = 25.6%, was confirmed by standard experiments with the ferri-/ferro-cyanide couple [43].

Figure 2.7. Set up for RRDE assembly showing (**a**) working electrode (WE) disks, (**b**) ring and tip and (**c**) the rotor with a speed controller (taken from Pine Inst. web).

An EvoLution mass spectrometer system (European Spectrometry Systems Ltd.) was employed for on-line electrochemical mass spectrometry measurements. The pressure inside the mass spectrometer (MS) was 1×10^{-6} – 5×10^{-6} mbar during OLEMS measurements. Further details of the experimental parameters, pretreatment procedures and instrument operation are described previously [58]. SERS analysis was performed with a HR 800 spectrograph (Jobin Yvon) with a holographic grating of 600 gr mm^{-1}. The confocal hole of the instrument was set at 100 μm. A CCD camera with 1024 × 256 pixels was used as detector. The excitation line source was provided by a 20 mW HeNe laser at 632.8 nm. The laser beam was focused through an Olympus 50× microscope objective, which was not immersed in the electrolyte, into a 5 μm spot on the electrode surface. A notch filter was used to filter the SERS signal before reaching the sample. With this configuration, a resolution of 1.2 cm^{-1} was obtained [59]. Surface enhancement of the gold disk by roughening the gold surface was done by applying 25 potential sweep oxidation-reduction cycles consecutively in 0.1 M KCl (Merck, pro analysis) from 1.25 to –0.25 V versus the saturated calomel electrode (SCE: $Hg/Hg_2Cl_2/KCl$) [60].

Cyclic voltammetry, forward potential scans and other electrochemical investigations for RRDE measurements, OLEMS analyses and *in situ* SERS investigations were performed with a computer-controlled IviumStat (Ivium

Technologies, Eindhoven, The Netherlands) and operated by IviumSoft. Prior to the actual experiments, Au_{disk} and Pt_{ring} were polished mechanically with an aqueous slurry of 0.3, 0.1 and 0.05 μm alumina (Buehler Limited) successively, on a Microcloth polishing fabric, until a mirror finish was achieved. After polishing, the electrodes were ultrasonically cleaned in Milli-Q (Millipore) water for 15–20 minutes after each polishing step and rinsed thoroughly with pure water. A spiral platinum counter electrode was flame annealed and washed with pure water before placing into the cell.

Pure argon gas was purged into the 0.1 M H_2SO_4 electrolyte solution for at least 30 minutes at a rotation rate of 1200 rpm before the oxygen evolution-detection experiment with the Au_{disk}-Pt_{ring} RRDE assembly. This step is very important in order to ensure the complete removal of oxygen from the test solution which can possibly interfere with the oxygen detection/reduction measurements. Oxygen elimination from the continuously Ar-bubbled 0.1 M H_2SO_4 aqueous solution was carefully verified by scanning the freshly polished Pt_{ring} electrode on the RRDE assembly between +1.44 V and +0.02 V (vs. NHE) from 500-2500 rpm until no oxygen reduction/detection current was observed. After this confirmation, the Au_{disk} was fitted to the RRDE for oxygen evolution studies in Ar-saturated 0.1M H_2SO_4 aqueous solution. It was then cyclized between 0.64–2.04 V (vs. NHE) and the Pt_{ring} was potentiostated at +0.44 V (vs. NHE) at a rotation rate of 700 rpm.

Prior to the water splitting and oxygen measurements experiments, the Au_{disk} and Pt_{ring} were electrochemically pre-treated in 0.1 M $HClO_4$ or 0.05 M H_2SO_4 by scanning the potential between 0.5–2.1 V and +1.7 to –0.2 V (vs. NHE) respectively, for 50 cycles at 50 mV/sec. This procedure provided good reproducibility of the data [61]. After potential cycling, the electrodes were immediately transferred to another cell containing O_2-deaerated Ar-saturated 0.1 M aqueous sulphuric acid solution in order to avoid surface contamination in air. For oxygen detection/reduction experiments in 0.1 M aqueous sulphuric acid solution,

the potential of the Pt_{ring} was held at +1.44 V (vs. NHE) for 5 seconds and scanned between +1.44 and +0.02 V (vs. NHE) at 20 mV/sse.

Two types of experiments were conducted for oxygen evolution from water splitting by the Ru-red catalyst. In the first type of experiment, an aliquot of Ru-red catalyst solution, prepared in a small quantity of O_2-deaerated deionized water, was dissolved in O_2-deaerated Ar-saturated aqueous 0.1 M H_2SO_4 solution before the catalytic water oxidation experiment. The resulting Ru-red concentration was 0.035 mM. In the second type of experiment, Ru-red was immobilized on the Au_{disk} by adsorption. Ru-red does not bind strongly to a mirror-finish Au surface, and therefore, a roughened gold surface was prepared to which Ru-red binds more strongly. The catalyst was immobilized by placing 15 μL of a stock solution of Ru-red (0.05 mM), prepared in ultrapure deoxygenated water, on the roughened Au surface. It was dried for 4–6 hours and the same procedure was repeated 5 times. The electrode was subsequently left for at least 32–34 hours. After this procedure, it was rinsed with ultrapure water to remove the unattached Ru-red molecules and employed directly for electrochemical investigation without any delay.

A thin hydrous ruthenium oxide ($RuO_x \cdot nH_2O$) film was electrochemically deposited on a freshly roughened Au_{disk} from 0.01 M HCl and 0.1 M potassium chloride electrolytes containing 1 mM $RuCl_3$ in a deoxygenated aqueous solution (pH ≈ 2) by a procedure described in the literature [62]. In our experimental setup, the electrodeposition of the $RuO_x \cdot nH_2O$ film was realized by scanning the potential of the Au_{disk} electrode from 0.10–1.04 V (vs. NHE) for 160–180 cycles in the above chloride electrolyte solution at a scan rate of 50 mV/sec. The ruthenium oxide film thus produced was washed with pure water and employed without any further treatment in SERS and anodic water oxidation experiments using the RRDE setup.

REFERENCES

01- T. N. Verziroglu and F. Barbir, *Int. J. Hydrogen Energy* **1992**, *17*, 391–404.

02- J. E. Funk, *Int. J. Hydrogen Energy* **2001**, *26*, 185–190.

03- C. A. Grimes, O. K. Varghese and S. Ranjan, *Light, Water, Hydrogen: The Solar Generation of Hydrogen by Water Photoelectrolysis*, Springer Science + Business Media: New York, **2008**; Ch. 2.

04- A. J. Bard, *J. Am. Chem. Soc.* **2008**, *130*, 8565–8568.

05- T. J. Meyer, *Nature* **2008**, *451*, 778–779.

06- N. S. Lewis, *Nature* **2001,** *414*, 589–590.

07- X. Sala, M. Rodriguez, I. Romero, L. Escriche and A. Llobet, *Angew. Chem., Int. Ed.* **2009**, *48*, 2842–2852.

08- K. N. Ferreira, T. M. Iverson, K. Maghlaoui, J. Barber and S. Iwata, *Science* **2004**, *303***,** 1831–1838.

09- J. Yano, J. Kern, K. Sauer, M. J. Latimer, Y. Pushkar, J. Biesiadka, B. Loll, W. Saenger, J. Messinger, A. Zouni and V. K. Yachandra, *Science* **2006**, *314*, 821–825.

10- J. P. McEvoy and G. W. Brudvig, *Chem. Rev.* **2006,** *106*, 4455–4483.

11- A. W. Rutherford and A. Boussac, *Science* **2004**, *303*, 1782–1784.

12- M. Haumann, P. Liebisch, C. Müller, M. Barra, M. Grabolle and H. Dau, *Science* **2005**, *310*, 1019–1021.

13- L. Hammarström and S. Styring, *Phil. Trans. R. Soc. B* **2008**, *363*, 1283–1291.

14- J. A. Gilbert, D. S. Eggleston, W. R. Murphy, *Jr.* D. A. Geselovitz, S. W. Gersten, D. J. Hodgson and T. J. Meyer, *J. Am. Chem. Soc.* **1985**, *107*, 3855–3864.

15- T. Wada, K. Tsuge and K. Tanaka, *Angew. Chem., Int. Ed. Engl.* **2000**, *39*, 1479–1482.

16- C. Sens, I. Romero, M. Rodrıguez, A. Llobet, T. Parella and J. Benet-Buchholz, *J. Am. Chem. Soc.* **2004**, *126*, 7798–7799.

17- J. K. Hurst, *Coord. Chem. Rev.* **2005**, *249*, 313–328.

18- R. Zong and R. P. Thummel, *J. Am. Chem. Soc.* **2005**, *127*, 12802–12803.

19- P. Kurz, G. Berggren, M. F. Anderlund and S. Styring, *J. Chem. Soc. Dalton Trans.* **2007**, 4258–4261.

20- M. W. Kanan and D. G. Nocera, *Science* **2008,** *321*, 1072–1075.

21- J. Limburg, J.S. Vrettos, L.M. Liable-Sands, A.L. Rheingold, R.H. Crabtree and G.W. Brudvig, *Science* **1999**, *283*, 1524–1527.

22- Z. Deng, H.-W. Tseng, R. Zong and R. Thummel, *Inorg. Chem.* **2008**, *47*, 1835-1848.

23- F. Liu, T. Cardolaccia, B. J. Hornstein, J. R. Schoonover and T. J. Meyer, *J. Am. Chem. Soc.* **2007**, *129*, 2446–2447.

24- W. F. Ruettinger, C. Campana and G. C. Dismukes, *J. Am. Chem. Soc.* **1997,** *119,* 6670–6671.

25- J. Mola, E. Mas-Marza, X. Sala, I. Romero, M. Rodriguez, C. Viñas, T. Parella and A. Llobet, *Angew. Chem. Int. Ed.* **2008**, *47*, 5830–5832.

26- J. T. Muckerman, D. E. Polyansky, T. Wada, K. Tanaka and E. Fujita, E. *Inorg. Chem.* **2008**, *47*, 1787–1802.

27- C.W. Cady,R. H. Crabtree and G. W. Brudvig, *Coord. Chem. Rev.* **2008**, *252*, 444–455.

28- R. Rarnaraj, A. Kira and M. Kaneko, *Angew. Chem. Int. Ed. Engl.* **1986,** *25*, 1009–1011.

29- S.Yamashita, K. Nagoshi, M. Yagi amd M. Kaneko, *J. Mol. Catal. A* **2000**, *153*, 209–214.

30- M. Yagi, E. Takano and M. Kaneko, *Electrochim. Acta* **1999**, *44*, 2493–2497.

31- M. Yagi, K. Kinoshita and M. Kaneko, *Electrochim. Acta* **1999**, *44*, 2245–2250.

32- R. Rarnaraj and M. Kaneko, *J. Mol. Catal.* **1993**, *81*, 319–332.

33- G. J. Yao, A. Kira and M. Kaneko, *J. Chem. Soc. Faraday Trans.1* **1988**, *84*, 4451–4456.

34- R. Ramaraj, A. Kira and M. Kaneko, *J. Chem. Soc. Faraday Trans.1* **1987**, *83,* 1539–1551.

35- D. E. Burchfield and R. M. Richman, *Inorg. Chem.* **1985**, *24,* 852–857.

36- S. Trasatti, *Electrochim. Acta* **1984,** *29*, 1503–1512.

37- M. Yagi, Y. Takahashi, I. Ogino and M. Kaneko, *J. Chem. Soc., Faraday Trans.* **1997**, *93*, 3125–3127.

38- M. Yagi, I. Ogino, A. Miura, Y. Kurimura and M. Kaneko, *Chem. Lett.* **1995**, *24*, 863.

39- I. Ogino, K. Nagoshi, M. Yagi and M. Kaneko, *J. Chem. Soc., Faraday Trans.* **1996**, *92*, 3431–3434.

40- J. Haenen, W. Visscher and E. Barendrecht, *J. Electroanal. Chem.* **1986**, *208*, 273–296.

41- M. Vuković, *J. Chem. Soc. Faraday Trans.* **1990**, *86*, 3743–3748.

42- Y. Hu, Y. V. Tolmachev and D. A. Scherson, *J. Electroanal. Chem.* **1999**, *468*, 64–69.

43- (a) S. Han, J. Zhai, L. Shi, X. Liu, W. Niu, H. Li and G. Xu, *Electrochem. Commun.* **2007**, *9*, 1434–1438. (b) M.-G. Vergé, P. Mettraux, C.-O.A. Olsson and D. Landolt, *J. Electroanal. Chem.* **2004**, *566*, 361–370.

44- U. A. Paulus, T. J. Schmidt, H. A. Gasteiger and R. J. Behm, *J. Electroanal. Chem.* **2001**, *495*, 134–145.

45- P. R. Birkin, J. M. Elliott and Y. E. Watson, *Chem. Commun.* **2000**, 1693–1694.

46- R. Kötz, S. Stucki, D. Scherson and D. M. Kolb, *J. Electroanal. Chem.* **1984**, *172*, 211–219.

47- M. Wohlfahrt-Mehrens and J. Heitbaum, *J. Electroanal. Chem.* **1987**, *237*, 251–260.

48- H. Ma, C. Liu, J. Liao, Y. Su, X. Xue and W. Xing, *J. Mol. Catal. A: Chemical* **2006**, *247*, 7–13.

49- J. M. Friedman, D. L. Rousseau, G. Navon, S. Rosenfeld, P. Glynn and K. B. Lyons, *Arch. Biochem. Biophys.* **1979**, *193*, 14–21.

50- M. Itabashi, K. Shoji and K. Itoh, *Chem. Lett.* **1981**, *10*, 491–494.

51- M.A.A.F. de C.T. Carrondo, W.P. Griffith, J.P. Hall and A.C. Skapski, *Biochimica et Biophysica Acta* **1980**, *627*, 332–334.

52- J. M. Fletcher, B. F. Greenfield, C. J. Hardy, D. Scargill and J. L. Woohead, *J. Chem. Soc. (Lond.)* **1961**, 2000–2006.

53- J. E. Earley and T. Fealey, *Inorg. Chem.* **1973**, *12*, 323–327.

54- J. R. Campbell, R. J. H. Clark, W. P. Griffith and J. P. Hall, *J. Chem. Soc., Dalton Trans.***1980**, 2228–2236.

55- S. A. Wasileski, M. T. M. Koper and M. J. Weaver, *J. Chem. Phys.* **2001**, *115*, 8193-8203.

56- S. Bhaskar, P. S. Dobal, S. B. Majumder and R. S. Katiyara, *J. Appl. Phys.* **2001**, *89*, 2987–2992.

57- S. Y. Mar, C. S. Chen, Y. S. Huang and K. K. Tiong, *Appl. Surf.Sci.* **1995**, *90*, 497–504.

58- (a) A. H. Wonders, T. H. M. Housmans, V. Rosca and M. T. M. Koper, *J. Appl. Electrochem.* **2006**, *36*, 1215-1221. (b) M. Duca, M. O. Cucarella, P. Rodriguez and M. T. M. Koper, *J. Am. Chem. Soc.* **2010**, *132*, 18042–18044.

59- (a) S. C. S. Lai, S. E. F. Kleyn, V. Rosca and M. T. M. Koper, *J. Phys. Chem. C*, **2008**, *112*, 19080–19087. (b) P. Corio and J. C. Rubim, *J. Raman Spectrosc.* **1997**, *28*, 235–241.

60- P. Gao, D. Gosztola, L. W. H. Leung and M. J. Weaver, *J. Electroanal. Chem.* **1987**, *233*, 211–222.

61- A. Sarapuu, A. Kasikov, T. Laaksonen, K. Kontturi and K. Tammeveski, *Electrochim. Acta* **2008**, *53*, 5873–5880.

62- C.-C. Hu and Y.-H. Huang, *Electrochim. Acta* **2001**, *46*, 3431–3444.

Appendix A2

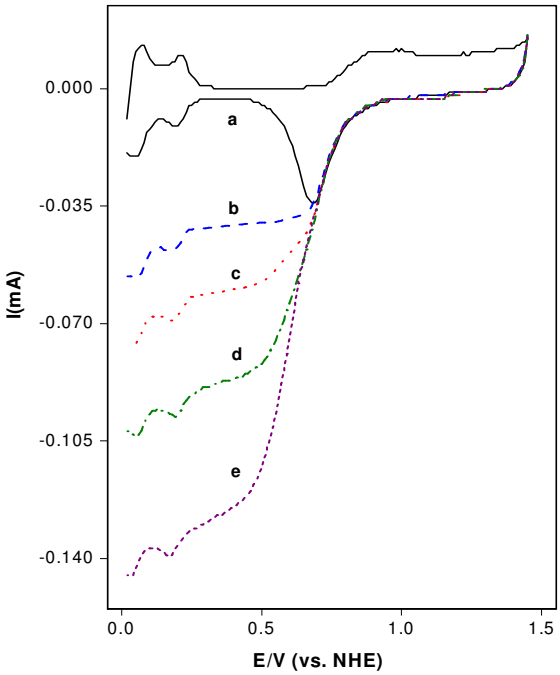

Figure A2.1.
Current potential curves for oxygen reduction on the Pt ring at Au_{disk} potentials (a) 0.0 V, (b) 1.75 V, (c) 1.85 V, (d) 1.95 V and (e) 2.05 V in deoxygenated Ar-saturated 0.1 M H_2SO_4 solution at 700 rpm, scan rate 20 mV/sec, E/V vs. NHE. Pt_{ring} was potentiostated at 0.44 V (vs. NHE).

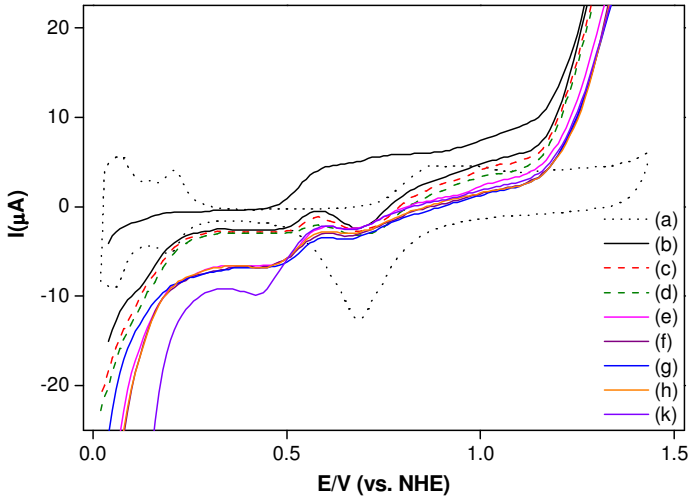

Figure A2.2. Current potential curves for oxygen reduction on the Pt ring in deoxygenated 0.1 M H_2SO_4 solution without Ru-red at Au_{disk} potentials (a) 0.0 V and in deoxygenated 0.1 M H_2SO_4 solution containing 0.035 mM Ru-red at (b) 0.0 V, (c) 1.21 V, (d) 1.22 V, (e) 1.23 V, (f)1.25 V, (g) 1.30 V (h) 1.40 V and (k) 1.50 V. Oxygen is generated by catalytic water oxidation in the presence of Ru-red in the aqueous electrolyte solution. Rotation rates were 700 rpm, scan rates 20 mV/sec and the ring potential was 0.44 V (vs. NHE).

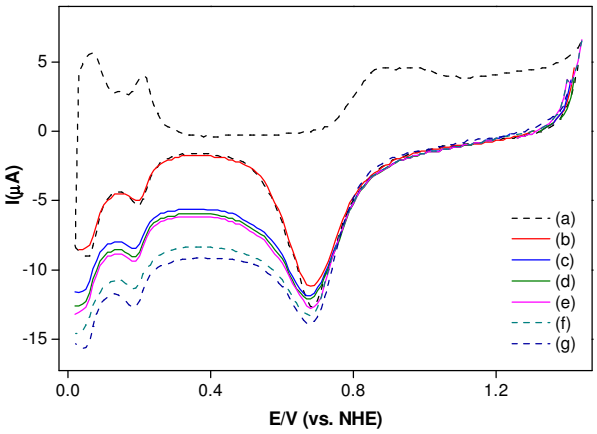

Figure A2.3.
Current potential curves for oxygen reduction on the Pt ring at Au_{disk} [functionalized with Ru-red (RRA)] potentials (a) 0.0 V, (b) 1.43 V, (c) 1.44 V, (d) 1.45 V, (e) 1.50 V, (f) 1.75 V and (g) 1.85 V in deoxygenated 0.1 M H_2SO_4 electrolyte solution. Oxygen is generated by catalytic water oxidation on the RRA. Rotation rates were 700 rpm, scan rates 20 mV/sec and the ring potential was 0.44 V (vs. NHE).

Figure A2.4.

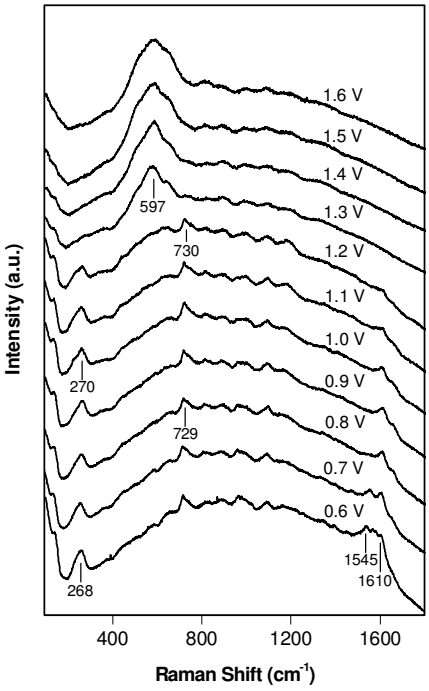

Figure A2.5.

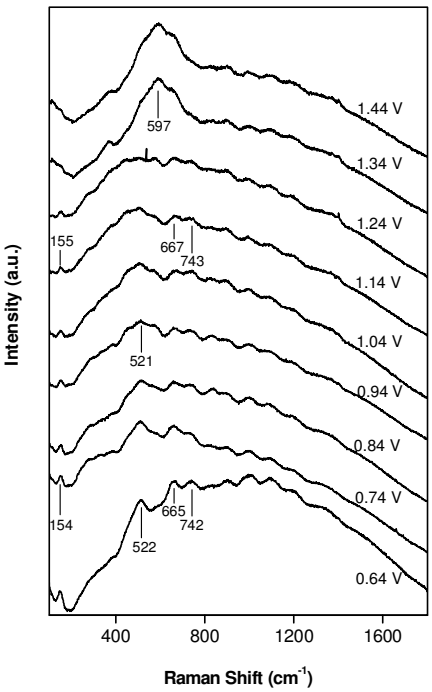

Figure A2.4. *In situ* electrochemical SERS spectra of a freshly polished and roughened Au_{disk} electrode at selected potentials in deoxygenated Ar-saturated 0.1 M H_2SO_4 aqueous electrolyte without Ru-red in solution. The starting potential was 0.6 V and was successively incremented up to 1.6 V (vs. NHE).

Figure A2.5. Selected potential-dependent *in situ* electrochemical SER spectra for a hydrous ruthenium oxide ($RuO_x \cdot nH_2O$) film that was freshly electrodeposited on a roughened Au_{disk} electrode and scanned in the deoxygenated and Ar-saturated 0.1 M H_2SO_4 electrolyte solution. The starting potential was 0.6 V and was successively incremented up to 1.4 V (vs. NHE).

Chapter 3

Mono Ruthenium Catalysts for Water Splitting

ABSTRACT

A class of single site homogeneous water splitting catalysts is presented in this chapter that shows for the first time a four-step proton coupled electron transfer (PCET) pathway for molecular oxygen generation by a bifunctional proton management mechanism to stabilize a divalent catalyst complex during the four-electron water oxidation cycle. The *p*-cymene mononuclear ruthenium derived water oxidation complexes with dinitrogen ligands are easily accessible and relatively inexpensive compared to other available ruthenium complexes. The aqua exchange induction step levels the chemical potential in the PCET water oxidation cycle by facilitating the proton release. Since water ligation contributes with two hydrogen atoms, it activates the complex for two consecutive PCET steps with a very similar proton management system. The aqua ligation of the $[Ru^{IV}(=O)]^{2+}$ complex at the beginning of the second half of the catalytic cycle is facilitated by a large bite angle and a wide coordination gap between the dinitrogen ligand bound to Ru and the aromatic moiety. A mechanism is proposed where the donating *p*-cymene stabilizes the $[Ru^{IV}(=O)]^{2+}$ state and prevents its further oxidation to the $[Ru^{V}(=O)]^{3+}$ complex before second OH_2 insertion. In this way the catalyst cycles through $Ru^{II/III/IV}$–$Ru^{III/IV/II}$ states with two water molecules coordinating sequentially while maintaining an overall charge +2. The free energy differences while going from HO* to HOO* are 3.1, 3.13 and 3.08 eV for $[(cy)Ru^{II}(bpy)OH_2]^{2+}$, $[(cy)Ru^{II}(phen)OH_2]^{2+}$ and $[(cy)Ru^{II}(bpm)OH_2]^{2+}$ complexes respectively, which is well in line with the free energy difference determined for a wide range of catalysts and within the standard range of 3.2 ± 0.1 eV [1].

Based on: K.S. Joya and H.J.M. de Groot, **2011** (*to be submitted*)

3.1. INTRODUCTION

Hydrogen generation from water splitting is difficult, and an efficient oxygen evolving complex that can be widely applied is still missing [1-3]. In particular, the development of a molecular system operating at moderate activation energies with high activity and rate for oxygen evolution is challenging from a catalytic standpoint [4-9]. It is well established that a four step PCET pathway is a key element for an efficient operation of the oxygen evolving complex (OEC) in natural photosynthesis, and the oxo-manganese cluster embedded in photosystem-II (PS-II) provides insight for the design of artificial substitutes [10-13]. Mono site ruthenium and iridium complexes have been reported that are active for water oxidation without a four step PCET reaction coordinate for oxygen evolution [13-15]. For the single-site ruthenium systems steric crowding reduces the accessibility of the complex for catalysis. In parallel, a relatively strong electron affinity of the tri-nitrogen ligands induces the formation of a $[Ru^{V}(=O)]^{3+}$ complex by one electron oxidation of $[Ru^{IV}(=O)]^{2+}$ [15,16]. As the formation of the $[Ru^{V}(=O)]^{3+}$ complex is not coupled to deprotonation of the complex with the second OH_2, the net build up of positive charge limits the maximum attainable rate, even in aqueous solution at higher pH [7].

A successive four-step PCET for the entire complex is a prerequisite for an optimal catalyst, since it facilitates the build up of redox equivalents by circumventing the high energy intermediates during multi-electron water splitting [12-14]. From a thermodynamics perspective, an ideal water oxidation catalyst operates along a reaction coordinate with an equilibrium potential of 1.23 V for each intermediate oxidation step [14,17]. The total free energy change for the formation of oxygen from H_2O is 4.92 eV, which is realized by the extraction of four electrons and protons by consecutive PCET steps from two water molecules [17,18]. In oxo-bridged binuclear ruthenium complexes, the oxygen formation proceeds via nucleophilic attack of OH_2 on the oxo ligand to generate the higher energy HOO* intermediate [19,20]. Among the various intermediates that can be

produced during catalysis by mono-site systems, the formation of the peroxide (HOO*) from $[Ru^{IV}=O]^{2+}$ acquires high energy since it is thought to proceed by a non-PCET step with a prior conversion into $[Ru^{V}=O]^{3+}$ instead of second aqua ligation and PCET to maintain a Ru^{IV} species [15,16].

The catalyst bound HOO* intermediate produced in the second half of the water oxidation cycle is difficult to oxidize compared to the hydroxide (HO*) in the first catalytic PCET step. It has been found empirically that there is an energy difference of 3.2±0.1 eV between the HOO* and HO* intermediates along the catalysis pathway [14,17]. Depending on the chemical nature of the catalyst, either the =O intermediate or the -OOH transition determines the overall energy for the four-electron water oxidation process, and the free energy of the =O intermediate can vary among catalysts, relative to the average of the positioning of the -OH and the -OOH intermediates on the reaction coordinate [17,18].

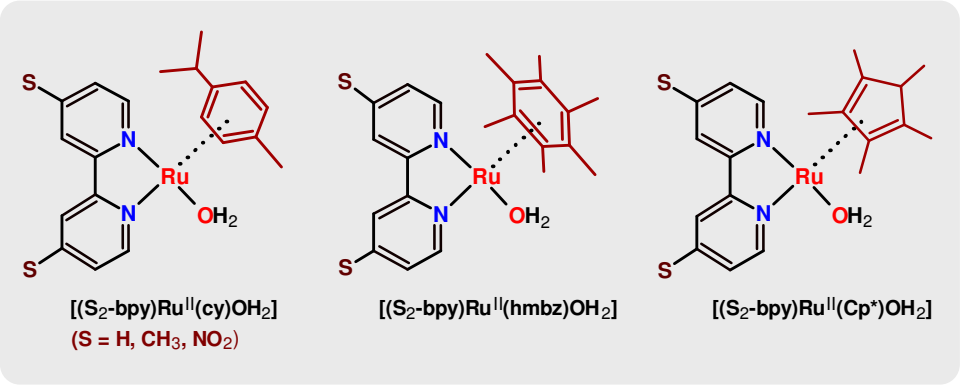

Figure 3.1. Ruthenium *p*-cymene (cy), hexamethyl benzene (hmbz) or pentamethyl-cyclopentadiene (Cp*) derived simple and 4,4′-disubstituted-2,2′-bipyridine, phenanthroline or bipyrimidine mono nuclear complexes [21].

This chapter describes a class of *p*-cymene (cy) derived single site ruthenium complexes (Fig. 3.1). The water splitting system for homogeneous catalysis is derived from Ru-cy complexes that are chemically preprogrammed with the bidentate ligands (L) like simple 2,2′-bipyridine (bpy) and 4,4′-disubstituted 2,2′-bipyridine (S_2-bpy), 1,10-phenanthroline (phen) and 2,2′-bipyrimidine (bpm) for

enhanced electron donation to the metal core from the aromatic moiety [21]. In combination with aqua ligation this produces a push-pull mechanism that can stabilize the $[Ru^{IV}(=O)]^{2+}$ state by partial charge transfer from the ligand in synergy with deprotonation. This prevents the further oxidation into $[Ru^{V}(=O)]^{3+}$ and facilitates the insertion of a second water molecule to the $[Ru^{IV}(=O)]^{2+}$ intermediate. It provides the first example of the formation of the $[Ru^{III}\text{-}(OOH)]^{2+}$ species from a $[Ru^{IV}(=O)]^{2+}$ complex by a PCET mechanism (Scheme 3.1). Homogeneous catalytic water oxidation was realized in aqueous acids in the presence of Ce(IV) as a one-electron oxidizing agent [16].

3.2. RESULTS AND DISCUSSION

3.2.1. Catalytic Complexes Synthesis and Characterization

The mono nuclear chloro complexes $[(L)Ru^{II}(cy)Cl]^{+}$ (**Ru**–L) were obtained in good purity and high yield (~ 70 %) by stirring a mixture of the $[RuCl_2(p\text{-cymene})]_2$ dimer with the respective ligand in methanol or acetone. The orange complexes were isolated and further purified by reprecipitation from acetone or methanol solution. The simple and 4,4′-disubstituted-2,2′-bipyridine, phen or bpm coordinate to the ruthenium upon cleavage of the dichloride bridge of the $[RuCl_2(p\text{-cymene})]_2$ dimer [22,23]. The purity and composition of the complexes were analyzed by proton NMR and by elemental analysis (see Materials and Methods for details and Fig. A3.1).

The exchange of the negatively charged chloride anion with a neutral aqua molecule in chloro complexes $[(L)Ru^{II}(cy)Cl]^{+}$ is accompanied by a colour change from orange-yellow to bright-yellow that was be followed in time with UV-vis spectroscopy (Fig. 3.2). The crystal structures of the similar complexes have been determined by X-ray diffraction and revealed a trans configuration of the dinitrogen ligand with respect to the *p*-cymene [23-25]. This structural configuration has a wide coordination gap between the bpy-Ru and the *p*-cymene ligand [24]. The aqua versions $[(L)Ru^{II}(cy)\text{-}OH_2]^{2+}$ (Cat.**Ru**–L) of the chloro

complexes were readily obtained, either *in situ* by dissolving in aqueous solution, or by stirring with stoichiometric aliquots of aqueous $AgNO_3$ or $AgPF_6$ in a methanol-water mixture.

3.2.2. Optical Measurements and Electrochemical Studies

The aqua exchange in $[(bpy)Ru^{II}(cy)\text{-}Cl]^+$ (**Ru**–bpy) is accompanied by a colour change from orange-yellow to bright-yellow for the $[(bpy)Ru^{II}(cy)\text{-}OH_2]^{2+}$ catalyst (Cat.**Ru**–bpy), as indicated by a pronounced change of the optical absorption profile in the spectral region between 300 nm and 500 nm (Fig. 3.2). Above pH=9, a broad band appears between 420 nm and 525 nm, indicating the deprotonated complex $[(L)Ru^{II}(cy)\text{-}OH]^+$ in the alkaline medium. This is accompanied by a colour change from yellow to light-brown and darkening of the colour on further pH increase. These colour changes are attributed to exchange of chloride by a neutral water molecule at the catalytic ruthenium sites in the aqueous medium, followed by deprotonation of OH_2 into HO^-, depending on the pH of the solution.

The cyclic voltammetry of the mono ruthenium complexes with $[(terpy)\text{-}Ru\text{-}(N\text{-}N)]^{n+}$ and $[(Mebimpy)\text{-}Ru\text{-}(N\text{-}N)]^{n+}$ scaffolds (terpy is 2,2′:6″,2″-terpyridine; Mebimpy is 2,6-bis(1-methylbenzimidazol-2-yl)-pyridine ligand; N-N is 2,2′-bipyridine, 2,2′-bipyrimidine or 2,2′-bipyrazine), reveals two primary oxidation steps. For the Mebimpy-Ru-bpy complex, the reaction proceeds via two consecutive PCET steps generating the two Ru redox couples $[Ru^{III}\text{-}(OH)]^{2+}/[Ru^{II}\text{-}(OH_2)]^{2+}$ and $[Ru^{IV}(=O)]^{2+}/[Ru^{III}\text{-}(OH)]^{2+}$ at 0.81 V and 1.27 V (vs. NHE) respectively (pH=1) [7,15,16]. The two transitions show an approximately 60mV/pH shift while moving from an acidic to alkaline solution of pH~11-12. Further increase of the electrode potential produced a third oxidation of the catalytic site to form a $[Ru^{V}(=O)]^{3+}$ type complex from $[Ru^{IV}(=O)]^{2+}$ at > 1.67 V for $[(Mebimpy)\text{-}Ru\text{-}(bpy)]^{n+}$ and at *ca.* 1.80 V for $[(terpy]\text{-}Ru\text{-}(bpy)]^{n+}$ just before the second water insertion (Table 3.1). This oxidation is thought to be only an electron removal process, and water ligation is required to enable the proton release in a $[Ru^{III}\text{-}(OOH)]^{2+}/[Ru^{V}(=O)]^{3+}$ couple [16,19].

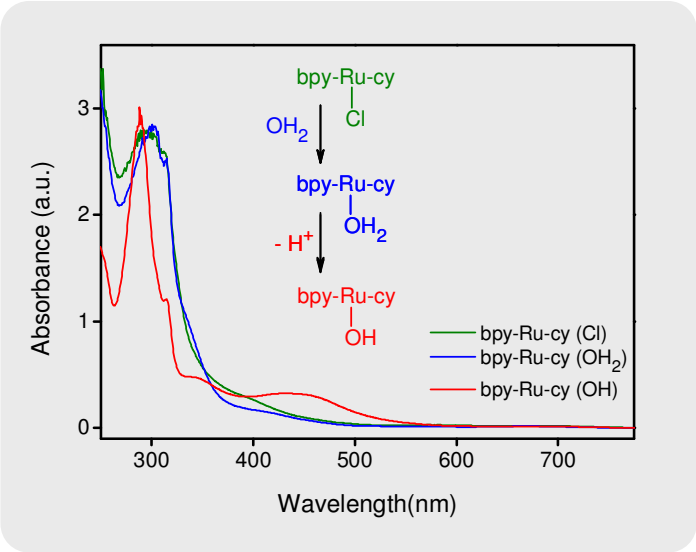

Figure 3.2. Electronic absorption spectra of the $[(bpy)Ru(cy)-(Cl)]^{+}$ complex (green line) following blue curve attributed to the formation of $[(bpy)Ru(cy)-(OH_2)]^{2+}$ catalyst induced by aqua exchange and deprotonation of the aqua $[(bpy)Ru(cy)-(OH_2)]^{2+}$ complex to form $[(bpy)Ru(cy)-(OH)]^{+}$ (red line). For all measurements a concentration of the complex of 7.5×10^{-5} M was used.

In this study, CV measurements for the complexes $[(bpy)Ru(cy)-(OH_2)]^{2+}$, $[(bpm)Ru(cy)-(OH_2)]^{2+}$ and $[(phen)Ru(cy)-(OH_2)]^{2+}$ were performed with a scan rate of 100 mV per second to avoid the weak polarization signals due to slow electrode kinetics of ruthenium oxidation in the complex that could occur at lower scan rate [16,26]. The current waves for the redox pairs $[Ru^{III}-(OH)]^{2+}/[Ru^{II}-(OH_2)]^{2+}$ and $[Ru^{IV}(=O)]^{2+}/[Ru^{III}-(OH)]^{2+}$ are observed around 0.51 – 0.61 V and 1.15 – 1.20 V (pH=1), respectively. The electrochemistry of Cat.**Ru**–bpy in aqueous acid reveals polarization waves for $[Ru^{III}-(OH)]^{2+}/[Ru^{II}-(OH_2)]^{2+}$ and $[Ru^{IV}(=O)]^{2+}/[Ru^{III}-(OH)]^{2+}$ representing two consecutive PCET steps as established before for mono ruthenium polypyridyl complexes [16,19]. These first two oxidation steps for the catalytic cycle of $[(bpy)Ru(cy)-(OH_2)]^{2+}$ appear at $E_{1/2}$ *ca*. 0.55 V and 1.19 V vs. NHE (Fig. A3.2a).

Further cycling of the potential leads to the formation of $[Ru^{III}\text{-}(OOH)]^{2+}$ from the $[Ru^{IV}(=O)]^{2+}$ species on the second aqua ligation, which is visible as a shoulder just above *ca*. 1.65 V, irreversible and superimposed on the background signal (Fig. A3.2a). This is followed by $[Ru^{IV}\text{-}(OO)]^{2+}/[Ru^{III}\text{-}(OOH)]^{2+}$ conversion with subsequent oxygen release above 1.81 V, observed as tiny bubbles on the working electrode surface during forward scans. The sequential oxidation of the $[Ru^{II}\text{-}OH_2]^{2+}$ complex into $[Ru^{III}\text{-}(OH)]^{2+}$, $[Ru^{IV}(=O)]^{2+}$ and the peroxo intermediate $[Ru^{III}\text{-}(OOH)]^{2+}$ was also monitored spectro-photometrically by titrating with stoichiometric aliquots of cerium ammonium nitrate (CAN) and observing the absorption in the 275-400 nm range (Fig. A3.3). The spectral changes are consistent with the generation of the $[Ru^{III}\text{-}(OH)]^{2+}$, $[Ru^{IV}(=O)]^{2+}$ redox pairs in the first half and $[Ru^{III}\text{-}(OOH)]^{2+}$ and $[Ru^{IV}\text{-}(OO)]^{2+}$ species in the second part of the water oxidation cycle, as reported earlier for $[terpy\text{-}Ru\text{–}(N\text{-}N)]^{n+}$ type mono nuclear complexes [15,16].

In neutral solution, $[Ru^{III}\text{-}(OH)]^{2+}/[Ru^{II}\text{-}(OH_2)]^{2+}$ and $[Ru^{IV}(=O)]^{2+}/[Ru^{III}\text{-}(OH)]^{2+}$ intermediates exhibit quasireversible transitions and produce relatively weak polarization currents (Fig. A3.2b). This is attributed to slow reversible electrode kinetics of the complex on the electrode in the neutral phase and to electroprecipitation effects in the phosphate buffer solution [26]. The electrochemical data for the catalyst in aqueous solution confirm that two redox couples, $[Ru^{III}\text{-}(OH)]^{2+}/[Ru^{II}\text{-}(OH_2)]^{2+}$ and $[Ru^{IV}(=O)]^{2+}/[Ru^{III}\text{-}(OH)]^{2+}$, produce a ~60 mV/pH shift characteristic of Nernst behaviour, while going from aqueous acid to a neutral solution (Fig. A3.2) and this validates the two consecutive PCET steps [19]. The electrochemical transition for $[Ru^{III}\text{-}(OOH)]^{2+}/[Ru^{IV}(=O)]^{2+}$ intermediate takes place at *ca*. 1.42 V (vs. NHE) during the forward scan in the neutral phase, while the reverse potential cycling reveals a reduction wave for the $[Ru^{IV}(=O)]^{2+}/[Ru^{III}\text{-}(OOH)]^{2+}$ couple at *ca*. 1.36 V vs. NHE (Fig. A3.2b). The pH dependence for the $[Ru^{III}\text{-}(OOH)]^{2+}/[Ru^{IV}(=O)]^{2+}$ transition is also consistent with Nernst behaviour for a third consecutive PCET step in the catalytic cycle of the $[(bpy)Ru(cy)\text{-}(OH_2)]^{2+}$ catalyst.

3.2.3. Pourbaix Diagrams

The Pourbaix diagrams (potential vs. pH plots) for the complexes were constructed from CV's obtained in aqueous solutions at various pH. The potential vs. pH plot for Cat.**Ru**–bpy is presented in Figure 3.3 and shows three pH-dependent current potential profiles with the characteristic Nernst slope of *ca.* 60 mV/pH for the observable ruthenium couples $[Ru^{III}\text{-}(OH)]^{2+}/[Ru^{II}\text{-}(OH_2)]^{2+}$, $[Ru^{IV}(=O)]^{2+}/[Ru^{III}\text{-}(OH)]^{2+}$ and $[Ru^{III}\text{-}(OOH)]^{2+}/[Ru^{IV}(=O)]^{2+}$ (Figs. A3.4). The $[(N\text{-}N)Ru^{IV}=O(cy)]^{2+}$ complexes do not form the higher $[Ru^{V}(=O)]^{3+}$ oxidation state complex that was reported recently for other classes of mono ruthenium catalysts and is generated at high potential, above 1.67 V (vs. NHE) at pH=1 [7,16]. The pH dependence of the potential for the $[Ru^{III}\text{-}(OOH)]^{2+}/[Ru^{IV}(=O)]^{2+}$ redox couple is attributed to insertion of a second water molecule at the $[(N\text{-}N)Ru^{IV}=O(cy)]^{2+}$ stage that makes it possible to avoid the further oxidation of the ruthenium core and the formation of a $[Ru^{V}(=O)]^{3+}$ species [19]. The affinity of the $[Ru^{IV}(=O)]^{2+}$ species for the coordination of the second water molecule is stabilized by the donating nature of the isopropyl and methyl substituted aromatic ligand towards the ruthenium centre.

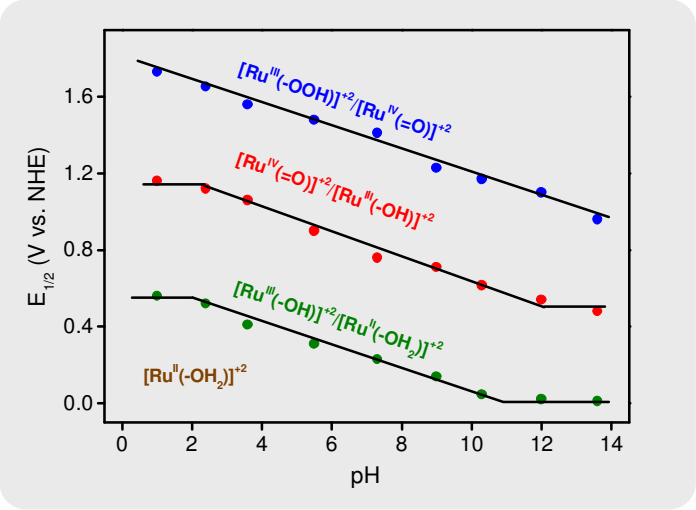

Figure 3.3. Pourbaix diagram for $[(bpy)Ru^{II}(OH_2)(cy)]^{2+}$ showing the ruthenium couples $[Ru^{III}(OH)]^{2+}/[Ru^{II}(OH_2)]^{2+}$, $[Ru^{IV}(=O)]^{2+}/[Ru^{III}(OH)]^{2+}$ and $[Ru^{III}(OOH)]^{2+}/[Ru^{IV}(=O)]^{2+}$. The electrochemical data were generated from CV's obtained on a glassy carbon working electrode in 0.1 M aqueous solutions.

The large bite angle between bpy-Ru and the aromatic ligand that facilitates the aqua exchange in the catalyst induction step can promote second aqua ligation as well [22,23]. The higher oxidation state of the catalyst generated after ligation of a second water molecule is attributed to the $[Ru^{III}\text{-}(OOH)]^{2+}$ and $[Ru^{IV}(\text{-}OO)]^{2+}$ forms preceeding oxygen evolution [15]. Both higher potential ruthenium couples are produced by pH-dependent PCET oxidation of the $[Ru^{IV}(=O)]^{2+}$ complex after insertion of the second water molecule, and without undergoing a transformation into a $[Ru^{V}(=O)]^{3+}$ type species [16,19]. Hence this catalytic system exhibits a consecutive four step PCET oxidation process for water oxidation and molecular oxygen formation (Scheme 3.1). Thus, proton release is not rate-limiting and is accompanying the release of an electron in the ruthenium redox couples in $[(N\text{-}N)Ru^{II}(cy)\text{-}OH_2]^{2+}$ complexes. For all couples in the Pourbaix diagram the slope of ~60 mV/pH characteristic for PCET is observed, even at higher pH up to 12 (Fig. 3.3). This contrasts with the detection of a pH-dependent slope only for the first half of the cycle in mononuclear Ru catalysts with tri-nitrogen ligands and Ir-bpy derived water oxidation catalysts [7,8].

3.2.4. Free Energies of Intermediates Along the Reaction Coordinate for the Water Oxidation Cycle

The standard free energy changes (ΔG) associated with the HO*, =O* and HOO* catalytic intermediates along the reaction coordinate for water oxidation and molecular oxygen formation for the $[(cy)Ru^{II}(bpy)OH_2]^{2+}$, $[(cy)Ru^{II}(phen)OH_2]^{2+}$ and $[(cy)Ru^{II}(bpm)OH_2]^{2+}$ complexes are calculated from the Pourbaix diagrams (pH=7) and transformed to a pH-independent reference frame that eliminates the 60 mV/pH shift. The total free energy change for the water oxidation process for an oxygen evolving catalyst operating at an optimal activity is $\Delta G = 4.92$ eV [18]. The dashed lines in Figure 3.4 represent the free energy levels for all intermediates of an optimal catalyst, with $\Delta G = 1.23$ eV for all four steps, similar to the natural PS-II [14,17]. For the HO*, =O* and HOO* intermediates, the free energy levels are at 1.23 eV, 2.46 eV and 3.69 eV respectively. Catalytic water oxidation can proceed

when all steps are downhill [1]. With the three sequential intermediates for the Cat.**Ru**–bpy cycle at ΔG = 0.67, 1.27, 1.83 eV (Fig. 3.4), and a total of 4.92 eV between the free energy of water and oxygen/hydrogen, the remaining free energy difference for the fourth step is ΔG = 1.15 eV. The free energy profile for Cat.**Ru**–phen and Cat.**Ru**–bpm is given in the Figures A3.5.

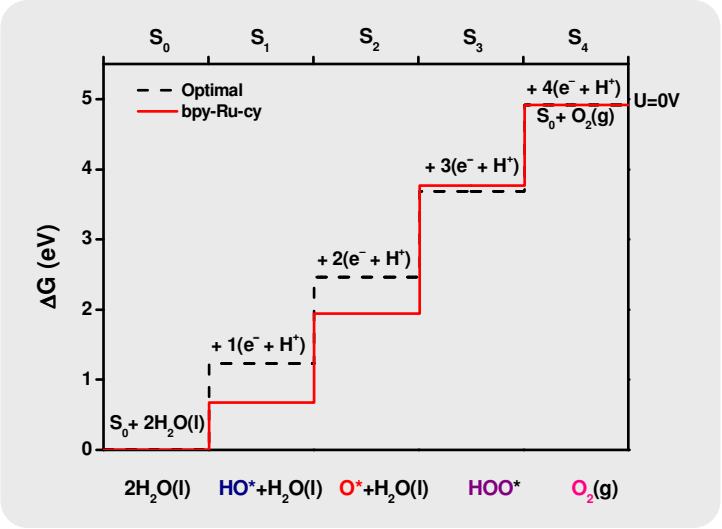

Figure 3.4. Relative Gibbs free energies (ΔG) of reactive species and intermediates along the reaction coordinate for water splitting and oxygen generation for the $[(bpy)Ru^{II}(OH_2)(cy)]^{2+}$ (Cat.**Ru**–bpy) [red solid line] catalytic system, compared with the free energy profile for an optimal catalyst (black dashed lines) with four equal steps of 1.23 eV [14,17].

The ΔG for the formation of the HOO* species determines the activation barrier and gives rise to the overpotential, which is ~ 0.6 V for the three catalyst complexes, close to the theoretical minimum of 0.4 V overpotential for a mononuclear catalyst complex [17,18], suggesting that the $[(cy)Ru^{II}(bpy)OH_2]^{2+}$, $[(cy)Ru^{II}(phen)OH_2]^{2+}$ and $[(cy)Ru^{II}(bpm)OH_2]^{2+}$ complexes are good artificial catalysts for water splitting that operate via a four PCET step mechanism (Figs. A3.5). Rosmeissl *et al.* suggested that the free energy of the oxide intermediate can be adjusted independently of either HO* or HOO*, but normally the =O intermediate or the -OOH intermediate determines the overall energy for the four-

electron water oxidation process [1,17]. For mono-metal catalytic centers, the free energy difference between the HOO* and the HO* intermediate is 3.2±0.1 eV [1]. The energy differences for the $[(cy)Ru^{II}(bpy)OH_2]^{2+}$, $[(cy)Ru^{II}(phen)OH_2]^{2+}$ and $[(cy)Ru^{II}(bpm)OH_2]^{2+}$ complexes are 3.1, 3.13 and 3.08 eV, respectively, well within the standard range [17,18].

3.2.5. Catalytic Water Oxidation

Catalytic homogeneous water oxidation was conducted *in situ* in an airtight glass cell and oxygen evolution was measured with a calibrated oxygen electrode connected to a digital oxygen-meter. The chloro complexes and catalysts Cat.**Ru**–bpy, Cat.**Ru**–dmbpy, Cat.**Ru**–dnbpy, Cat.**Ru**–phen and Cat.**Ru**–bpm are water soluble and addition of Ce(IV) in the form of CAN (cerium ammonium nitrate) leads to the detection of oxygen formation from water splitting. In a characteristic experiment, 350 equivalents of Ce(IV) were added to the Ar-purged aqueous solution of the catalysts in 0.1 M HNO_3.

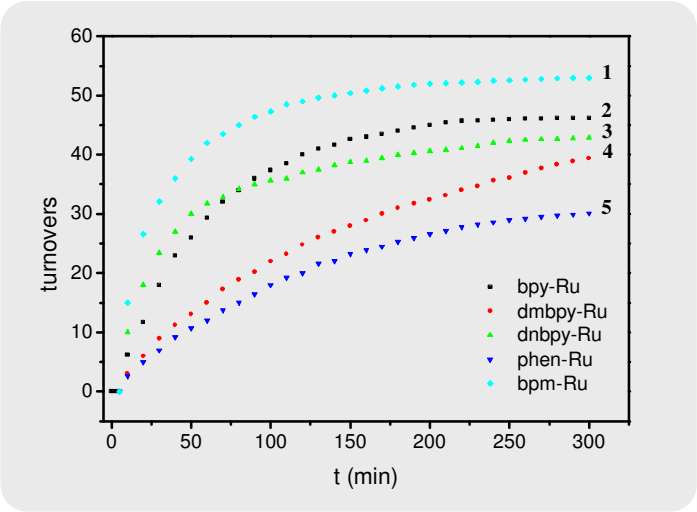

Figure 3.5. Oxygen turnovers vs. time during homogeneous water splitting catalysis by (1) $[(cy)Ru^{II}(bpm)\text{-}OH_2]^{2+}$, (2) $[(cy)Ru^{II}(bpy)\text{-}OH_2]^{2+}$, (3) $[(cy)Ru^{II}(dnbpy)\text{-}OH_2]^{2+}$, (4) $[(cy)Ru^{II}(dmbpy)\text{-}OH_2]^{2+}$ and (5) $[(cy)Ru^{II}(phen)\text{-}OH_2]^{2+}$ with 350 eq. of Ce(IV) in aqueous deoxygenated 0.1 M HNO_3.

The oxygen generation turnovers obtained for Cat.**Ru**–L in 5 hours of catalysis are shown in Figure 3.5 (Table A3.1). Cat.**Ru**–bpm and Cat.**Ru**–dnbpy show a rapid initial oxygen generation rate with >40 and >30 turnovers respectively, in 50 minutes. The highest initial rapid response for catalytic oxygen evolution by the $[(bpm)Ru^{II}(OH_2)(cy)]^{2+}$ complex is ascribed to the presence of two nitrogen atoms in 2,2′-bipyrimidine that are more electron withdrawing compared to the two carbon atoms in the 4,4′-position of the 2,2′-bipyridine ligand [16].

3.2.6. Water Oxidation Mechanism

A postulated pentacyclic catalytic mechanism for water oxidation, based on electrochemical investigations of the $[(L)Ru^{II}(cy)\text{-}OH_2]^{2+}$ complex and potential vs. pH behaviour from the Pourbaix diagram, is presented in Scheme 3.1. First, aqua ligation of the $[(L)Ru^{II}(cy)Cl]^{+}$ complex in the catalyst induction step leads to the formation of a stable divalent $[(L)Ru^{II}(cy)\text{-}OH_2]^{2+}$ molecular species with a chemical topology or connectivity pattern that is different from the chloride precursor. Apparently the combination of electron donating properties of the *p*-cymene and the dinitrogen ligand produce a pK_a shift, sufficient to transform the OH^- into a lewis base that stabilizes the adduct with the H^+, and leading to aqua ligation in a divalent form as opposed to OH^- ligation in a monovalent complex. Analogous forms of proton management have been encountered in biology, for instance in the complex counterion mechanism in the purple and blue forms of the transmembrane proton pump bacteriorhodopsin in the marine archebacterium *Halobacterium salinarium*, where the apparent pK_a is shifted by five units to stabilize a protonated species for light-driven biocatalysis and proton pumping in a concerted mechanism with a polyene electron donating moiety [28]. Thus, a bifactorial activation of the catalyst, a H_2X-Ru chemical topology in conjunction with a proton chemical potential bias, allows for two consecutive PCET steps. A PCET-ready species is formed by the addition of a proton that can be easily released again upon removal of an electron, while a second proton is also available for release upon extraction of a second electron by essentially the same mechanism.

Scheme 3.1. Proposed pentacyclic mechanism, based on electrochemical investigations, for homogeneous catalytic water oxidation by mono ruthenium $[(N\text{-}N)Ru^{II}(cy)\text{-}OH_2]^{2+}$ (N-N = bpy, dmbpy, dnbpy, phen, bpm) catalysts. During the catalyst induction step, the $[(N\text{-}N)Ru^{II}(cy)\text{-}Cl]^{+}$ complexes are transformed into the corresponding aqua version by exchanging Cl^- with neutral OH_2. Blue curved arrows represent four-step electron removal, with each step coupled to a proton transfer event, as indicated by green outward curved arrows. The oxidation states of the ruthenium possibly alternate through $Ru^{II}/Ru^{III}/Ru^{IV}$–$Ru^{III}/Ru^{IV}/Ru^{II}$, while maintaining an overall charge of +2. This is enabled by rapid association of a second water molecule, possibly accompanied by non rate-limiting internal rearrangements to generate $[Ru^{III}\text{-}(OOH)]^{2+}$ and $[Ru^{IV}\text{-}(OO)]^{2+}$ complexes by two successive PCET steps and eventually dioxygen release and water molecule insertion to recharge the system for the next catalytic cycle for water splitting and molecular oxygen evolution.

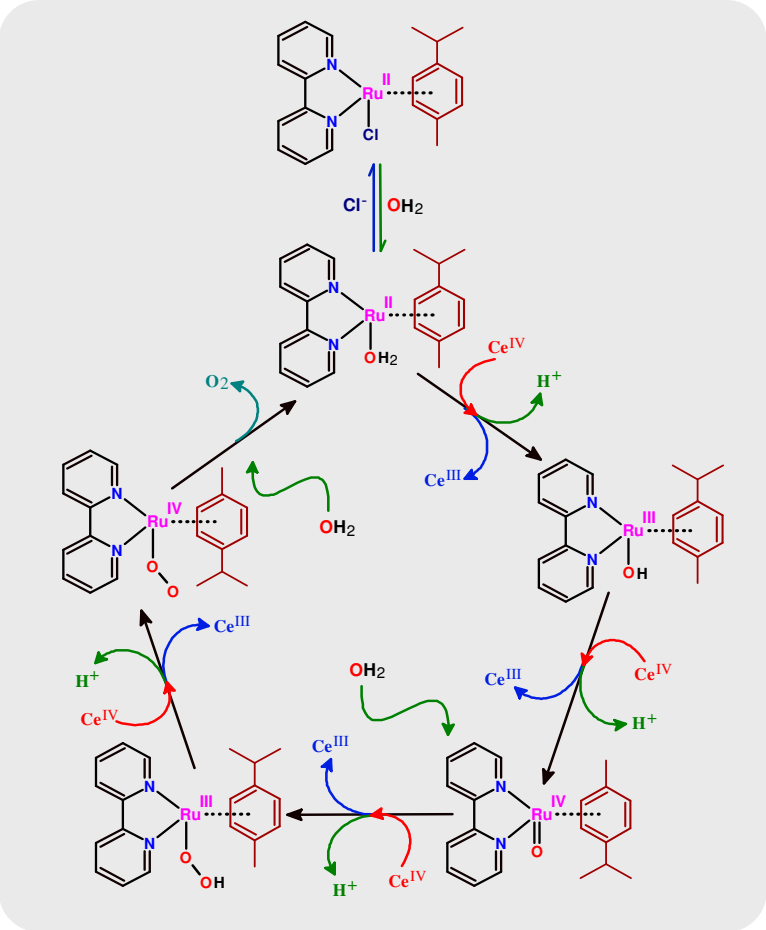

Subsequent insertion of a second water molecule re-establishes the proton management for the second half of the cycle and the activated form retains a double positive charge during the course of the whole catalytic cycle. Thus, on the addition

of Ce(IV) in the homogeneous phase, the $[(L)Ru^{II}(cy)\text{-}OH_2]^{2+}$ catalytic complexes loose two electrons in two stages, each coupled with a proton transfer event to form $[Ru^{III}\text{-}(OH)]^{2+}$ and $[Ru^{IV}(=O)]^{2+}$ consecutively. A wide coordination gap between the ruthenium bound dinitrogen ligand and the cymene probably provides a suitable environment for rapid second water molecule insertion with the catalytic sites, while the relatively strong electron donating property of the cymene aromatic ligand possibly prevents the formation of $[Ru^{V}(=O)]^{3+}$. This produces the first example of a $[Ru^{III}\text{-}(OOH)]^{2+}$ complex that operates fully with a four step PCET mechanism, similar to the natural PSII. The higher potential species, $[Ru^{III}\text{-}(OOH)]^{2+}$ and $[Ru^{IV}\text{-}(OO)]^{2+}$, are generated by two successive proton coupled electron transfer steps. Dioxygen is released from the $[Ru^{IV}\text{-}(OO)]^{2+}$ species on the addition of another water molecule, and this regenerates the $[(L)Ru^{II}(cy)\text{-}OH_2]^{2+}$ complex for the next catalytic cycle for water oxidation.

DFT calculations for ruthenium complexes with a tri-nitrogen ligand revealed that a seven-coordinate structure with a bidentate peroxide ligand is preferred over a six-coordinated structure with a terminal peroxido ligand [29,30]. In $[(L)Ru^{II}(cy)\text{-}OH_2]^{2+}$ type complexes, second aqua inclusion with a $[Ru^{IV}(=O)]^{2+}$ complex possibly generates a short lived non rate-limiting seven-coordinate Ru(IV/III) type intermediate. This structure then loses two electrons in two stages, each coupled with proton removal to realize a $[Ru^{III}\text{-}(OOH)]^{2+}$ complex, followed by $[Ru^{IV}\text{-}(OO)]^{2+}$ formation. Finally, the complex $[Ru^{IV}\text{-}(OO)]^{2+}$ releases the molecular oxygen on the inclusion of a water molecule. The above observations match the modified S-cycle for the natural Mn_4O_4Ca cluster [14]. Thus, a pH dependent four-electron cycle that is coupled with proton transfer enables to construct a mono metal water oxidation system (Scheme 3.1).

3.3. CONCLUSIONS

In conclusion, a group of mono site ruthenium derived molecular water splitting catalysts is presented here that devise a four step proton coupled electron transfer cycle for dioxygen formation in homogeneous conditions. The electrochemical data

for the complexes $[(cy)Ru^{II}(N\text{-}N)\text{-}OH_2]^{2+}$ are translated into the free energy difference, while going from HOO* to HO* intermediate, and show the values of 3.1, 3.13 and 3.08 eV for $[(cy)Ru^{II}(bpy)OH_2]^{2+}$, $[(cy)Ru^{II}(phen)OH_2]^{2+}$ and $[(cy)Ru^{II}(bpm)OH_2]^{2+}$ complexes, respectively. It is expected that the results presented here will contribute a novel mechanistic reaction process and knowledge for designing future water splitting systems for clean fuel generation. Further work on the development of complexes with other alkyl substituted benzene such as hexamethyl benzene or durene, and pentamethylcyclopentadiene with dintirogen ligands, carboxylic acid derivatives of pyridine (COOH-py) and pyrazine (COOH-pz), and with N-Heterocyclic carbenes (NHC), is in progress.

3.4. MATERIALS AND METHODS

All syntheses of ligands and complexes were performed in oxygen free environment, in an argon or nitrogen atmosphere. $RuCl_3.nH_2O$, [Ru(*p*-cymene) $Cl_2]_2$ dimer, 2,2′-bipyridine (bpy), 1,10-phenanthroline (phen), 2,2′-bipyrimidine (bpm), 4,4′-dimethyl-2,2′-bipyridine (dmbpy) and cerium ammonium nitrate were obtained from Sigma-Aldrich Co., and used as received. The organic solvents for the synthesis were degassed and made anhydrous according to the standard procedures [31,32]. The synthesis of the $[RuCl_2(p\text{-cymene})]_2$ dimer and 4,4′-dinitro-2,2′-bipyridine (dnbpy) is described in the literature [33,34]. ^{1}H-NMR spectra were obtained with a Bruker WM-300 spectrometer. UV-vis spectra were recorded using Varian DMS 200 spectrophotometers, using Teflon-stoppered quartz cells with a path length of 1 cm.

Electrochemical investigations and cyclic voltammetry were performed with an Autolab PG-stat10 potentiostat controlled by GPES-4 software. A three electrode configuration pyrex glass cell was employed for electrochemical studies. The cell and glassware were decontaminated by boiling in a 1:2 mixture of concentrated nitric acid and sulfuric acid. The glass apparatus was then washed and boiled in ultra-pure water and dried in an oven. The cell was boiled 3 times in ultra-pure

water followed by thorough washing before each experiment. Solutions were prepared in ultra-pure water (Millipore MilliQ®) and electrochemical measurements were performed in deoxygenated aqueous solutions at room temperature.

The working electrode (WE) in the CV experiments was a freshly polished glassy carbon (GC) disk of 5.0 mm diameter, embedded in a PTFE shroud. A mirror finishing was achieved by polishing the GC disk mechanically with an aqueous slurry of 0.3, 0.1 and 0.05 μm alumina (Buehler Limited) successively, on a microcloth polishing fabric. After polishing, the GC disk was ultrasonically cleaned in Milli-Q (Millipore) water for 15 minutes after each polishing step and rinsed thoroughly with pure water. Platinum wire (thickness l=1 mm), shaped into a spiral, was used as a counter electrode (CE). The spiral platinum counter electrode was flame annealed and washed with pure water before placing it into the cell.

A mercury–mercury sulfate electrode (MMSE: $Hg/Hg_2SO_4/K_2SO_4$) was used as a reference electrode (RE) for the measurements in aqueous solution ($pH \leq 6$) and a silver–silver chloride electrode (SSCE: Ag/AgCl/KCl) was applied for the investigations in the neutral and higher pH aqueous solutions. All potentials are referred to the normal hydrogen electrode (NHE). The catalytic oxygen evolution was measured *in situ* in an air tight pyrex glass cell using a calibrated oxygen electrode connected with a digital O_2 meter (YSI, Inc., Model 550A) [7].

Synthesis

3.4.1. Chloro Complex [(cy)Ru^{II}(bpy)Cl]Cl (**Ru-**bpy)

2,2′-bipyridine (bpy: 0.156 g, 1.0 mmol) in MeOH (15 mL) was added to a stirred mixture of $[RuCl_2(p\text{-cymene})]_2$ dimer (0.362 g, 0.5 mmol) in ab. MeOH (20 mL). The mixture was further stirred for 1.5 hours at 40-45 °C. The solution was filtered with a sintered funnel of fine porosity and the solvent was evaporated under vacuum. The solid orange-yellow complex [(cy)Ru^{II}(bpy)Cl]Cl thus obtained was

re-precipitated from acetone or MeOH by addition of ether/hexane. Yield 0.33 g, 71 %. ^{1}H NMR (CD_3OD, 295 K, δ ppm, *J* Hz): 9.49 (d, 2H, $H^{6,6'}{}_{bpy}$, *J* 5.47); 8.51 (d, 2H, $H^{3,3'}{}_{bpy}$, *J* 7.97); 8.23 (t, 2H, $H^{4,4'}{}_{bpy}$, *J* 7.86); 7.76 (t, 2H, $H^{5,5'}{}_{bpy}$, *J* 6.65); 6.13 (d, 2H, $Ar_{p\text{-cy}}$, *J* 6.33); 5.87 (d, 2H, $Ar_{p\text{-cy}}$, *J* 6.33); 2.63 (sep, 1H, -C$\underline{H}(CH_3)_{2\ p\text{-cy}}$); 2.27 (s, 3H, $CH_{3\ p\text{-cy}}$); 1.17 (d, 6H, -CH(C$\underline{H}_3)_{2\ p\text{-cy}}$, *J* 6.91), Analysis found: C, 49.17%; H, 5.30%; N, 5.60%. Calculated: C, 50.0%; H, 5.04%; N, 5.83% for $C_{20}H_{22}N_2Ru_1Cl_2.H_2O$ complex.

3.4.2. Chloro Complex [(cy)Ru^{II}(dmbpy)Cl]Cl (**Ru-**dmbpy)

The orange-yellow chloro complex [(cy)Ru^{II}(dmbpy)Cl]Cl was prepared in a similar manner as described above (section 3.4.1) using 4,4′-dimethyl-2,2′-bipyridine (dmbpy: 0.184 g, 1.0 mmol) instead of 2,2′-bipyridine. Yield 0.37 g, 76 %. ^{1}H NMR (CD_3OD, 295 K, δ ppm, *J* Hz): 9.26 (d, 2H, $H^{6,6'}{}_{dMebpy}$, *J* 5.85); 8.37 (s, 2H, $H^{3,3'}{}_{dMebpy}$); 7.58 (d, 2H, $H^{5,5'}{}_{dMebpy}$, *J* 5.85); 2.62 (s, 6H, 4,4′-$(CH_3)_{2\ dMebpy}$); 6.06 (d, 2H, $Ar_{p\text{-cy}}$, *J* 6.33); 5.80 (d, 2H, $Ar_{p\text{-cy}}$, *J* 6.33); 2.60 (sep, 1H, -C$\underline{H}(CH_3)_{2\ p\text{-cy}}$); 2.26 (s, 3H, $CH_{3\ p\text{-cy}}$); 1.03 (d, 6H, -CH(C$\underline{H}_3)_{2\ p\text{-cy}}$, *J* 6.91), Analysis found: C, 51.20%; H, 5.96%; N, 5.53%. Calculated: C, 51.97%; H, 5.55%; N, 5.51% for $C_{22}H_{26}N_2Ru_1Cl_2.H_2O$ complex.

3.4.3. Chloro Complex [(cy)Ru^{II}(dnbpy)Cl]Cl (**Ru-**dnbpy)

The orange-red chloro complex [(cy)Ru^{II}(dnbpy)Cl]Cl was prepared in a similar manner as described above (section 3.4.1) using 4,4′-dinitro-2,2′-bipyridine (dnbpy: 0.246 g, 1.0 mmol) instead of 2,2′-bipyridine. Yield 0.43 g, 78 %. ^{1}H NMR (CD_3OD, 295 K, δ ppm, *J* Hz): 9.88 (d, 2H, $H^{6,6'}{}_{dnbpy}$, *J* 6.81); 9.51 (s, 2H, $H^{3,3'}{}_{dnbpy}$); 8.53 (dd, 2H, $H^{5,5'}{}_{dnbpy}$, *J* 2.28, *J* 6.25); 6.28 (d, 2H, $Ar_{p\text{-cy}}$, *J* 6.37); 6.05 (d, 2H, $Ar_{p\text{-cy}}$, *J* 6.37); 2.75 (sep, 1H, -C$\underline{H}(CH_3)_{2\ p\text{-cy}}$); 2.28 (s, 3H, $CH_{3\ p\text{-cy}}$); 1.11 (d, 6H, -CH(C$\underline{H}_3)_{2\ p\text{-cy}}$, *J* 6.91), Analysis found: C, 41.43%; H, 4.13%; N, 9.50%. Calculated: C, 42.11%; H, 3.89%; N, 9.82% for $C_{20}H_{20}N_4O_4Ru_1Cl_2.H_2O$ complex.

3.4.4. Chloro Complex [(cy)Ru^{II}(phen)Cl]Cl (**Ru-**phen)

The orange-yellow chloro complex [(cy)Ru^{II}(phen)Cl]Cl was prepared in a similar manner as described above (section 3.4.1) using 1,10-phenanthroline (phen: 0.18 g, 1.0 mmol) instead of 2,2′-bipyridine. Yield 0.34 g, 70 %. ^{1}H NMR (CD_3OD, 295 K, δppm, *J* Hz): 9.84 (dd, 2H, $H^{2,9}{}_{phen}$, *J* 1.14, *J* 5.27); 8.83 (dd, 2H, $H^{4,7}{}_{phen}$, *J* 1.14, *J* 8.25); 8.2 (s, 2H, $H^{5,6}{}_{phen}$); 8.11 (dd, 2H, $H^{3,8}{}_{phen}$, *J* 5.31, *J* 8.38); 6.24 (d, 2H, $Ar_{p\text{-cy}}$, *J* 6.35); 6.0 (d, 2H, $Ar_{p\text{-cy}}$, *J* 6.35); 2.66 (sep, 1H, -C$\underline{H}(CH_3)_{2\ p\text{-cy}}$); 2.26 (s, 3H, $CH_{3\ p\text{-cy}}$); 0.98 (d, 6H, -CH(C$\underline{H}_3)_{2\ p\text{-cy}}$, *J* 6.91), Analysis found: C, 50.32%; H, 5.21%; N, 5.31%. Calculated: C, 50.58%; H, 5.02%; N, 5.36% for $C_{22}H_{22}N_2Ru_1Cl_2.2H_2O$ complex.

3.4.5. Chloro Complex [(cy)Ru^{II}(bpm)Cl]Cl (**Ru-**bpm)

The orange-brown chloro complex [(cy)Ru^{II}(bpm)Cl]Cl was prepared in a similar manner as described above (section 3.4.1) using 2,2′-bipyrimidine (bpm: 0.158 g, 1.0 mmol) instead of 2,2′-bipyridine. Yield 0.31 g, 67 %. ^{1}H NMR (CD_3OD, 295 K, δppm, *J* Hz): 9.8 (dd, 2H, $H^{6,6'}{}_{bpm}$, *J* 1.96, *J* 5.76); 9.28 (dd, 2H, $H^{4,4'}{}_{bpm}$, *J* 1.96, *J* 4.77); 7.96 (t, 2H, $H^{5,5'}{}_{bpm}$, *J* 5.26); 6.22 (d, 2H, $Ar_{p\text{-cy}}$, *J* 6.43); 6.01 (d, 2H, $Ar_{p\text{-cy}}$, *J* 6.43); 2.79 (sep, 1H, -C$\underline{H}(CH_3)_{2\ p\text{-cy}}$); 2.25 (s, 3H, $CH_{3\ p\text{-cy}}$); 1.17 (d, 6H, -CH(C$\underline{H}_3)_{2\ p\text{-cy}}$, *J* 6.91), Analysis found: C, 43.61%; H, 4.89%; N, 11.40%. Calculated: C, 43.97%; H, 4.71%; N, 11.39% for $C_{18}H_{20}N_4Ru_1Cl_2.1.5H_2O$ complex.

3.4.6. General Synthesis of the Aqua Complexes: [(cy)Ru^{II}(L)-OH_2]$^{2+}$ (Cat.**Ru**-L)

The chloro complexes [(cy)Ru^{II}(L)Cl]$^+$ (**Ru-**L) were converted into the aqua (OH_2) catalysts [(cy)Ru^{II}(L)-OH_2]$^{2+}$ (Cat.**Ru-**L) by stirring with aqueous solution containing 2.1 eq. of $AgNO_3$ or silver hexafluorophosphate in methanol (1:1, H_2O/MeOH) for 30 minutes. The white precipitates were filtered off and the solvent mixture was evaporated under vacuum. The yellow solid aqua complexes

thus obtained were recrystallized from acetone or MeOH by addition of ether/hexane.

3.4.7. Direct Synthesis of the Aqua Complexes: $[(cy)Ru^{II}(L)\text{-}OH_2]^{2+}$ (Cat.**Ru**–L)

Dinitrogen ligands (L) (1.0 mmol) were dissolved in 15 mL MeOH/H_2O and added to aqueous tri-aqua $[(Ru)(cy)\text{-}(OH_2)_3]^{2+}$ (1.0 mmol). The mixture was stirred for 5 hours at 65 °C giving a yellow solution. The solvent was evaporated to yield a yellow solid $[(cy)Ru^{II}(L)\text{-}OH_2]^{2+}$ (Cat.**Ru**–L) that was further dried in vacuo. The solid pale yellow complex thus obtained was recrystallized from MeOH by addition of ether/hexane.

The rapid *in situ* aqua (OH_2) exchange in the complex $[(cy)Ru^{II}(L)Cl]^{+}$ also occurred when the complex is mixed with the 0.1 M aqueous acidic solution for a few minutes. The aqua exchange was monitored by following the colour change of the solution from orange to yellow visually or by UV-Vis spectral investigation (Fig. 3.2).

Scheme 3.2. Schematic representation of the synthesis route for the *p*-cymene ruthenium derived bipyridine, 4,4′-disubstituted-2,2′-bipyridine, phenanthroline and 2,2′-bipyrimidine mono metal complexes.

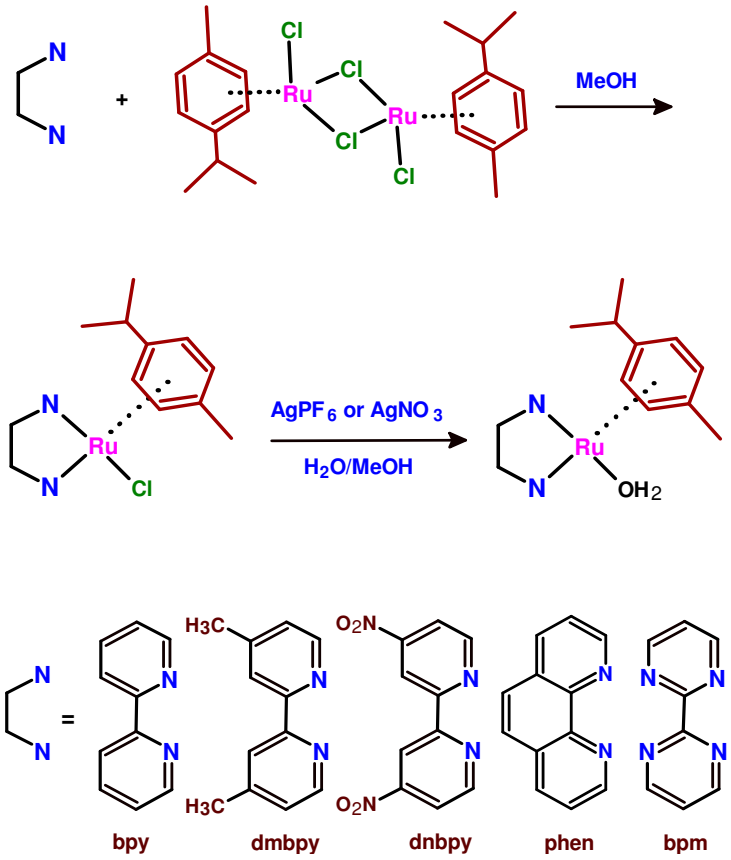

REFERENCES

01- I. C. Man, H.-Y. Su, F. Calle-Vallejo, H. A. Hansen, J. I. Martínez, N. G. Inoglu, J. Kitchin, T. F. Jaramillo, J. K. Nørskov and J. Rossmeisl, *ChemCatChem* **2011**, *3*, 1159–1165.

02- N. S. Lewis, *Nature* **2001,** *414*, 589–590.

03- T. J. Meyer, *Nature* **2008**, *451*, 778–779.

04- T. Wada, K. Tsuge and K. Tanaka, *Angew. Chem. Int. Ed. Engl.* **2000**, *39*, 1479–1482.

05- C. Sens, I. Romero, M. Rodríguez, A. Llobet, T. Parella and J. Benet-Buchholz, *J. Am. Chem. Soc.* **2004**, *126*, 7798–7799.

06- N. D. McDaniel, F. J. Coughlin, L. L. Tinker and S. Bernhard, *J. Am. Chem. Soc.* **2008**, *130*, 210–217.

07- Chen, Z. Concepcion, J. J. Jurss, J. W. and Meyer, T. J. *J. Am. Chem. Soc.* **2009**, *131*, 15580–15581.

08- J. D. Blakemore, N. D. Schley, D. Balcells, J. F. Hull, G. W. Olack, C. D. Incarvito, O. Eisenstein, G. W. Brudvig and R. H. Crabtree, *J. Am. Chem. Soc.* **2010**, *132*, 16017–16029.

09- L. Tong, L. Duan, Y. Xu, T. Privalov and L. Sun, *Angew. Chem. Int. Ed.* **2011**, *50*, 445 –449.

10- K. N. Ferreira, T. M. Iverson, K. Maghlaoui, J. Barber and S. Iwata, *Science* **2004**, *303*, 1831–1838.

11- Y. Umena, K. Kawakami, J. R. Shen and N. Kamiya, *Nature* **2011**, *473*, 55–60.

12- M. H. V. Huynh and T. J. Meyer, *Chem. Rev.* **2007**, *107*, 5004–5064.

13- R. Zong and R. P. Thummel, *J. Am. Chem. Soc.* **2005**, *127*, 12802–12803.

14- H. Dau, C. Limberg, T. Reier, M. Risch, S. Roggan and P. Strasser, *ChemCatChem* **2010**, *2*, 724–761.

15- J. J. Concepcion, J. W. Jurss, J. L. Templeton and T. J. Meyer, *J. Am. Chem. Soc.* **2008**, *130,* 16462–16463.

16- D. J. Wasylenko, C. Ganesamoorthy, M. A. Henderson, B. D. Koivisto, H. D. Osthoff and C. P. Berlinguette, *J. Am. Chem. Soc.* **2010**, *132*, 16094–16106.

17- J. Rossmeisl, K. Dimitrievski, P. Siegbahn and J. K. Nørskov, *J. Phys. Chem. C* **2007**, *111*, 18821–18823.

18- M. T. M. Koper, *J. Electroanal. Chem.* **2011**, *660*, 254–260.

19- (a) J. J. Concepcion, M.-K. Tsai, J. T. Muckerman and T. J. Meyer, *J. Am. Chem. Soc.* **2010**, *132*, 1545–1557; (b) L. Tong, L. Duan, Y. Xu, T. Privalov and L. Sun, *Angew. Chem. Int. Ed.* **2011**, *50*, 445–449.

20- F. Liu, T. Cardolaccia, B. J. Hornstein, J. R. Schoonover and T. J. Meyer, *J. Am. Chem. Soc.* **2007**, *129*, 2446–2447.

21- K. S. Joya and H. J. M. de Groot, *Netherlands Patent Application* no. 2005512, Oct., **2010**.

22- S. B. Wendicke, E. Burri, R. Scopelliti and K. Severin, *Organometallics* **2003**, *22*, 1894–1897.

23- Md. K. Nazeeruddin, S. M. Zakeeruddin, J.-J. Lagref, P. Liska, P. Comte, C. Barolo, G. Viscardi, K. Schenk and M. Graetzel, *Coord. Chem. Rev.* **2004**, *248*, 1317–1328.

24- P. Govindaswamy, J. Canivet, B. Therrien, G. Süss-Fink, P. Štěpnička and J. Ludvík, *J. Organomet. Chem.* **2007**, *692*, 3664–3675.

25- B. Therrien, G Süss-Fink, P. Govindaswamy and C. Saïd-Mohamed, *Polyhedron* **2007**, *26*, 4065–4072

S. B. Wendicke, E. Burri, R. Scopelliti and K. Severin, *Organometallics* **2003**, *22*, 1894–1897.

26- R. S. Nicholson and I. Shain, *Ana. Chem.* **1964**, *36*, 706–723.

27- The electrochemical experiments for oxygen onset were conducted on ITO electrodes modified with the catalyst. The oxygen generation overpotential was about ~0.62 V (vs. NHE).

28- H. J. M. de Groot, S. O. Smith, J. Courtin, E. van den Berg, C. Winkel, J. Lugtenburg, R. G. Griffin and J. Herzfeld, *Biochemistry* **1990**, *29*, 6873–6883.

29- M. E. Navarro Clemente, J. P. Saavedra, M. C. Vásquez, M. A. Paz-Sandoval, A. M. Arif and R. D. Ernst, *Organometallics* **2002**, *21*, 592–605.

30- J. Shen, E. D. Stevens and S. P. Nolan, *Organometallics* **1998**, *17*, 3875–3882.

31- D. D. Perrin and W. L. F. Armarego, Purification of Laboratory Chemicals; Pergamon Press: New York, **1988**, and references cited therein.

32- B. S. Furniss, A. J. Hannaford, P. W. G. Smith and A. R. Tatchell, Vogel's Textbook of Practical Organic Chemistry, 5th ed.; Pearson: Harlow, **1989** and references cited therein.

33- M. A. Bennett and A. K. Smith, *J. Chem. Soc. Dalton Trans*. **1947**, 233–241.

34- G. Maerker and F.Case, *J. Am. Chem. Soc*. **1958**, *80*, 2745-2748.

Appendix A3

[(cy)Ru^{II}(bpy)-Cl]Cl

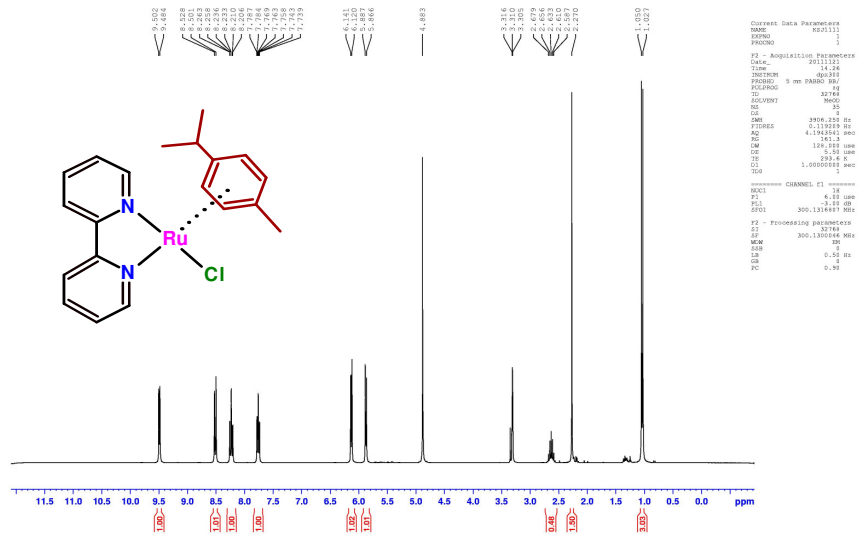

[(cy)Ru^{II}(dmbpy)-Cl]Cl

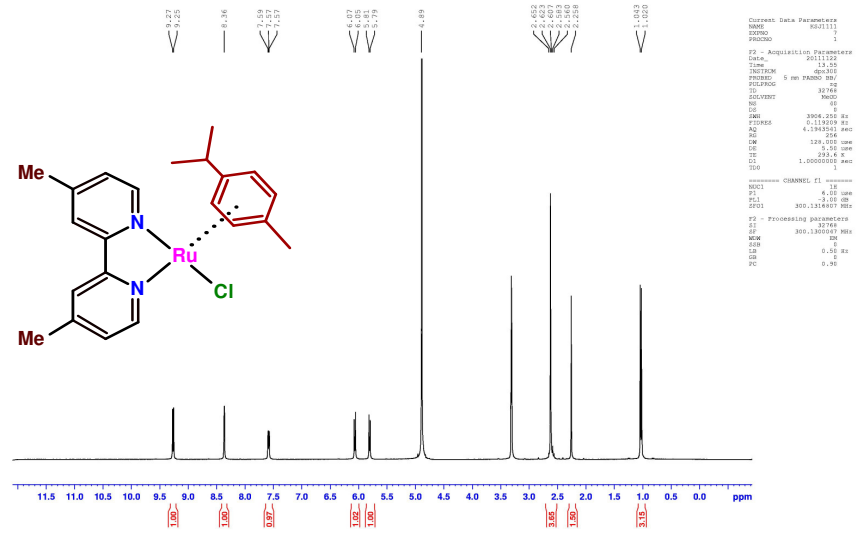

[(cy)Ru^{II}(dnbpy)-Cl]Cl

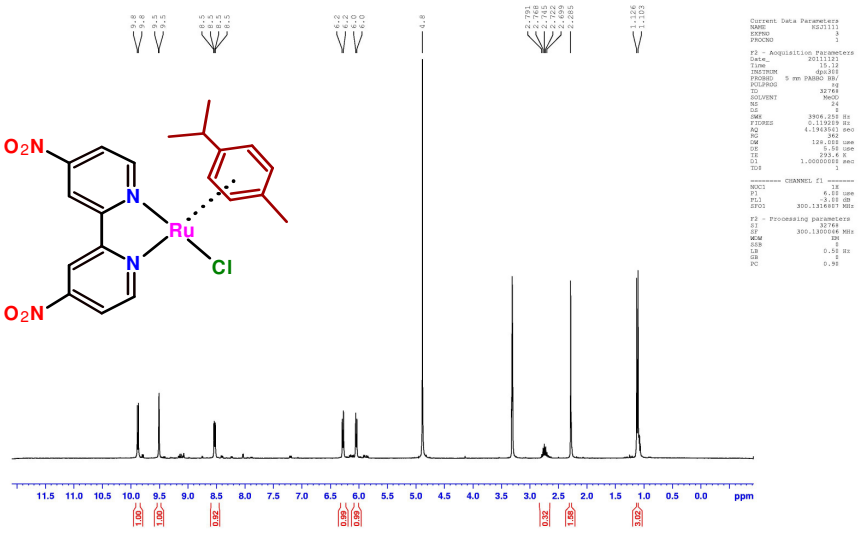

[(cy)Ru^{II}(phen)-Cl]Cl

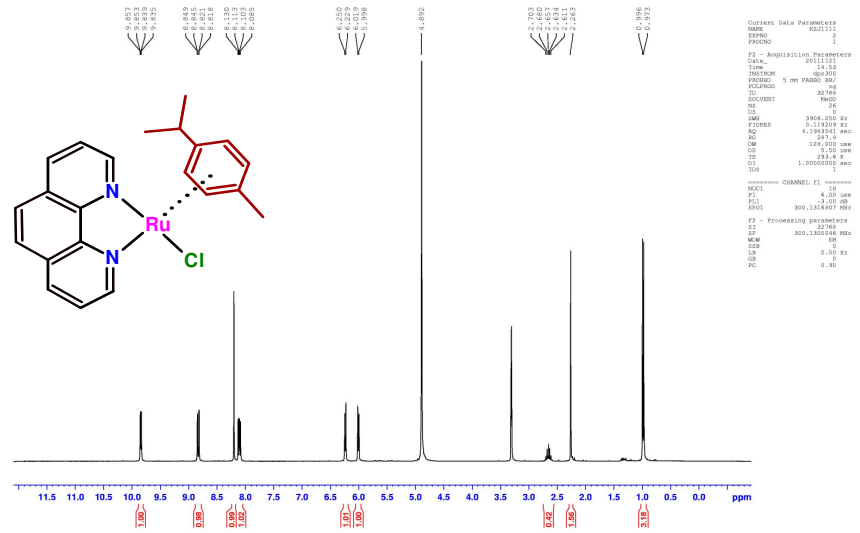

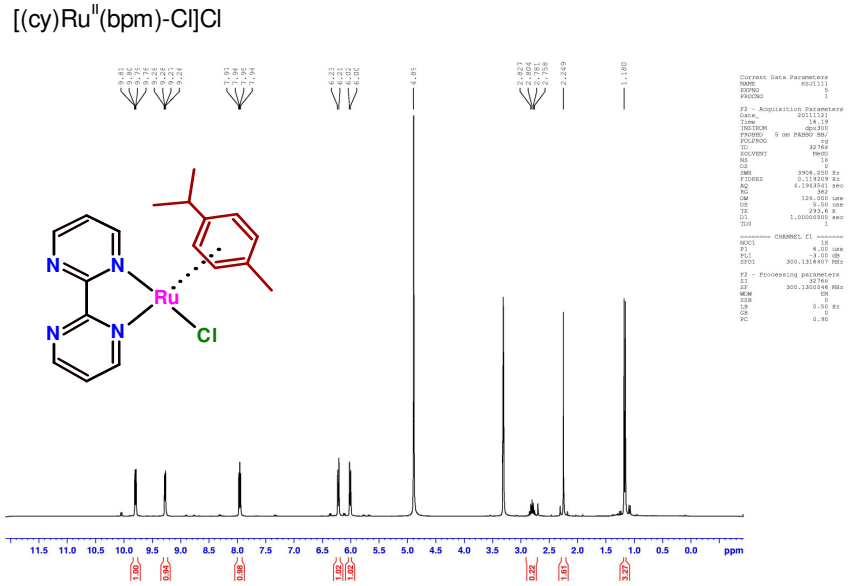

Figure A3.1. Proton NMR spectra of the complexes **Ru**-bpy, **Ru**-bdmpy, **Ru**-dnbpy, **Ru**-phen and **Ru**-bpm.

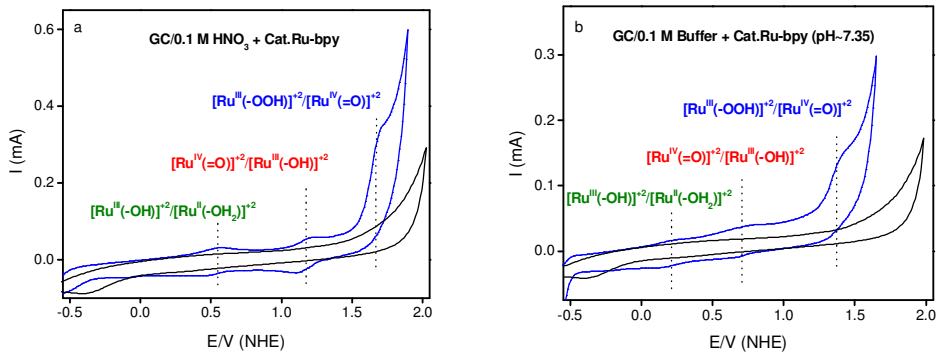

Figure A3.2. Cyclic voltammograms of Cat.**Ru**–bpy (2.5 mM) at glassy carbon disk working electrode in 0.1 M (**a**) HNO_3 and (b) buffer (pH~7.35) solutions showing $[Ru^{III}\text{-}(OH)]^{2+}/[Ru^{II}\text{-}(OH_2)]^{2+}$ and $[Ru^{IV}(=O)]^{2+}/[Ru^{III}\text{-}(OH)]^{2+}$ reversible couples. (Scan rate was 100 mV/sec; glassy carbon disk diameter d=5 mm).

Figure A3.3.
Spectral investigation ascribed to the consecutive oxidation of $[(cy)Ru(bpm)-(OH_2)]^{2+}$ catalyst (green line) into $[Ru^{III}-(OH)]^{2+}$, (red line) $[Ru^{IV}(=O)]^{2+}$, (blue line) $[Ru^{III}-(OOH)]^{2+}$ and (purple line) $[Ru^{IV}-(OO)]^{2+}$ in 0.1 M aqueous HNO_3 using quantitative Ce(IV) solution.

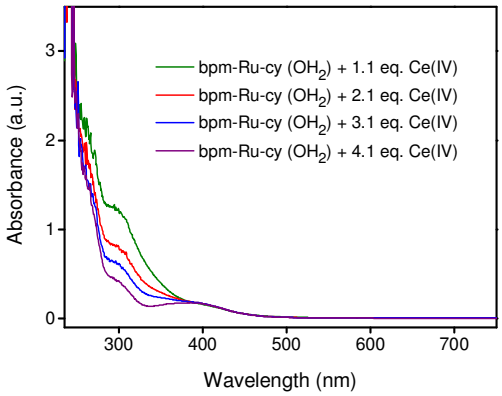

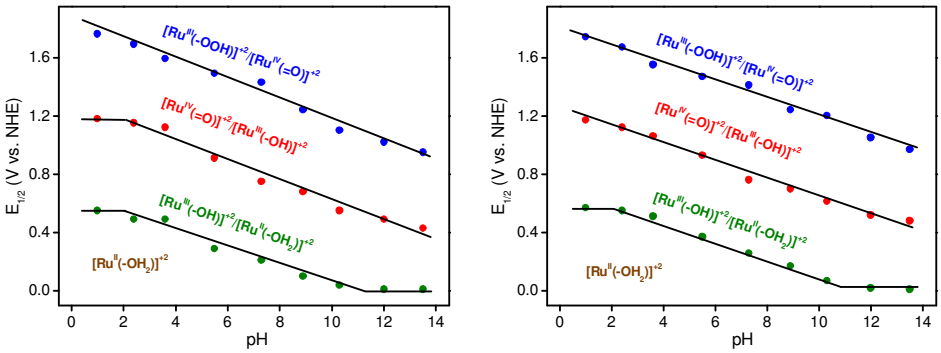

Figure A3.4. (**Left**) Potential vs pH plot (Pourbaix diagram) for $[(phen)Ru^{II}(cy)OH_2]^{2+}$ and (**right**) $[(bpm)Ru^{II}(cy)OH_2]^{2+}$ showing $[Ru^{III}(OH)]^{2+}/[Ru^{II}(OH_2)]^{2+}$, $[Ru^{IV}(=O)]^{2+}/[Ru^{III}(OH)]^{2+}$ and $[Ru^{III}(OOH)]^{2+}/[Ru^{IV}(=O)]^{2+}$ transitions generated at glassy carbon disk (diameter d=5mm) working electrode in 0.1 M aqueous solutions.

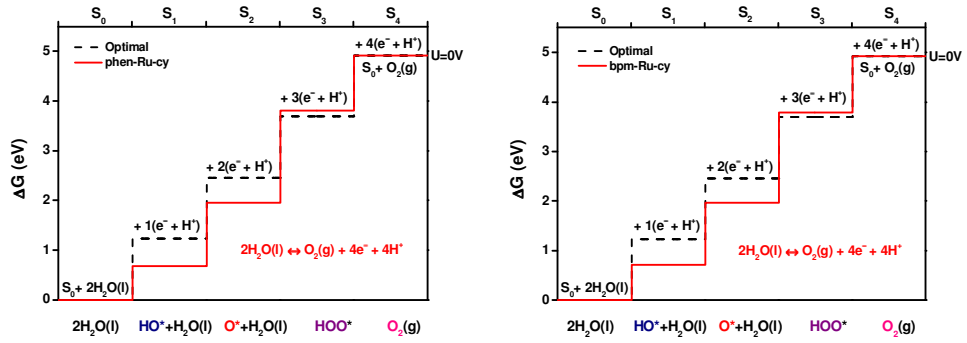

Figure A3.5. Relative Gibbs free energies (ΔG) of reactive species and intermediates (horizontal lines) during water splitting and oxygen generation for (**Left**) $[(phen)Ru^{II}(cy)OH_2]^{2+}$. (ΔG = 0.68, 1.28, 1.85 eV) and (**right**) $[(bpm)Ru^{II}(cy)OH_2]^{2+}$ (ΔG = 0.71, 1.26, 1.82 eV), compared with the free energy profiles for the reaction coordinate of an optimal catalyst with four steps each of 1.23 eV [13,16].

Table A3.1. Initial rates for oxygen generation catalyzed by $[(cy)Ru^{II}(N\text{-}N)\text{-}OH_2]^{2+}$ complexes in argon-purged 0.1 M HNO_3 aqueous solutions using 350 eq. of Ce(IV).

Catalyst	Formula	Initial rate ($t.o.hour^{-1}$)[a]	TON[b]
Cat.**Ru**–bpy	$(bpy)Ru^{II}(cy)\text{-}OH_2$	29.3	46.2
Cat.**Ru**–dmbpy	$(dmbpy)Ru^{II}(cy)\text{-}OH_2$	15	39.4
Cat.**Ru**–dnbpy	$(dnbpy)Ru^{II}(cy)\text{-}OH_2$	31.7	42.9
Cat.**Ru**–phen	$(phen)Ru^{II}(cy)\text{-}OH_2$	12	30.1
Cat.**Ru**–bpm	$(bpm)Ru^{II}(cy)\text{-}OH_2$	42	53

[a] Turnovers (t.o.) obtained in first hour of catalysis and [b] total turnover number obtained during 5 hours of catalysis operation.

Chapter 4

Surface Electrocatalytic Assembly for Water Oxidation at High Turnover and Rate

ABSTRACT

The development surface catalytic electrochemical assembly for water oxidation is important for application in electro- and photo-driven devices for fuel generation. This chapter describes the extension of the mono-site ruthenium derived molecular complexes in chapter 3 for use in an electrochemical system and discloses a highly competent immobilized mono-site ruthenium molecular catalytic assembly for water oxidation and oxygen evolution. This catalytic system mimics the photosystem-II (PS-II) in producing hundred thousands of rapid turnovers for dioxygen by four proton coupled electron transfer (PCET) steps. In neutral water, the catalyst generates >3 × 10^5 turnovers for dioxygen at a frequency of ~7 per second and more than 6 × 10^5 turnovers at ~5.33 sec^{-1} in aqueous acids were realized. The catalyst cycles through $Ru^{II/III/IV}$–$Ru^{III/IV/II}$ states while maintaining an overall charge +2. This leads to a water splitting device with the highest turnover numbers achieved till date for a molecular catalyst. A turnover rate up to 80 per second was achieved during full cell water electrolysis between 1.8–2.2 V (vs. NHE).

Based on: K.S. Joya and H.J.M. de Groot, **2011** (*submitted*)

4.1. INTRODUCTION

The quest for a greener future through clean and affordable energy, fuel and electricity, using renewable natural resources, has become one of the most urgent challenges, spurred by worries about global warming, climate change and fuel scarcity [1,2]. The production of hydrogen or low-carbon based fuels from catalytic water splitting using solar energy represents an attractive potential solution for environmentally clean energy carriers [3-5]. However, the design and implementation of a stable four-electron transfer catalytic system for efficient water oxidation operating at high catalytic turnover number (TON) and frequency (TOF), with low activation barrier, moderate overpotential and high current density is a challenging hurdle along the way [6-10]. Principles laid down in natural photosystem-II have manifested guidance for the synthetic design, where a consecutive proton coupled electron transfer regime enables the accumulation of four redox equivalents that circumvent high energy intermediates during the multi-electron water oxidation cycle [11,12].

In spite of the elucidation of the photosynthetic machinery, there is as yet no artificial equivalent, capable of constructing a four-step PCET pathway, separating electrons and protons from water to produce oxygen at a high rate for hundred thousands of cycles [13-18]. During last few years, a growing interest in light driven and electrocatalytic water splitting has triggered the scientific interest towards the construction of an efficient system with a robust oxygen evolving complex (OEC). In this pursuit, various molecular complexes [17-20] and inorganic oxide materials [21-23] have been scrutinized for effective water oxidation, but they were far behind in mimicking the TON and TOF performance of PS-II. Also the few electrochemical molecular catalysis systems that have been reported show a low rate and small current densities for oxygen evolution [24-26].

From a mechanistic standpoint, formation of molecular oxygen is realized by the extraction of four electrons and protons in four PCET steps from two water molecules at the anode [12]. The total free energy change between H_2O and the

reaction products, O_2 and H_2, is 4.92 eV (see chapter 1 for details). An ideal water oxidation catalyst operates at an equilibrium potential of 1.23 eV for each PCET step and photosynthesis is thought to work very close to this optimum [27,28]. In mononuclear artificial systems, the maximum oxygen evolution activity is considered to be limited due to a minimum overpotential of ~0.4 V when proceeding through an HOO* intermediate, and there is a constant difference of 3.2±0.1 eV in the affinity between the HOO* and the HO* intermediates [11,27]. However, recently reported mono-site ruthenium catalysts are unable to construct a four step PCET mechanism, and the HOO* intermediate is formed at high potential from a $[Ru^{V}=O]^{3+}$ species which is generated by an electron transfer step in a non-PCET rate limiting step [18,29].

In this chapter, the synthesis and analysis of a highly efficient and apparently robust immobilized electro-assisted catalytic water splitting system is described that generates hundred thousands turnover at a rapid rate, both in neutral solution and aqueous acids (Fig. 4.1).

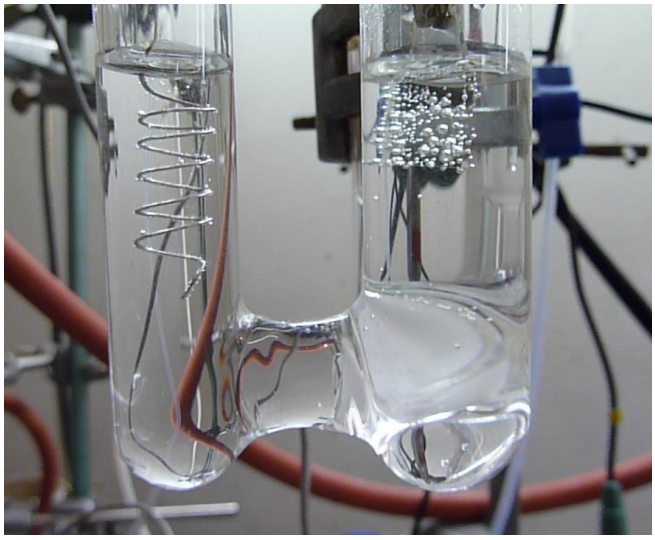

Figure 4.1. Experimental demonstration of oxygen generation (bubbles) by Cat.**Ru**–PO_3H_2 or Cat.**Ru**–COOH catalyst anchored on ITO electrode surface via linker molecules (L = COOH or PO_3H_2) to drive electro-assisted water oxidation.

The catalysts are easy accessible mononuclear ruthenium complexes with alkyl substituted benzene or cyclopentadiene and a heterocyclic 2,2′-bipyridine (bpy) ligand [30]. The complexes can be immobilized on conducting oxide surfaces via anchoring groups like COOH or PO_3H_2 and electrochemical analyses provide converging evidence that the catalysts operate by a four-step PCET mechanism for water oxidation at a moderate overpotential. The onset of oxygen evolution in aqueous acid (pH=1) is just above 1.83 V (vs. NHE) and at *ca*. 1.45 V (vs. NHE) in neutral solution. Catalytic induction of the complex by aqua exchange produces an electronic bias that brings the catalyst redox potential into the regime for PCET water oxidation while reducing the proton affinity at the same time. A mechanism is proposed where the catalyst cycles through $Ru^{II/III/IV}$–$Ru^{III/IV/II}$ states while maintaining an overall divalent positively charged complex during the water oxidation pathway.

4.2. RESULTS AND DISCUSSION

4.2.1. Synthesis and Characterization

The *p*-cymene-Ru derived 4,4′-dicarboxylic (H_2dcabpy) or 4,4′-diphosphonic acid (H_4dphbpy) modified 2,2′-bipyridine complexes $[(H_2dcabpy)Ru^{II}(cy)Cl]^+$ (**Ru**–COOH) and $[(H_4dphbpy)Ru^{II}(cy)Cl]^+$ (**Ru**–PO_3H_2), and their aqua version catalysts $[(H_2dcabpy)Ru^{II}(cy)\text{-}OH_2]^{2+}$ (Cat.**Ru**–COOH) and $[(H_4dphbpy)Ru^{II}(cy)\text{-}OH_2]^{2+}$ (Cat.**Ru**–PO_3H_2), were obtained by procedures described in Materials and Methods, and charaterized by proton NMR spectra and elemental analysis (see subsection 4.4.1). The X-ray structure of the related complexes reveals a trans configuration of the dinitrogen ligand with respect to the aromatic moeity [31,32]. The aqua versions Cat.**Ru**–PO_3H_2 and Cat.**Ru**–COOH are readily obtained by stirring with the stoichiometric aliquots of aqueous $AgNO_3$ or silver hexafluorophosphate in methanol water mixture. Similar to the complexes described in chapter 3, the *in situ* aqua exchange for $[(H_2dcabpy)Ru^{II}(cy)Cl]^+$ complex in the presence of water is also followed by UV-vis studies indicating

spectral changes for colour change from orange-yellow to bright-yellow, corresponding with an absorption band shift from 412 nm to 399 nm (Fig. A4.2). Above pH=8, the complex starts to turn brown ascribed to the deprotonation of the OH_2 moiety and the solution darkens upon further increase of the pH.

4.2.2. Electrochemistry and Oxygen Evolution

The CV of the linker modified $[(cy)Ru^{II}(L_2\text{-bpy})OH_2]^{2+}$ catalyst shows clean polarization waves for the $[Ru^{III}\text{-}(OH)]^{2+}/[Ru^{II}\text{-}(OH_2)]^{2+}$ and $[Ru^{IV}(=O)]^{2+}/[Ru^{III}\text{-}(OH)]^{2+}$ redox pairs in aqueous solution (Fig. 4.2). In aqueous acid, the current waves for the first two oxidations appear at $E_{1/2}$ *ca.* 0.60 V and 1.18 V (vs. NHE) respectively. For E >1.5 V (vs. NHE) the current rises due to the formation of the $[Ru^{III}\text{-}(OOH)]^{2+}$ species from $[Ru^{IV}(=O)]^{2+}$ on second aqua ligation and following $[Ru^{IV}\text{-}(OO)]^{2+}/[Ru^{III}\text{-}(OOH)]^{2+}$ with subsequent oxygen release at E >1.83 V (vs. NHE), observed as bubbles on the working electrode during forward scans. In neutral solution, $[Ru^{III}\text{-}(OH)]^{2+}/[Ru^{II}\text{-}(OH_2)]^{2+}$ and $[Ru^{IV}(=O)]^{2+}/[Ru^{III}\text{-}(OH)]^{2+}$ pairs appear at $E_{1/2}$ ~ 0.22 V and $E_{1/2}$ ~ 0.77 V (vs. NHE), respectively, with weaker signals resembling Cat.**Ru**–bpy as described in section 3.2.2 [33,34]. The electrochemical findings in aqueous acid and neutral solution validate the Nernst behaviour for $[Ru^{III}\text{-}(OH)]^{2+}/[Ru^{II}\text{-}(OH_2)]^{2+}$ and $[Ru^{IV}(=O)]^{2+}/[Ru^{III}\text{-}(OH)]^{2+}$ transitions by two consecutive PCET steps [29]. The $[Ru^{III}\text{-}(OOH)]^{2+}/[Ru^{IV}(=O)]^{2+}$ transition in the neutral phase occurs at $E_{1/2}$ *ca.* 1.42 V (vs. NHE) while the reverse scan reveals the reduction wave for $[Ru^{IV}(=O)]^{2+}/[Ru^{III}\text{-}(OOH)]^{2+}$ at *ca.* 1.36 V (vs. NHE). This confirms the Nernst behaviour for the $[Ru^{III}\text{-}(OOH)]^{2+}/[Ru^{IV}(=O)]^{2+}$ transition, which implies a third consecutive PCET step along the reaction coordinate describing the catalytic mechanism. Since the steps are very similar as for the homogeneous catalysts in chapter 3, there is very little effect of the linker on the catalytic function.

The stepwise oxidation of $[Ru^{II}\text{-}OH_2]^{2+}$ into $[Ru^{III}\text{-}(OH)]^{2+}$ and $[Ru^{IV}(=O)]^{2+}$ in acidic solution is also monitored spectro-electrochemically at 0.63 V and 1.22 V (vs. NHE) for a sample at higher concentration to make the optical absorption

detectable. The third oxidation step of the catalyst occurs *ca.* 1.75 V (vs. NHE) and is accompanied by a colour change (inset Fig. 4.2). Repeating the scans in neutral solution generates similar spectral shifts for consecutive oxidation at 0.27 V, 0.82 V and 1.43 V (vs. NHE) respectively. The absorption spectra for $[Ru^{III}\text{-}OH]^{2+}$ and $[Ru^{II}\text{-}OH_2]^{2}$ are entirely recovered during reduction from $[Ru^{IV}{=}O]^{2+}$ or $[Ru^{III}\text{-}OH]^{2+}$ for the reverse scan, at cathodic peak potentials of 1.05 V and 0.51 V, respectively. This points to sturdiness and reversible kinetics of the electrocatalytic system [9,25].

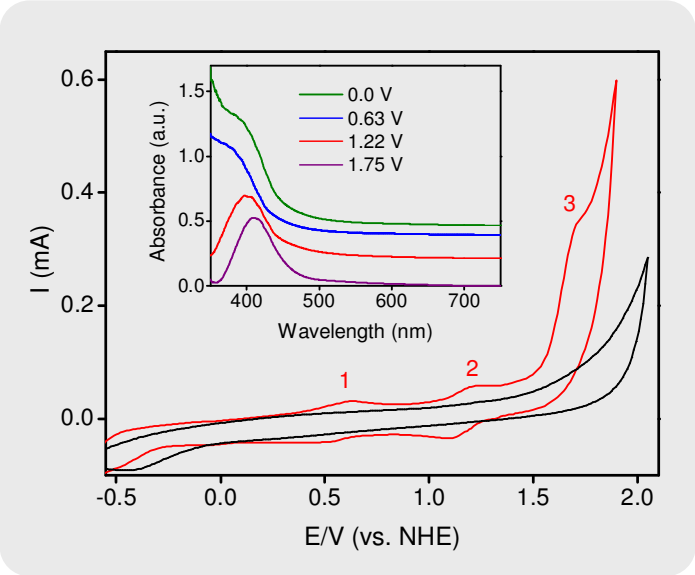

Figure 4.2. Cyclic voltammograms of $[(cy)Ru(dcabpy)\text{-}(OH_2)]^{2+}$ complex (2 mM) at a glassy carbon (GC) disk in 0.1 M HNO_3 solution showing oxidation waves for (1) $[Ru^{III}\text{-}(OH)]^{2+}/[Ru^{II}\text{-}(OH_2)]^{2+}$, (2) $[Ru^{IV}(=O)]^{2+}/[Ru^{III}\text{-}(OH)]^{2+}$ and (3) $[Ru^{III}\text{-}(OOH)]^{2+}/[Ru^{IV}(=O)]^{2+}$ (red line) and a blank CV trace for a glassy carbon (GC) disk measured under similar conditions (black line). (E/V vs. NHE, scan rate was 100 mV/sec, GC disk diameter d=5 mm). The inset shows spectro-electrochemical investigation of the Cat.**Ru**–COOH in 0.1 M HNO_3 solution. The UV-vis spectra were recorded at 0.0V and following electrolysis at 0.63 V (blue line); 1.22 V (red line) and 1.75 V (purple line). (The catalyst concentration was ~8.5 µM).

The onset of oxygen evolution for a Cat.**Ru**–COOH modified ITO electrode initiates just above 1.41 V (vs. NHE) in neutral phosphate buffer solution. On the other hand, the oxygen generation starts at *ca.* 1.87 V (vs. NHE) in 0.1 M aqueous

acid (Fig. 4.3). After the oxygen onset in neutral solution, the current density rises sharply and reaches >3 mA/cm^2 at just 1.55 V. ITO is considered a relatively inert electrode [8-10], and this observation provides strong evidence for an excellent and fast rate catalytic performance of the system for electrolysis of neutral water. Since the overpotential closely matches the behaviour of the catalyst measured on the glassy carbon electrode, it is unlikely that the complex decomposes on the surface. In addition, similar type of surface enhancement has been observed by Meyer's group for [(N-N)Ru^{II}(terpy)-(OH$_2$)]$^{n+}$ and [(N-N)Ru^{II}(Mebimpy)-(OH$_2$)]$^{n+}$ catalysts [25,26]. Further cycling of the potential for the surface anchored catalyst in neutral buffer solution causes the current density to attain a value >14 mA/cm^2 at *ca.* 1.95 V vs. NHE (Fig. 4.3). The current density increase is accompanied by a rapid rise of the oxygen generation at the Cat.**Ru**–COOH modified indium-doped tin oxide (ITO) electrode with simultaneous hydrogen evolution at the Pt counter electrode.

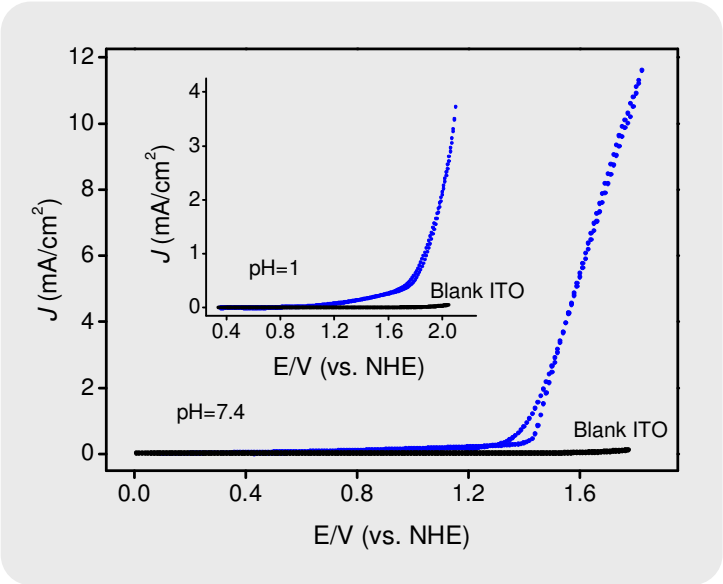

Figure 4.3. Cyclic voltammograms for a Cat.**Ru**–COOH modified ITO electrode (Cat/ITO) showing the oxygen onset current wave in 0.1 M aqueous phosphate buffer (pH=7.4) that was deoxygenated prior to performing the experiment. The inset represents the CV for the onset current wave in 0.1 M H_2SO_4 solution under similar conditions. (Scan rate was 50 mV/sec, ITO area A=1 cm^2, catalyst loading 1.51–1.65 × 10^{-10} mol/cm^2).

At higher potential (above 1.80 V vs. NHE) in neutral solution, the rapid increase of the current density with applied potential gradually levels off (Fig. 4.3 and Fig. A4.3). Meanwhile, an abundant stream of oxygen bubbles leaves from the ITO electrode surface. It is remarkable that the first conversion step, the oxidation of the $[Ru^{II}\text{-}(OH_2)]^{2+}$ into $[Ru^{III}\text{-}(OH)]^{2+}$ appears at a lower potential, at *ca.* ~0.60 V (vs. NHE) than for the recently reported $E_{1/2} > 0.90$ V (vs. NHE) for mono site ruthenium catalysts [18,34]. The oxygen evolution CV's at high current densities of 4 and 12 mA/cm^2 for the immobilized complexes on ITO in acidic and neutral pH solutions are remarkably reproducible, indicating good stability of the surface anchored catalyst under electrochemical conditions (Fig. 4.3). This is in line with the high TOF and TON for the electrocatalytic systems. The CV data for the electrodes in acidic solution and in neutral media provide converging evidence that the electrochemical redox behaviour of the $[(cy)Ru^{II}(dcabpy)OH_2]^{2+}$ catalyst comprises multiple pH dependent oxidations and exhibits also a shift in the oxygen onset potential while going from an acidic phase to a neutral solution (Fig. 4.3).

4.2.3. Pourbaix Diagram and Free Energy Profile

The Pourbaix diagram constructed for the various ruthenium transitions in the Cat.**Ru**–COOH is shown in Figure 4.4. A ~60 mV/pH shift of the equilibrium point for water oxidation is detected for positive potential scanning in aqueous solution over a wide pH range, from 2 to 12. This shows that the limiting step is a PCET process for water oxidation. The pH-dependence of the transition from the $[Ru^{IV}(=O)]^{2+}$ to the $[Ru^{III}\text{-}OOH)]^{2+}$ intermediate indicates the Nernst behaviour of the $[Ru^{III}\text{-}(OOH)]^{2+}/[Ru^{IV}(=O)]^{2+}$ couple that determines the overpotential of the system. The PCET formation of $[Ru^{III}\text{-}OOH)]^{2+}$ from $[Ru^{IV}(=O)]^{2+}$ was not yet observed for a mono site molecular water oxidation catalyst [18,25]. For instance, in recently reported mononuclear complexes the rate-limiting step is independent of pH and is thought to involve the formation of a high energy $[Ru^{V}=O]^{3+}$ intermediate via a non-PCET step by one electron oxidation of $[Ru^{IV}=O]^{2+}$ above 1.75 V (vs. NHE) prior to second OH_2 insertion [25,26]. In this scheme, a subsequent OH_2

attack is rate limiting for O-O bond formation and is followed by release of a proton [29].

In contrast, for catalyst Cat.**Ru**–COOH the oxygen generation occurs at less overpotential in neutral or higher pH aqueous solutions by following a ~60 mV/pH slope due to the PCET conversion of the ruthenium couple $[Ru^{III}\text{-}(OOH)]^{2+}/[Ru^{IV}{=}O]^{2+}$. In neutral solution, the water catalysis by the $[(cy)Ru^{II}(dcabpy)OH_2]^{2+}$ complex starts just above 1.41 V (vs. NHE) and the limiting step is the formation of the $[Ru^{III}\text{-}(OOH)]^{2+}$ species with a standard free energy difference of ΔG=1.83 eV (pH=0) and at an overpotential ΔV=0.60 V for the full electrolysis reaction. Since this overpotential is quite close to the minimum overpotential of 0.4 V, there is near-optimal positioning of $[Ru^{IV}(=O)]^{2+}$ intermediate with respect to the free energy levels of $Ru^{III}\text{-}(OH)]^{2+}$ and $[Ru^{III}\text{-}(OOH)]^{2+}$ complexes [27,28].

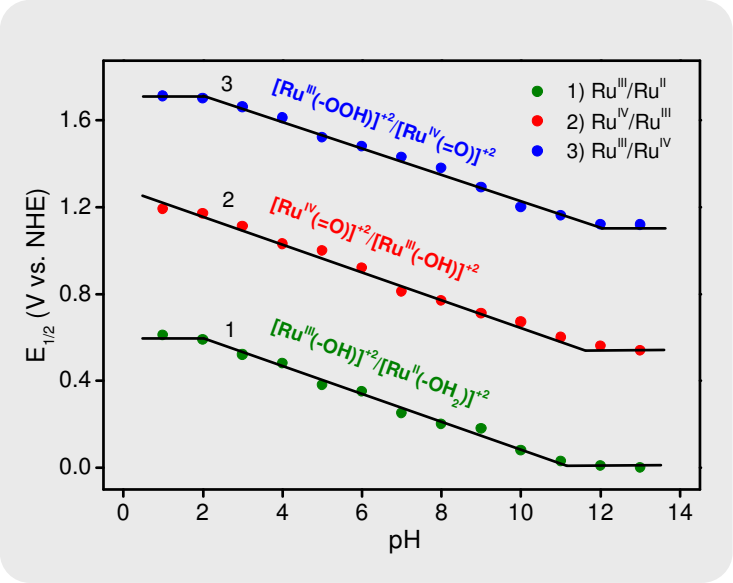

Figure 4.4. Pourbaix diagram for Cat.**Ru**–COOH showing $[Ru^{III}(OH)]^{2+}/[Ru^{II}(OH_2)]^{2+}$, $[Ru^{IV}(=O)]^{2+}/[Ru^{III}(OH)]^{2+}$ and $[Ru^{III}(OOH)]^{2+}/[Ru^{IV}(=O)]^{2+}$ couples generated at a glassy carbon disk (diameter d=5mm) working electrode in 0.1 M aqueous solutions.

From the Pourbaix diagram (Fig. 4.4), the electrochemical polarization for $[Ru^{III}\text{-}(OH)]^{2+}/[Ru^{II}\text{-}(OH_2)]^{2+}$, $[Ru^{IV}(=O)]^{2+}/[Ru^{III}\text{-}(OH)]^{2+}$ and $[Ru^{IV}(=O)]^{2+}/[Ru^{III}\text{-}(OOH)]^{2+}$ at pH=7 translates into the standard free energy differences of 0.67 eV, 1.27 eV and 1.83 eV respectively, in a pH-independent reference frame. Hence the difference in affinity between the $[Ru^{III}\text{-}(OH)]^{2+}$ and $[Ru^{III}\text{-}(OOH)]^{2+}$ intermediate is 3.10 eV, which is well within the range of 3.2±0.1 eV calculated by Rosmeissl and Nørskov [28,35]. As the standard free energy difference for the whole water splitting process is 4.92 eV, a potential difference of 1.15 eV is calculated for the last step towards oxygen evolution involving the $[Ru^{IV}\text{-}(OO)]^{2+}/[Ru^{III}\text{-}(OOH)]^{2+}$ intermediate, which is not potential limiting.

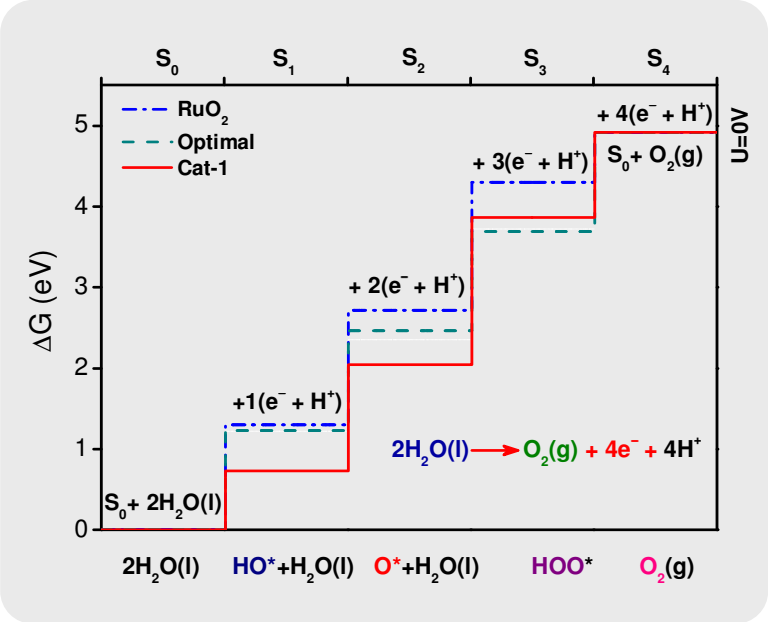

Figure 4.5. Relative Gibbs free energies (ΔG) of reactive species and intermediates, S_0-S_4 (horizontal lines) during catalytic water splitting and oxygen generation for $[(cy)Ru^{II}(dcabpy)OH_2]^{2+}$ (Cat-**1**), compared with the free energy profiles for RuO_2, and the reaction coordinate for the optimal catalyst with four steps each of 1.23 eV [27,28].

Since the complex $[(cy)Ru^{II}(dcabpy)OH_2]^{2+}$ exhibits a pH-dependent feature with the characteristic slope of ~60 mV/pH and produces the catalytic intermediates independent of proton chemical potential, the chemical reference system can be

changed to obtain a universal description of the cycle in terms of its free energy profile along a reaction coordinate that is delineated by the catalytic intermediates in 1.1-1.4 and 1.5-1.8 in chapter 1 [27,35].

The total free energy change for the water oxidation by Cat.**Ru**–COOH complex is ΔG=4.92 eV, which is distributed over the four steps between sequential intermediates, S_1-S_4, as described above. The free energy profile is compared with the standard free energies of the three intermediates in RuO_2 that were calculated with DFT, and with an optimal water oxidation catalyst with ΔG = 1.23 eV for each of four steps, which is very similar to the profile of the natural PS-II (Fig. 4.5) [11,27]. Catalytic water oxidation can proceed at the lowest potential when all steps are downhill. For RuO_2 this requires a minimum overpotential of ~0.4 V [27], while the Cat.**Ru**–COOH modified ITO operates at a moderate overpotential of just ~0.6 V for thousands of cycles and represents a very good artificial system for water splitting.

4.2.4. Catalytic Water Splitting and Oxygen Evolution

The steady state catalytic water electrolysis experiments were performed with the Cat.**Ru**–COOH modified ITO electrode, both in acidic and neutral pH solutions in an electrolysis cell with separate anodic and cathodic compartments. In aqueous acids, a turnover number of more than 6.7×10^5 in 35 hours was achieved at *ca*. 1.89 V (vs. NHE) with a turnover frequency of ~5.33 moles of oxygen per mole of catalyst per second. The current density was >1.7 mA/cm^2 in the beginning and dropped to ~1.65 mA/cm^2 after 13 hours (Fig. 4.6a). The average current density during the whole experiment over 35 hours was >1.6 mA/cm^2. The oxygen generation was monitored *in situ* with a calibrated oxygen electrode as described in the previous chapter [25]. More than 800 μmol of oxygen was produced in 30 hours during water oxidation with a Cat.**Ru**–COOH modified ITO electrode in a 0.1 M acidic solution (inset Fig. 4.6a).

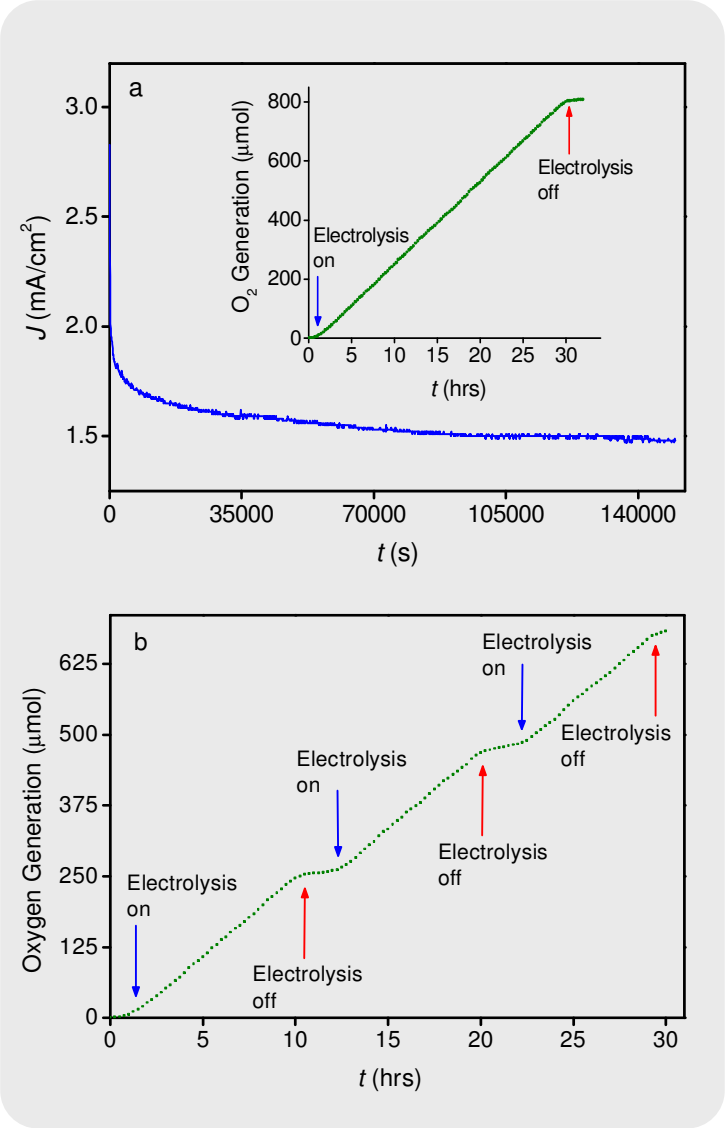

Figure 4.6. (**a**) Controlled-potential water electrolysis (current density mA/cm^2 vs. time) with the Cat.**Ru**–COOH modified ITO electrode in deoxygenated aqueous 0.1 M H_2SO_4 at *ca.* 1.89 V (vs. NHE). The inset shows oxygen generation (in µmol) vs. time for prolonged water electrolysis under similar conditions. (**b**) Successive initiation of water electrolysis (10 hours) and termination (2 hours) with the Cat.**Ru**–COOH modified ITO electrode in deoxygenated aqueous 0.1 M H_2SO_4 at *ca.* 1.89 V (vs. NHE). ITO area A=1 cm^2, (catalyst loading ~1.51–1.65 × 10^{-10} mol/cm^2). (The blue arrows mark the beginning of electrolysis and red arrows point to termination of the electrolysis).

In order to monitor the stability of the catalytic system for intermittent operation, successive electrolysis experiments were performed for consecutive time intervals with the Cat.**Ru**–COOH modified ITO electrode in 0.1 M acidic aqueous solutions. Figure 4.6b shows the activity of the catalyst for three electrolysis runs, with a 2 hours break after 8 and 9 hours of catalytic operation. The rate of oxygen generation remains almost the same for each electrolysis step. This indicates good stability and surface activity of the immobilized Cat.**Ru**–COOH complex in the acidic environment. Also when the system is not being operated for a while, the catalyst stays active and efficient when electrolysis is initiated again.

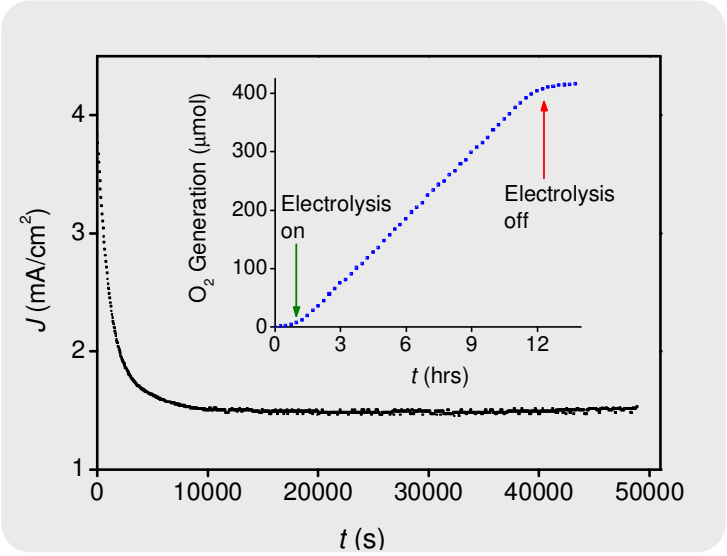

Figure 4.7. Controlled-potential water electrolysis (current mA/cm^2 vs. time) with the Cat.**Ru**–COOH modified ITO electrode in deoxygenated aqueous 0.1M phosphate buffer solution (pH ~ 7.1) at *ca.* 1.45 V (vs. NHE). The inset shows oxygen generation (in µmol) vs. time for prolonged water electrolysis under similar conditions. ITO area A=1 cm^2, (catalyst loading ~1.51–1.65 × 10^{-10} mol/cm^2). (The green arrow indicates the beginning of electrolysis and red arrow point to termination of the electrolysis).

The Cat.**Ru**–COOH modified ITO generates more than 3.1×10^5 turnovers for molecular oxygen at *ca.* 1.5 V (vs. NHE) in only 12 hours, at a turnover rate of ~7.14 moles of oxygen per mole of catalyst per second during electrocatalysis of a

neutral aqueous solution containing 0.1 M phosphate buffer (inset Fig. 4.7). Under steady state conditions, the average current density was more than 1.5 mA/cm^2 (Fig. 4.7). The above numbers are larger than observed for a cobalt phosphate catalyst on an ITO electrode under similar conditions in neutral phosphate buffer solution, *i.e.* 9 µmol of oxygen per hour with a current density of ~1 mA/cm^2 at an overpotential of 0.41 V at pH=7 [10]. For the Cat.**Ru**–COOH modified ITO, the current was stable for more than 15 hours and a stream of oxygen bubbles was running off the catalyst modified ITO electrode with simultaneous hydrogen bubbles generation at the Pt cathode. More than 400 µmol of oxygen was produced in 11 hours in neutral phosphate buffer solution (inset Fig. 4.7).

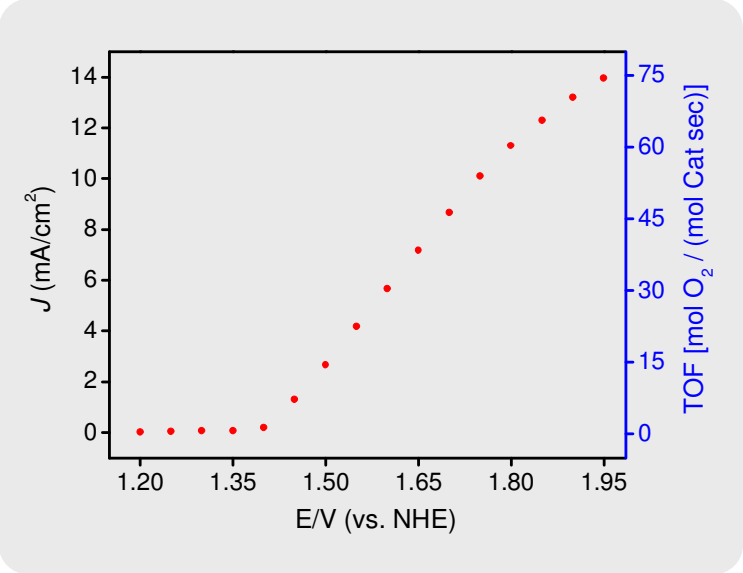

Figure 4.8. TOF (mol O_2 per mol catalyst per second) and oxygen generation (µmol per hour) against the applied potential at the Cat.**Ru**–COOH modified ITO electrode in deoxygenated aqueous in 0.1 M phosphate buffer solution (pH~7.4). ITO area A=1 cm^2, (catalyst loading ~1.51–1.65 × 10^{-10} mol/cm^2).

In the potential cycling catalytic water oxidation experiments, it was also noticed that the oxygen evolution initiates above 1.41 V (vs. NHE) in the neutral phase and the current density rises almost linearly up to 10 mA/cm^2 with increasing potential until E = 1.77 V vs. NHE (Fig. 4.8). This is accompanied by an increase

of the oxygen generation at the Cat.**Ru**–COOH modified ITO electrode, along with enhanced hydrogen evolution at the Pt counter electrode. At higher potential the current density gradually levels off, while an abundant stream of oxygen bubbles is leaving from the ITO surface (Fig. A4.3). The three-parameter relation in Figure 4.8 also shows a linear increase in the TOF of the catalytic system with the applied electrode potential until 1.75 V (vs. NHE). Approximately 350 μmol of oxygen per hour is produced by water oxidation at an oxygen generation rate of >60 mol per mol of catalyst per second, with a current density of ~11 mA/cm^2 (Fig. A4.3).

4.2.5. Catalytic Mechanism for Water Oxidation

On the basis of electrochemical investigations and potential vs. pH behaviour of Cat.**Ru**–COOH complex, a pentacyclic mechanism for catalytic water oxidation (Scheme 1) is deducted that proceeds along the reaction coordinate depicted in Figure 4.5. A double positive charge is maintained in successive proton coupled electron transfer steps, similar to the modified S-cycle for PS-II [11,12]. Induction of the catalyst is accomplished by the exchange of the chloride anion by a H_2O molecule. This produces a $[Ru^{II}(\text{-}OH_2)]^{2+}$ complex that can equilibrate its electron and proton affinities and bridge between the electrode and the surrounding medium via the aqua ligation. $[Ru^{III}\text{-}(OH)]^{2+}/[Ru^{II}\text{-}(OH_2)]^{2+}$ and $[Ru^{IV}(=O)]^{2+}/[Ru^{III}\text{-}(OH)]^{2+}$ transitions are realized by two successive proton coupled electron transfer oxidation steps after aqua induction in the first half of the water oxidation cycle [18,29].

The CV's show a pH dependent potential for the $E_{1/2}$ of the $[Ru^{III}\text{-}(OH)]^{2+}/[Ru^{II}\text{-}(OH_2)]^{2+}$, $[Ru^{IV}(=O)]^{2+}/[Ru^{III}\text{-}(OH)]^{2+}$ couples, higher potential $[Ru^{IV}(=O)]^{2+}/[Ru^{III}\text{-}(OOH)]^{2+}$ species and oxygen onset potential during water oxidation (Figs. 4.2-4.4). Apparently the $[Ru^{IV}(=O)]^{2+}$ complex is not converted into a longer living $[Ru^{V}(=O)]^{3+}$ intermediate before second water ligation, the mechanism reported earlier for single site catalysts [25,26]. The addition of the second water molecule with the complex $[Ru^{IV}(=O)]^{2+}$ probably produces a short lived $[Ru^{II}\text{-}(O_2H_2)]^{2+}$ type intermediate that enables the balancing of proton and electron affinities at the beginning of the second half of the catalytic cycle [18].

This then undergoes a third consecutive PCET conversion into $[Ru^{III}(\text{-}OOH)]^{2+}$, as shown by a slope of ~60 mV/pH (Fig. 4.4). In this way the formation of $[Ru^{V}(=O)]^{3+}$ or other higher oxidation ruthenium intermediates that would arise when the non-protic $[Ru^{IV}(=O)]^{2+}$ intermediate is oxidized prior to addition of a second water molecule, can be avoided [18,25]. Apparently, the water coordination with $[Ru^{IV}(=O)]^{2+}$ is not rate-limiting, and it is probably facilitated by the wide angle between bpy-Ru and the small multifunctional *p*-cymene that might switch back and forth its topology [36].

Scheme 4.1. Proposed pentacycle catalytic mechanism for water oxidation and oxygen evolution by $[(cy)Ru^{II}(L_2bpy)\text{-}OH_2]$ type complexes (L_2 is COOH or PO_3H_2). Red arrows represent four electron removal steps, each coupled with a proton transfer (blue arrows) and green arrows indicate electron transfer to ITO electrode via the linker. Characteristic for the mechanism is a complex with overall charge +2 and alternating Ru oxidation states $Ru^{II}/Ru^{III}/Ru^{IV}$ – $Ru^{III}/Ru^{IV}/Ru^{II}$ that are enabled by rapid, non rate-limiting oxidation processes, following association of a second water molecule and internal rearrangements and subsequent exchange of O_2 by H_2O.

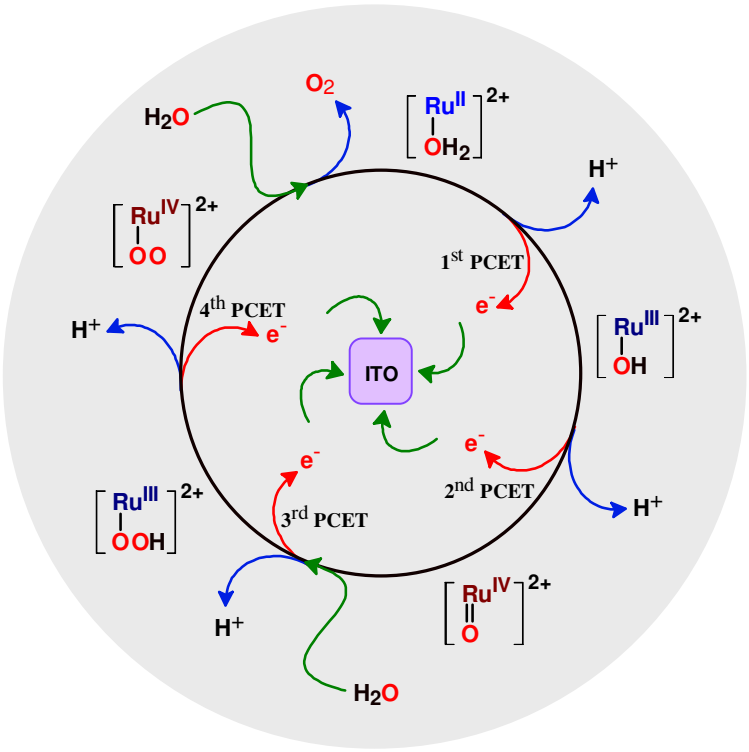

This mediates the electron affinity of the system with its charge stabilization properties to allow for both the coordination of a second OH_2 in an octahedral Ru surrounding and rapid PCET interconversion to a $[Ru^{III}\text{-}(OOH)]^{2+}$ species by lowering the barrier for this process. Thus, the surface anchored Cat.**Ru**–COOH eliminates the need for an increase of the redox potential by increasing the valence state of the Ru site and the entire complex without ejection of a proton. The different rate-limiting ruthenium couples in the catalyst $[(cy)Ru^{II}(dcabpy)OH_2]^{2+}$ all show for the slope of ~60 mV/pH that is characteristic for reversible kinetics at the glassy carbon electrode, even at higher pH up to 12 and for none of the steps there is an underlying mechanism delaying proton transfer and affecting the kinetics. This matches the PCET characteristics of the natural PS-II system and of RuO_2 [11,27]. It represents a compelling advantage of the Cat.**Ru**–COOH complex over earlier molecular water oxidation complexes, and allows for a catalytic cycle of kinetically reversible proton coupled electron transfer regime while maintaining a divalent complex throughout the cycle, according to the mechanism proposed in Scheme 4.1.

4.3. CONCLUSIONS

In conclusion, a surface immobilized mononuclear ruthenium complex for electro-driven water oxidation, based on a stable, easy accessible and highly efficient mono catalytic site system, is discussed in this chapter. The complex appears electrocatalytically active and robust when anchored to the electrode surface by a linker group. A catalyst modified ITO electrode in neutral solution generated more than 400 μmol of oxygen in 11 hours in a controlled-potential water electrolysis experiment at relatively low overpotential with a current density >1.5 mA/cm^2. The catalyst turnovers were more than 3.1×10^5 in 12 hours, at a turnover rate of ~7.14 moles of oxygen per mole of catalyst per second. In another set of experiments in aqueous acids, the oxygen generation turnover numbers were more than 6×10^5 in 35 hours with turnover frequencies of ~5.33 per second. One cm^2 of electrode

covered with catalyst produced 800 μmol of oxygen in 30 hours of water electrolysis at a current density of ~1.65 mA/cm^2. The catalytic system is capable of generating ~450 μmol of oxygen per hour in neutral water at an oxygen generation rate up to 80 per mol of catalyst per second, with a current density of >14 mA/cm^2. The above numbers are in excess of values reported for other known molecular catalysts for homogeneous and electrocatalytic oxygen evolution [18,24-26]. This study describes thus a good oxygen generation catalytic system for neutral and acidic water electro-oxidation and opens new doors towards efficient, stable and easy accessible water splitting assemblies for clean fuel generation.

Although we do not have access yet to detailed spectroscopic data for the catalyst on ITO, the CV analyses provide converging evidence that the catalyst is intact and active on the ITO surface. First, there is a catalytic effect at less overpotential than for the bare ITO that gives a water oxidation indication only at > 2.5 V (vs. NHE); second, the magnitude of the overpotential does not correspond with the overpotential for the most common decomposition product RuO_2; third, the magnitude of the overpotential is essentially the same as for the catalyst on the glassy carbon electrode; fourth, there is pH dependence and it is essentially the same over a range from 1-10.5 as for the catalyst on the glassy carbon electrode. On the other hand, it is sometimes difficult to identify the first two ruthenium transitions for the very small amount of catalyst in contact with the ITO surface [25,26], which can be attributed to slow electrode kinetics [18,25]. The ITO electrode is a mixture of two oxides and chemically different from the inert glassy carbon for which (i) the Nernst behaviour of the intermediates was determined and (ii) enhanced catalysis relative to the catalyst in solution was already observed. Although the bare ITO does not give a polarization response (Fig 4.3) [9,25], it is in principle possible that complex mechanisms involving a combination of molecular and semiconductor electronic processes at the interface between the catalyst and the ITO occur. After continuous operation for many hours, inactive spots develop on the electrode at the locations where oxygen bubbles were generated. Since ITO is a relatively inert electrode and the blank electrode does not

give an electrocatalytic response, these spots were attributed to inactivation or deterioration of the catalyst, possibly involving breakdown of the cymene that is thought to undergo ligation switching in every cycle in the proposed mechanism of Scheme 4.1.

In this way nicely the fundamental chemical paradox of water splitting transpires, that a durable system requires sturdiness, while multi electron catalysis requires flexibility. Apparently the molecular catalytic system for efficient water splitting discussed here offers an attractive compromise in this respect, with its high TON's and TOF's that exceed the values reported thus far for other catalytic systems. Further validation of the system and resolving the mechanism that makes that the interface of catalyst and electrode allow the rapid switching of the electronic properties for many cycles will have to be investigated by time resolved spectroelectrochemical studies in a future step.

4.4. MATERIALS AND METHODS

Unless otherwise specified, the solutions were prepared in ultra-pure water (Millipore MilliQ® A10 gradient, 18.2 MΩ cm, 2–4 ppb total organic content). The electrochemical measurements were carried out in carefully Ar-purged deoxygenated aqueous solutions at room temperature. Compounds, ligands and catalyst complexes were synthesized in argon/nitrogen atmosphere. ITO coated glass slides (10 cm × 2.5 cm), $[RuCl_2(p\text{-cymene})]_2$ dimer and $RuCl_3.nH_2O$ were obtained from Sigma-Aldrich Co., and used as received. 4,4′-dicarboxylic acid-2,2′-bipyridine (H_2dcabpy) and 4,4'-diphosphonic acid-2,2′-bipyridine (H_4dphbpy) were prepared using literature procedures [37,38]. ^{1}H NMR spectra and UV-vis measurements are conducted as described in the previous chapter.

General procedures for glassware and cell cleaning, electrodes type and preparation, and instrumentation for electrochemical measurements are described in section 3.4. ITO coated glass slides (1 cm × 2.5 cm, exposed surface area 1.0 cm^2) were used as a working electrode (WE) for the surface bound electro-catalytic

CV studies. The catalytic water electrolysis and oxygen evolution measurement investigations were carried out in a three electrode double junction H-type glass cell where the reference electrode chamber was separated by a very fine porosity glass frit. In catalytic water electrolysis, the WE was ITO with the specification mentioned above. Platinum wire (thickness 1 mm), shaped into a spiral, was used as a counter electrode (CE). The catalytic oxygen evolution was measured *in situ* using a calibrated oxygen electrode connected with a digital O_2 meter (YSI, Inc., Model 550A).

Prior to the water splitting investigation and oxygen measurements experiments, the aqueous solutions were purged with high-purity argon (Linde Gas, 6.0) for at least 30 min before each measurement. The whole cell assembly was airtight and care was taken to prevent any passage of air and oxygen into the test solution in the cell. Oxygen elimination from the continuously Ar-bubbled aqueous solutions was carefully verified by scanning the freshly polished Pt disk (diameter d=3 mm, embedded in PTFE) electrode on RDE assembly from 500-2500 rpm until no oxygen detection was observed.

Immobilization of the catalyst on ITO coated glass slides (1 cm × 2.5 cm) was accomplished by soaking the electrode (4-8 hours) in 0.1 mM stock solution of catalyst in either pure deoxygenated water or 0.1M aqueous HNO_3. For controlled –potential water electrolysis studies, a 15-25 μL aliquot of 0.01 mM catalyst stock solution was placed on the ITO coated glass electrode to obtain the catalyst loading of ~1.5 – 2.5 × 10^{-10} mol/cm^2. The density of electrocatalytically active species per cm^2 of ITO surface was estimated from the CV's. The voltammograms for Ru^{III}/Ru^{II} transition between 0.40 and 0.85 V (Fig. A4.4) were integrated after background current correction according to equation 4.1:

$$\rho_{cat} = \frac{\int (I_{cat} - I_0)\, d\mathrm{V}}{AS\, e_0} \left[\frac{\text{el.sp.}}{\text{cm}^2}\right], \qquad (4.1)$$

and converted into number of moles of the catalyst per cm^2 of the electrode [25,26]. Here ρ_{cat} is number of electrocatalytically active species per electrode area (el.sp./cm^2), I_{cat} and I_0 is catalytic and background currents, respectively, V is potential, A is area (1 cm^2), S is scan rate (100 mV/sec) and e_0 is the elementary charge. The ITO, after each surface modification, was dried and the catalyst modified ITO slides were put inside a groove (1.1 mm × 5 mm) of a stainless steel rod (length l=18 cm and diameter d=0.5 cm) and fixed with Parafilm or Teflon tape. In some cases, a crocodile clip was use to hold the catalyst coated ITO glass slide for electrocatalytic water oxidation experiments.

Synthesis

4.4.1. Chloro complex [(cy)Ru^{II}(H_2dcabpy)Cl]Cl (**Ru**–COOH)

4,4′-dicarboxylic acid-2,2′-bipyridine (H_2dcabpy: 0.244 g, 1.0 mmol) was dissolved in 0.5 mL water containing NaOH (0.08 g, 2.0 mmol) and MeOH (25 mL) was added to it. This mixture was poured into a stirred mixture of $[RuCl_2(p\text{-cymene})]_2$ dimer (0.362 g, 0.5 mmol) in absolute MeOH (20 mL). The whole reaction mixture was further stirred for 2 hours at 40-45 °C. The solution was cooled to room temperature and pH was lowered to 1-2 by addition of 0.5 M HCl. The free ligand was filtered off and the solvent mixture was evaporated under vacuum. The solid orange chloro complex [(cy)Ru^{II}(H_2dcabpy)Cl]Cl thus obtained was re-precipitated from MeOH or acetone by addition of ether/hexane. Yield 0.43 g, 78 %. ^{1}H NMR (CD_3OD, 295 K, δppm, J Hz): 9.66 (d, 2H, $H^{6,6'}{}_{dcabpy}$, J 5.76); 8.99 (s, 2H, $H^{3,3'}{}_{dcabpy}$); 8.22 (dd, 2H, $H^{5,5'}{}_{dcabpy}$, J 1.49, J 5.79); 6.19 (d, 2H, $Ar_{p\text{-cy}}$, J 6.33); 5.95 (d, 2H, $Ar_{p\text{-cy}}$, J 6.33); 2.66 (sep, 1H, -C$\underline{H}(CH_3)_{2\ p\text{-cy}}$); 2.27 (s, 3H, $CH_{3\ p\text{-cy}}$); 1.06 (d, 6H, -CH(C$\underline{H}_3)_{2\ p\text{-cy}}$, J 6.91), Analysis found: C, 45.56%; H, 4.41%; N, 4.85%. Calculated: C, 45.74%; H, 4.36%; N, 4.86% for $C_{22}H_{22}N_2O_4Ru_1Cl_2.1.5H_2O$ complex.

4.4.2. Chloro Complex [(cy)Ru^{II}(H_4dphbpy)Cl]Cl (**Ru**–PO_3H_2)

The chloro complex [(cy)Ru^{II}(H_4dphbpy)Cl]Cl was prepared in a similar manner as described above (section 4.4.1) using 4,4′- diphosphonic acid -2,2′-bipyridine (H_4dphbpy: 0.316 g, 1.0 mmol) in 0.5 mL water containing NaOH (0.16 g, 4.0 mmol) instead of 4,4′-dicarboxylic acid-2,2′-bipyridine. Yield 0.41 g, 66 %. ^{1}H NMR (CD_3OD, 295 K, δppm, *J* Hz): 9.29 (d, 2H, $H^{6,6'}{}_{dphbpy}$, *J* 6.11); 8.81 (s, 2H, $H^{3,3'}{}_{dphbpy}$); 7.97 (dd, 2H, $H^{5,5'}{}_{dphbpy}$, *J* 2.01, *J* 6.15); 6.12 (d, 2H, $Ar_{p\text{-cy}}$, *J* 6.37); 5.87 (d, 2H, $Ar_{p\text{-cy}}$, *J* 6.37); 2.65 (sep, 1H, -C<u>H</u>$(CH_3)_{2\ p\text{-cy}}$); 2.21 (s, 3H, $CH_{3\ p\text{-cy}}$); 1.03 (d, 6H, -CH(C<u>H</u>$_3)_{2\ p\text{-cy}}$, *J* 6.91), Analysis found: C, 38.08%; H, 3.16%; N, 4.86%. Calculated: C, 38.60%; H, 3.89%; N, 4.50% for $C_{20}H_{24}N_2O_6P_2Ru_1Cl_2$ complex.

4.4.3. Catalyst Complex [(cy)Ru^{II}(H_2dcabpy)-OH_2]$^{2+}$ (Cat.**Ru**–COOH)

The chloro complex [(cy)Ru^{II}(H_2dcabpy)Cl]Cl was converted into the aqua (OH_2) catalyst [(cy)Ru^{II}(H_2dcabpy)-OH_2]$^{2+}$ by stirring with aqueous solution containing 2.1 eq. of $AgNO_3$ or silver hexafluorophosphate in methanol (1:1, H_2O/MeOH) for 30 minutes. The white precipitates were filtered off and the solvent mixture was evaporated under vacuum. The yellow solid aqua complex thus obtained was re-precipitated from acetone or MeOH by addition of ether/hexane.

4.4.4. Catalyst Complex [(cy)Ru^{II}(H_4dphbpy)-OH_2]$^{2+}$ (Cat.**Ru**–PO_3H_2)

The bright yellow aqua complex [(cy)Ru^{II}(H_4dphbpy)-OH_2]$^{2+}$ was prepared in a similar manner as described above (section 4.4.3) using chloro complex of 4,4′-diphosphonic acid -2,2′-bipyridine instead of 4,4′-dicarboxylic acid-2,2′-bipyridine.

REFERENCES

01- J. Chow, R. J. Kopp and P. R. Portney, *Science* **2003**, *302,* 1528–1531.

02- N. S. Lewis, *Nature* **2001**, *414,* 589–590.

03- T. J. Meyer, *Nature* **2008**, *451*, 778–779.

04- Z. Zou, J. Ye, K. Sayama and H. Arakawa, *Nature* **2001**, *414*, 625–627.

05- E. E. Barton, D. M. Rampulla and A. B. Bocarsly, *J. Am. Chem. Soc.* **2008**, *130*, 6342–6342.

06- W. J. Youngblood, S.-H. A. Lee, K. Maeda and T. E. Mallouk, *Acc. Chem. Res.* **2009**, *42*, 1966–1973.

07- K. Sivula, R. Zboril, F. L. Formal, R. Robert, A. Weidenkaff, J. Tucek, J. Frydrych and M. Grätzel, *J. Am. Chem. Soc.* **2010**, *132*, 7436–7444.

08- T. Wada, K. Tsuge and K. Tanaka, *Angew. Chem. Int. Ed. Engl.* **2000**, *39*, 1479–1482.

09- F. Liu, T. Cardolaccia, B. J. Hornstein, J. R. Schoonover and T. J. Meyer, *J. Am. Chem. Soc.* **2007**, *129*, 2446–2447.

10- M. W. Kanan and D. G. Nocera, *Science* **2008**, *310***,** 1019–1021.

11- H. Dau, C. Limberg, T. Reier, M. Risch, S. Roggan and P. Strasser, *ChemCatChem* **2010**, *2*, 724–761.

12- M. H. V. Huynh and T. J. Meyer, *Chem. Rev.* **2007**, *107*, 5004–5064.

13- J. Limburg, J. S. Vrettos, L. M. Liable-Sands, A. L. Rheingold, R. H. Crabtree and G.W. Brudvig, *Science* **1999**, 283, 1524–1527.

14- T. Wada, K. Tsuge and K. Tanaka, *Inorg. Chem.* **2001**, *40,* 329–337.

15- R. Zong and R. P. Thummel, *J. Am. Chem. Soc.* **2005**, *127*, 12802–12803.

16- N. D. McDaniel, F. J. Coughlin, L. L. Tinker and S. Bernhard, *J. Am. Chem. Soc.* **2008**, *130*, 210–217.

17- S. Romain, F. Bozoglian, X. Sala and A. Llobet, *J. Am. Chem. Soc.* **2009**, *131*, 2768–2769.

18- D. J. Wasylenko, C. Ganesamoorthy, M. A. Henderson, B. D. Koivisto, H. D. Osthoff and C. P. Berlinguette, *J. Am. Chem. Soc.* **2010**, *132*, 16094–16106.

19- L. Duan, A. Fischer, Y. Xu and L. Sun, *J. Am. Chem. Soc.* **2009**, *131*, 10397–10399.

20- J. F. Hull, D. Balcells, J. D. Blakemore, C. D. Incarvito, O. Eisenstein, G. W. Brudvig and R. H. Crabtree, *J. Am. Chem. Soc.* **2009**, *131*, 8730–8731.

21- M. Yagi, E. Tomita, S. Sakita, T. Kuwabara and K. Nagai, *J. Phys. Chem. B* **2005**, *109*, 21489–21491.

22- F. Jiao and H. Frei, *Angew. Chem. Int. Ed.* **2009**, *48*, 1841–1844.

23- M. M. Najafpour, T. Ehrenberg, M. Wiechen and P. Kurz, *Angew. Chem. Int. Ed.* **2010**, *49*, 2233–2237.

24- J. Mola, E. Mas-Marza, X. Sala, I. Romero, M. Rodriguez, C. Viñas, T. Parella and A. Llobet, *Angew. Chem. Int. Ed.* **2008**, *47*, 5830–5832.

25- Z. Chen, J. J. Concepcion, J. W. Jurss and T. J. Meyer, *J. Am. Chem. Soc.* **2009**, *131*, 15580–15581.

26- J. J. Concepcion, J. W. Jurss, P. G. Hoertz and T. J. Meyer, *Angew. Chem. Int. Ed.* **2009**, *48*, 9473–9476.

27- J. Rossmeisl, K. Dimitrievski, P. Siegbahn and J. K. Nørskov, *J. Phys. Chem. C* **2007**, *111*, 18821–18823.

28- J. Rossmeisl, Z. W. Qu, H. Zhu, G.-J. Kroes and J. K. Nørskov, *J. Electroanal. Chem.* **2007**, *607*, 83–89.

29- J. J. Concepcion, M.-K. Tsai, J. T. Muckerman and T. J. Meyer, *J. Am. Chem. Soc.* **2010**, *132*, 1545–1557.

30- (a) K. S. Joya and H. J. M. de Groot, Metal complex and use as multi-electron catalyst. *Netherlands Patent Application* no. 2005512; Oct **2010**; (b) *International Patent Application* no. PCT/NL2011/050673; Oct **2011**.

31- S. B. Wendicke, E. Burri, R. Scopelliti and K. Severin, *Organometallics* **2003,** *22*, 1894–1897.

32- Md. K. Nazeeruddin, S. M. Zakeeruddin, J.-J. Lagref, P. Liska, P. Comte, C. Barolo, G. Viscardi, K. Schenk and M. Graetzel, *Coord. Chem. Rev*. **2004**, *248*, 1317–1328.

33- R. S. Nicholson and I. Shain, *Ana. Chem.* **1964**, *36*, 706–723.

34- L. Tong, L. Duan, Y. Xu, T. Privalov and L. Sun, *Angew. Chem. Int. Ed*. **2011**, *50*, 445–449.

35- Á. Valdés, Z.-W. Qu, G.-J. Kroes, J. Rossmeisl and J. K. Nørskov. *J. Phys. Chem. C.* **2008**, *112*, 9872–9879.

36- G. Winkhaus and H. Singer, *J. Organometal. Chem.* **1967**, *7*, 487–491.

37- P. G. Hoertz, A. Staniszewski, A. Marton, G. T. Higgins, C. D. Incarvito, A. L. Rheingold and G. J. Meyer, *J. Am. Chem. Soc.* **2006**, *128*, 8234–8245.

38- S. Ferrere, *Chem. Mater.* **2000**, *12*, 1083–1089.

Appendix A4

[{$(PO_3H_2)_2$-bpy}-Ru^{II}-(cy)Cl]Cl

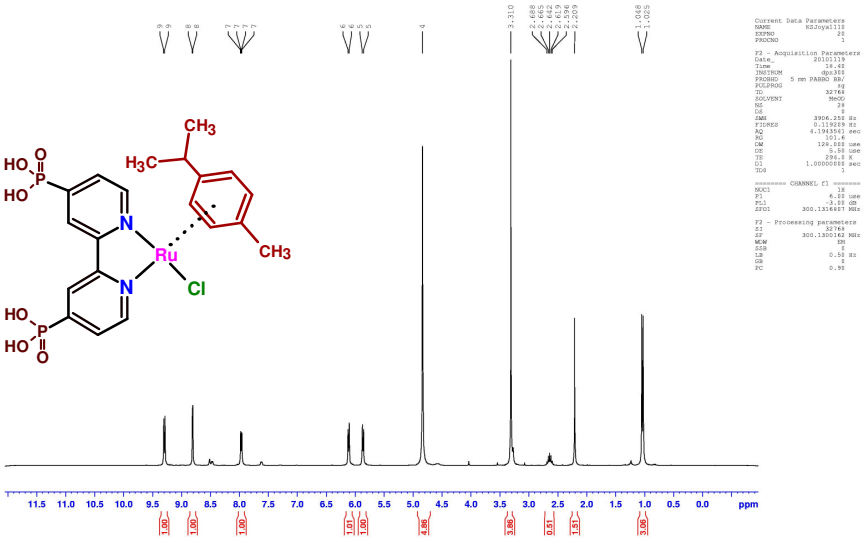

[{$(COOH)_2$-bpy}-Ru^{II}-(cy)Cl]Cl

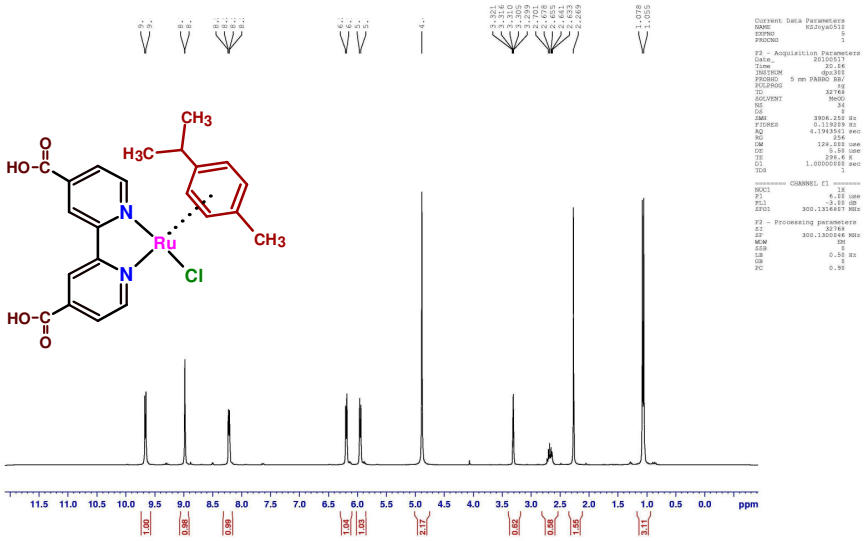

Figure A4.1. Proton-NMR spectra of the water oxidation complexes, **Ru**–PO_3H_2 and **Ru**–COOH.

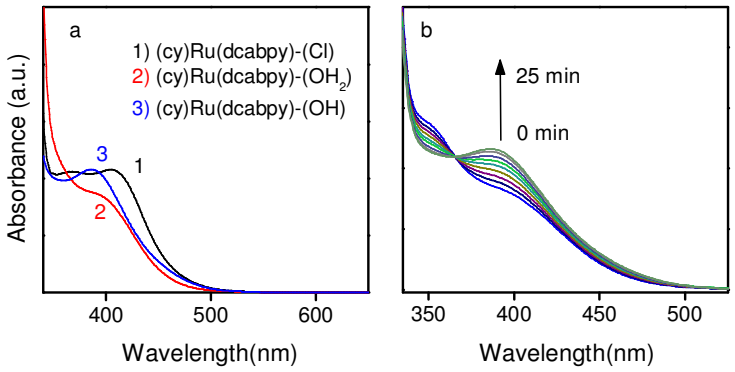

Figure A4.2. (**a**) Electronic absorption spectra of $[(cy)Ru(dcabpy)\text{-}(Cl)]^{+}$, $[(cy)Ru(dcabpy)\text{-}(OH_2)]^{2+}$ and $[(cy)Ru(dcabpy)\text{-}(OH)]^{+}$ complexes and (**b**) conversion of $[(cy)Ru(dcabpy)\text{-}(OH_2)]^{2+}$ into $[(cy)Ru(dcabpy)\text{-}(OH)]^{+}$ complex in 0.5 M NaOH. (The concentration of all complexes is 7.5×10^{-5} M).

Figure A4.3.

Relation between the applied electrolysis potential, oxygen evolution rate (μmol per hour) and TOF (O_2 mol per mol of catalyst per second) for the Cat.**Ru**–COOH modified ITO electrode in deoxygenated aqueous 0.1M phosphate buffer solution (pH ~ 7.1). (E/V vs. NHE, ITO area A=1 cm^2, catalyst loading ~1.51–1.65 × 10^{-10} mol/cm^2).

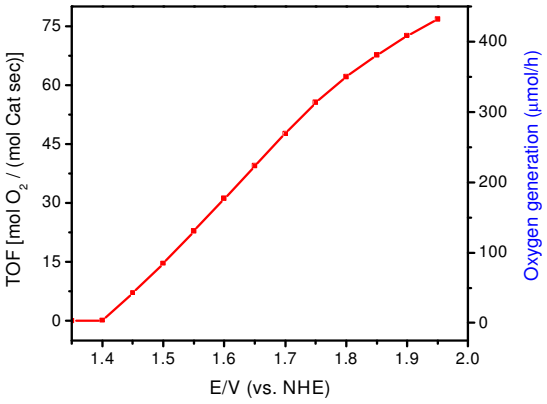

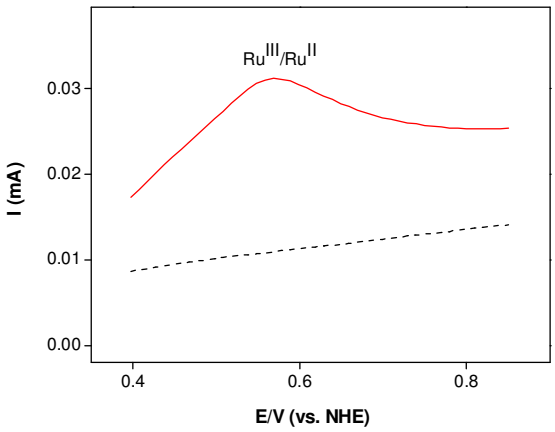

Figure A4.4.
CV's for blank ITO and Cat.**Ru**–COOH/ITO system. The number of active catalytic species were estimated by integrating peak area for the Ru(III/II) transition in deoxygenated aqueous 0.1 M HNO_3 . Scan rate was 100 mV/sec, ITO area A=1 cm^2.

Chapter 5

Catalytic Electro-assisted Water Splitting by Single Site Iridium Complexes

ABSTRACT

In this chapter, mono iridium complexes of the type $[(Cp^*)\text{-}Ir^{III}\text{-}(N\text{–}N)\text{-}OH_2]^{2+}$ for homogeneous catalytic water oxidation to molecular oxygen as well as surface immobilized electro-driven catalytic water splitting are described. Chloro complexes $[(Cp^*)\text{-}Ir^{III}\text{-}(N\text{–}N)\text{-}Cl]^{+}$ (Cp* is pentamethylcyclopentadiene and N–N is a dinitrogen ligand) were obtained by stirring a reaction mixture of $[IrCl_2(Cp^*)]_2$ with dinitrogen ligands in methanol. By OH_2 exchange in aqueous solution the $[(Cp^*)\text{-}Ir^{III}\text{-}(N\text{–}N)\text{-}OH_2]^{2+}$ complexes are obtained that are activated for water splitting catalysis. For electro-assisted water oxidation catalysis, the $[(bpy)Ir^{III}(Cp^*)OH_2]^{2+}$ catalyst was immobilized on an indium doped tin oxide (ITO) working electrode surface by anchoring groups COOH or PO_3H_2 introduced at the 4,4' positions on the dinitrogen ligand. Controlled-potential water electrolysis generates more than 2.1×10^5 turnovers at a rate of >6.5 moles of oxygen per mole of catalyst per second. This study presents the first example of $[(Cp^*)\text{-}Ir^{III}\text{-}(N\text{–}N)\text{-}OH_2]^{2+}$ type aqua ligated catalysts for water oxidation at an electrode surface.

Based on: K.S. Joya and H.J.M. de Groot, **2011** (*submitted*).

5.1. INTRODUCTION

Although most of the water oxidation catalysis research has been oriented towards ruthenium and manganese complexes with a polypyridyl ligand architecture [1-6], both for homogeneous as well as surface immobilized electrochemical systems [7-13], very recently several iridium based complexes have been introduced that show relatively high turn over frequency (TOF) for oxygen evolution in homogeneous investigations [14,15]. However, the stability and turnover numbers (TON) were not high enough to allow incorporation of the catalyst in light driven electrochemical water splitting devices for fuel generation [16,17].

As it is explained in the preceding chapter, an active oxygen evolving complex has to be immobilized on a conducting surface for application in operational electrocatalytic or light driven water splitting devices, and iridium based molecular complexes are not yet studied in electro-driven systems [18-22]. Brudvig and Crabtree recently described a Cp*-Ir aqua or hydroxo catalyst named "blue layer" that was generated by anodic deposition in a pH=6 aqueous potassium nitrate solution [23]. The catalyst operates with a current density up to 1.4 mA/cm^2 at ~1.4 V (vs. NHE) for water oxidation in 0.1M KNO_3 (pH=6) electrolyte solution. SEM analysis of the electrodeposited matrix reveals a film thickness between 1 and 2 μm, which represents a multilayer deposition on a fluorine-doped tin oxide (FTO) electrode surface and the formation of oxides of iridium cannot be excluded [23,24].

In this chapter, an immobilized catalytic electro-assisted water oxidation assembly using a linker modified L_2bpy-Ir^{III}Cp* complex (L is COOH and PO_3H_2 and bpy is 2,2′-bipyridine) for surface anchoring on an indium-doped tin oxide (ITO) working electrode is described (Fig. 5.1). An ITO surface of 1 cm^2 covered with the catalyst layer generates rapid turnover rate with high TON's for molecular oxygen during controlled-potential water electrolysis [25].

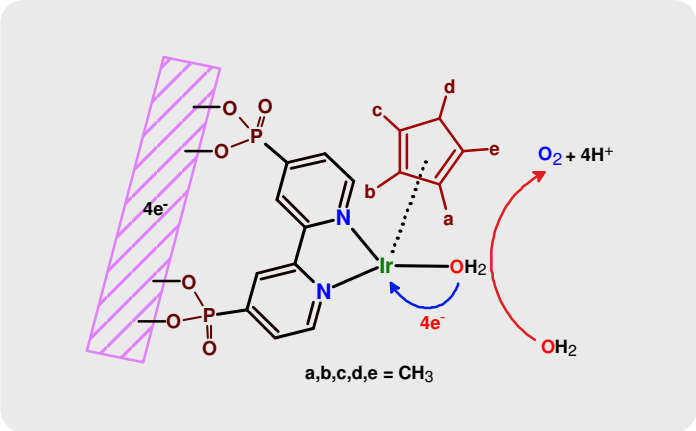

Figure 5.1. Schematic representation of the mono-iridium complex anchored to a conducting oxide surface (ITO) with linker (L = PO_3H_2) for electro-assisted water oxidation.

In addition, three aqua ligated iridium catalysts with different dinitrogen ligands $[(N–N)Ir^{III}(Cp^*)\text{-}OH_2]^{2+}$, analogous to the recently reported chloro or iodo bonded mono iridium complexes [26], are presented here and tested for homogeneous water oxidation studies (Fig. 5.2). While for the earlier examples exchange of a halogen with a neutral water molecule to instigate the water oxidation cycle produces an initial lag phase due to slow dissociation of the halogen from the iridium centre, a faster rate and efficient catalytic activity is observed for the aqua ligated mono iridium complexes described in this chapter [26].

5.2. RESULTS AND DISCUSSION

5.2.1. Catalytic Complexes Synthesis and Characterization

For homogeneous water oxidation catalysis, the iridium catalysts $[(bpy)Ir^{III}(Cp^*)\text{-}OH_2]^{2+}$ (Cat.**Ir**–bpy), $[(phen)Ir^{III}(Cp^*)\text{-}OH_2]^{2+}$ (Cat.**Ir**–phen) and $[(bpm)Ir^{III}(Cp^*)\text{-}OH_2]^{2+}$ (Cat.**Ir**–bpm), are obtained by immersion of the chloro complexes into a water methanol mixture containing silver nitrate or hexafluorophosphate salt (Fig.

5.2). The removal of the Cl^- after aqua induction is important to avoid the involvement of the halogen ions with the water oxidation process [27].

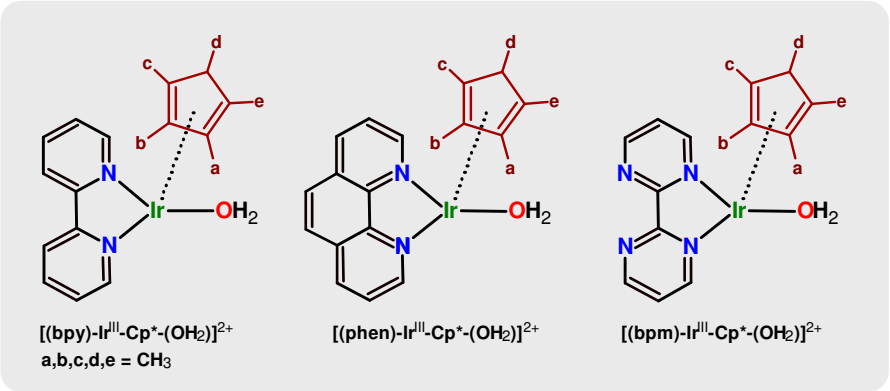

Figure 5.2. Mono iridium pentamethylcyclopentadiene (Cp*) derived 2,2′-bipyridine, phenanthroline (phen) and bipyrimidine (bpm) mono nuclear complexes [25].

The crystal structures of these complexes reveal a large bite angle of the iridium center with respect to the dinitrogen ligand and the aromatic Cp*. This possibly facilitates the aqua exchange at the iridium catalytic site and provides a wide gap for OH_2 coordination between the bpy-Ir and the cyclic conjugated hydrocarbon [25]. The strong electron donating character of the Cp* ligand helps to prevent the formation of higher oxidation iridium intermediates during the catalytic cycle [26].

The linker modified complexes with COOH and PO_3H_2 units at the 4,4′-positions in the $[(bpy)Ir^{III}(Cp^*)Cl]^+$ complex and the $[(bpy)Ir^{III}(Cp^*)\text{-}OH_2]^{2+}$ catalyst for electrochemical water oxidation were synthesized by stirring the mixture of the H_2dcabpy (4,4′-dicarboxylic acid-2,2′-bipyridine) or the H_4dphbpy (4,4′-diphosphonic acid-2,2′-bipyridine) ligand with $[IrCl_2(Cp^*)]_2$ dimer. The chloro complexes thus obtained are transformed into $[(H_2dcabpy)Ir^{III}(Cp^*)\text{-}OH_2]^{2+}$ (Cat.**Ir**–COOH) and $[(H_4dphbpy)Ir^{III}(Cp^*)\text{-}OH_2]^{2+}$ (Cat.**Ir**–PO_3H_2) by stirring with aqueous silver hexafluorophosphate salt or $AgNO_3$ in methanol. (see synthesis detail, ^{1}H-NMR and elemental analysis in section 5.4). *In situ* aqua exchange of the

chloro complex and deprotonation to form the $[(bpy)Ir^{III}(Cp^*)\text{-}OH]^{2+}$ complex was followed by UV-vis studies (Fig. A5.2).

5.2.2. Cyclic Voltammetry and Homogeneous Water Oxidation

Unlike the single-site ruthenium complexes discussed in the previous chapters, the electrochemistry of the mono iridium catalysts shows no apparent pH dependence of the overpotential for oxygen evolution even in alkaline media pH > 7 with the catalyst in contact with the glassy carbon electrode (Fig. A5.3). It was recently postulated that for the catalysts $[(Cp^*)\text{-}Ir^{III}\text{-}(N–C)\text{-}Cl]^+$ and $[(Cp^*)\text{-}Ir^{III}\text{-}(N–N)\text{-}Cl]^+$ (where N–C is phenyl-pyridine and N–N is bipyridine), the iridium oxidation into $[Ir^{IV}\text{-}(OH)]^{2+}/[Ir^{III}\text{-}(OH_2)]^{2+}$ and $[Ir^{V}{=}O)]^{2+}/[Ir^{IV}\text{-}(OH)]^{2+}$ redox couples is proceeded by two consecutive proton coupled electron transfer (PCET) steps [26]. For catalyst Cat.**Ir**–COOH, the weak polarization signals for the first two redox transitions are ascribed to slow electrode kinetics of the complexes under electrochemical conditions, also at a higher scan rate [28]. At pH > 9, a current wave appears at *ca*. 1.19 V (vs. NHE), which grows with increasing pH at the same potential (Figure A5.3). This catalytic wave apparently indicates current flow leading to water oxidation but, for better understanding, the catalyst was immobilized on an ITO electrode for electro-driven water oxidation and oxygen evolution studies (5.2.3).

The three aqua iridium complexes Cat.**Ir**–bpy, Cat.**Ir**–phen and Cat.**Ir**–bpm were tested for homogeneous water oxidation using an excess amount of Ce(IV) salt. The oxygen evolution was monitored in an airtight glass cell using an oxygen electrode as mentioned in chapter 3. The catalysis initiates within seconds after the addition of the primary oxidant Ce(IV). The $[(bpy)Ir^{III}(Cp^*)\text{-}OH_2]^{2+}$ and $[(phen)Ir^{III}(Cp^*)\text{-}OH_2]^{2+}$ complexes show a rapid initial rate for oxygen formation, faster than the bipyrimidine catalyst (Fig. 5.3). This nicely shows how aqua induction can shorten the initial lag time of this system. For the aqua bonded mono iridium complexes the rates are twice as high as for the halogen derivatives [26]. The oxygen evolution rate attains its maximum value within 1-2 minutes, and afterwards it starts to decrease slowly (Fig. 5.3).

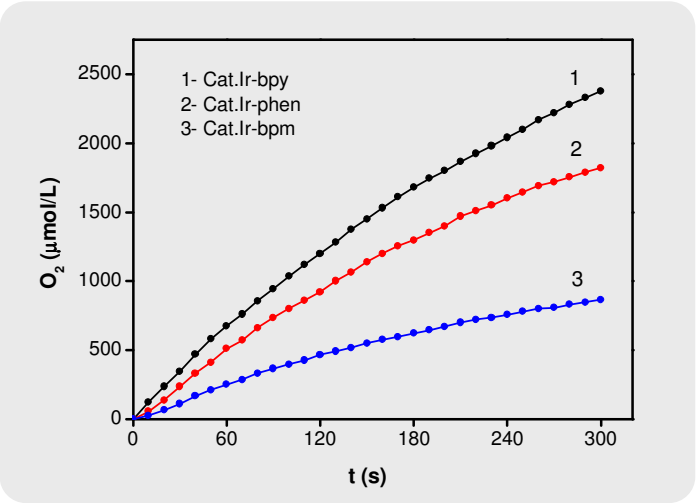

Figure 5.3. Initial oxygen evolution during homogeneous water oxidation catalyzed by (1) $[(bpy)Ir^{III}(Cp^*)\text{-}OH_2]^{2+}$, (2) $[(phen)Ir^{III}(Cp^*)\text{-}OH_2]^{2+}$ and (3) $[(bpm)Ir^{III}(Cp^*)\text{-}OH_2]^{2+}$ complexes in deoxygenated 0.1 M HNO_3 aqueous solutions in the presence of Ce(IV). (Catalysts concentration 25±0.2 µmol/L, Ce(IV) 50 mM).

Similar behaviour is also seen for $[(Cp^*)\text{-}Ir^{III}\text{-}(phpy)\text{-}Cl]^+$, $[(Cp^*)\text{-}Ir^{III}\text{-}(bpy)\text{-}Cl]^+$ and $[(Cp^*)\text{-}Ir^{III}\text{-}(bpy)\text{-}I]^+$ catalysts attributed to oxidation of the complex, including the possible degradation of the nitrogen ligand or the Cp* methyl groups. The TOF for Cat.**Ir**–bpy and Cat.**Ir**–phen is much higher than for the recently reported mono site iridium catalysts [26,29]. Table 5.1 shows a list of the TOF's measured for the first hour and the TON's obtained during five hours of catalysis operation for Cat.**Ir**–bpy, Cat.**Ir**–phen and Cat.**Ir**–bpm. The turnovers for all three systems are at least two times higher than for the fastest $[(bpy)Ir(Cp)\text{-}I]^+$ complex [26]. For prolonged water oxidation catalysis for 5 hours, $[(bpy)Ir^{III}(Cp^*)\text{-}OH_2]^{2+}$ shows a TON of 1500, which is much higher than the chloro and iodo analogues and confirms the increased durability of the catalysis process (Table 5.1). The initial rate of oxygen evolution for the aqua complexes $[(phen)Ir^{III}(Cp^*)\text{-}OH_2]^{2+}$ and $[(bpm)Ir^{III}(Cp^*)\text{-}OH_2]^{2+}$ is 21 and 11.2 min^{-1} respectively, also higher than for the chloro derivative (Table 5.1). It also shows a superior performance of the Ir complexes for homogeneous catalysis compared with the Ru catalysts discussed in chapter 3.

Table 5.1. Rates for oxygen generation and TON's for $[(bpy)Ir^{III}(Cp^*)\text{-}OH_2]^{2+}$, $[(phen)Ir^{III}(Cp^*)\text{-}OH_2]^{2+}$ and $[(bpm)Ir^{III}(Cp^*)\text{-}OH_2]^{2+}$ aqua complexes.

Catalyst	Rate $molO_2$ /(molCat · t)		TON[c] ($molO_2$/molCat)	*Ref.*
	(t.o.min^{-1})[a]	(t.o.hr^{-1})[b]		
Cat.**Ir**–bpy	27	419	>1500/5 hrs	*This work*
Cat.**Ir**–phen	21	301	>1045/5 hrs	*This work*
Cat.**Ir**–bpm	11.2	181	>781/5 hrs	*This work*
[(N-C)Ir(Cp*)-Cl	10	155	349/8 hrs	*26*
[(bpy)Ir(Cp*)-Cl]Cl	14.4	93	320/8 hrs	*26*
[(bpy)Ir(Cp)-I]NO_3	9.3	214	738/8 hrs	*26*
[(phen)Ir(Cp*)-Cl]Cl	8.4	–	–	*26*
[(bpm)Ir(Cp*)-Cl]Cl	3.9	–	–	*26*

[a] initial rate for the oxygen evolution measured for the first 5 minutes; [b] total turnovers (t.o.) obtained in the first hour of catalysis operation and [c] total turnover number obtained during 5 hours of the water oxidation reaction. Catalyst concentration 25±0.2 μmol/L, Ce(IV) 50 mM. The oxygen evolution was monitored *in situ* in an air-tight glass cell using a calibrated oxygen electrode connected to a digital oxy-meter in deoxygenated 0.1 M HNO_3 aqueous solutions.

5.2.3. Oxygen Evolution by Surface Anchored Mono-Iridium Catalysts

The current-potential behaviour of the ITO functionalized catalyst system shows the oxygen onset current wave above 1.5 V (vs. NHE), both in 0.1 M aqueous HNO_3 and in pH=7.35 buffer solutions (Fig. A5.4). This suggests that the rate limiting step is a non PCET mechanism that retains the water oxidation potential above 1.5 V even at higher pH. A polarization current wave appears at *ca*. 1.33 V (vs. NHE) in aqueous acids leading towards oxygen evolution currents (Fig. 5.4). It is followed by a broader reduction wave around 1.27 V during the reverse scan. On the other hand in neutral buffer solution, a polarization wave appears at ca. 0.9 V and is followed by a reversible and an irreversible reduction wave, while the onset of the oxygen current remains above 1.55 V vs. NHE (Fig. 5.4). The single wave in the acidic electrolyte can be assigned to the $[Ir^{IV}\text{-}(OH)]^{2+}/[Ir^{III}\text{-}(OH_2)]^{2+}$ and $[Ir^{V}(=O)]^{2+}/[Ir^{IV}\text{-}(OH)]^{2+}$ transitions occurring in a single step of simultaneous removal of two electrons and two protons which has been reported recently for the

ruthenium analogue $[(terpy)Ru^{II}(bpm)\text{-}OH_2]^{2+}$, where $[Ru^{III}\text{-}OH]^{2+}$ is a "missing" oxidation state [30]. Alternatively, two oxidations of the iridium centre $[Ir^{III}\text{-}OH_2]^{2+}$ can occur at almost the same energy, as described by Brudvig [26].

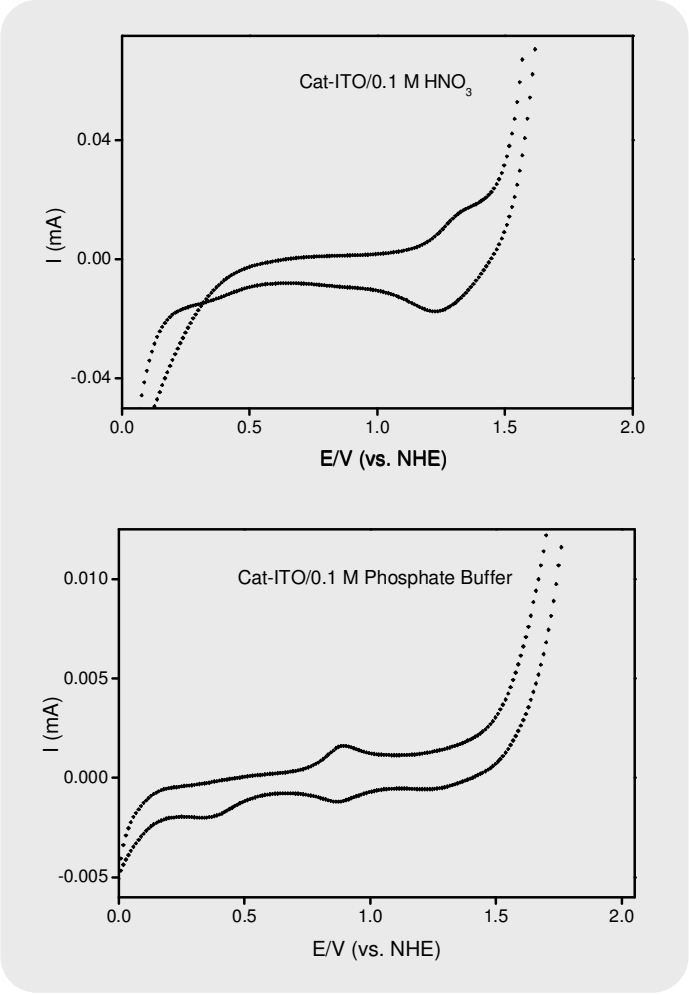

Figure 5.4. Expanded cyclic voltammetry for the $[(H_4dphbpy)\text{-}Ir^{III}\text{-}(Cp^*)]^{2+}$ complex anchored on an ITO electrode in deoxygenated aqueous **(top)** 0.1 M HNO_3 and **(bottom)** 0.1 M phosphate buffer solution (pH=7.35). (Scan rate 50 mV/sec, ITO area A= 1 cm^2).

Oxygen bubbles were also observed on the Cat-ITO working electrode during potential cycling in aqueous solution. The current does not grow by repeating the scans, indicating that there is no apparent electro-deposition of the catalyst or

oxides of iridium in the electrochemical conditions [17]. Following the CV experiments, the Cat.**Ir**–COOH and Cat.**Ir**–PO_3H_2 modified ITO electrodes were used to perform controlled potential catalytic water electrolysis experiments in aqueous solution. An electrolysis cell with separate anodic and cathodic compartments was employed to collect the oxygen and hydrogen as mentioned in the previous chapter. Oxygen evolution was monitored *in situ* with a calibrated oxygen electrode connected with a digital O_2 meter (YSI, Inc., Model 550A).

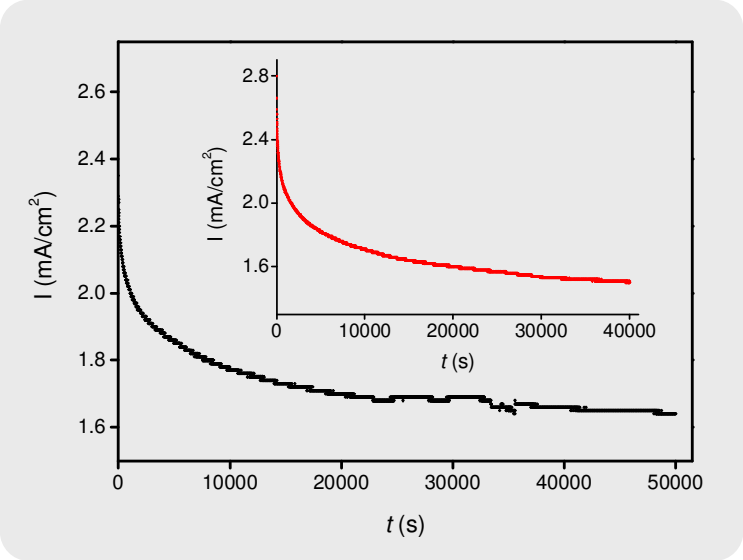

Figure 5.5. Controlled-potential water electrolysis with the Cat.**Ir**–PO_3H_2 modified ITO electrodes in deoxygenated aqueous 0.1 M pH=4 buffer solution, at *ca.* 1.75 V (vs. NHE). Inset shows electrolysis with the Cat.**Ir**–COOH modified ITO electrodes in deoxygenated aqueous solution under similar conditions at *ca.* 1.75 V (vs. NHE), ITO area A= 1 cm^2, (catalyst loading ~1.55–1.70 × 10^{-10} mol/cm^2).

Controlled-potential electrolysis of an aqueous solution with Cat.**Ir**–COOH and Cat.**Ir**–PO_3H_2 modified ITO electrodes were conducted at *ca.* 1.75 V (vs. NHE). Figure 5.5 shows the current-time plots for the catalytic water electrolysis at pH=4. The current densities at 1.75 V (vs. NHE) under steady state conditions were more than 1.61 mA/cm^2 and 1.67 mA/cm^2 for the Cat.**Ir**–COOH and Cat.**Ir**–PO_3H_2 modified ITO respectively. The oxygen generation current densities remain above

1.6 mA/cm^2 for several hours, both for Cat.**Ir**–COOH and for Cat.**Ir**–PO_3H_2 catalyst, and no significant decrease in the catalytic activity was observed. The initial average current densities related to the initial rate of oxygen generation were above >1.8 mA/cm^2 for Cat.**Ir**–PO_3H_2 and more than 1.7 mA/cm^2 for the Cat.**Ir**–COOH modified ITO systems (Fig. A5.5). As the potential is switched on, the oxygen bubble formation from the catalyst modified ITO started within seconds of the catalytic electrolysis operation.

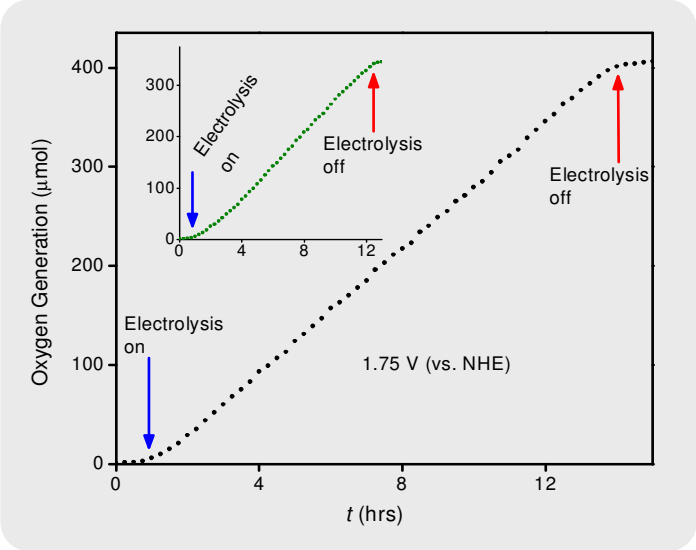

Figure 5.6. Oxygen generation (µmol) vs. time plot for the controlled-potential water electrolysis with Cat.**Ir**–PO_3H_2 modified ITO electrode and (inset) for Cat.**Ir**–COOH modified ITO electrode in deoxygenated aqueous 0.1 M buffer solution (pH=4) over an extended period of 14 hrs at *ca.* 1.75 V (vs. NHE). The blue arrows indicate the beginning of electrolysis and red arrows point to the termination. ITO area A=1 cm^2, (catalyst loading ~1.55–1.70 × 10^{-10} mol/cm^2 for Cat.**Ir**–PO_3H_2 and Cat.**Ir**–COOH).

An affluent stream of oxygen bubbles was leaving the catalyst modified ITO surface along with simultaneous hydrogen generation at the spiral Pt in the cathodic compartment during the electro-assisted catalysis. The Cat.**Ir**–PO_3H_2 modified ITO was found to be as efficient as the Ru based electrocatalytic systems for water electrolysis described in chapter 4, showing more than 1.65 mA/cm^2 oxygen generation current densities for 14 hours of uninterrupted electrolysis (Figs. 5.5-

5.6). In addition, the current densities for both catalytic systems are more than an order of magnitude larger than for the recently reported $–CH_2$-PO_3H_3 modified mono site ruthenium based electrocatalytic water splitting assemblies [13].

During controlled-potential electrolysis at pH=4, the Cat.**Ir**–PO_3H_2 modified ITO system generates more than 400 μmol of molecular oxygen in 13 hours of catalytic operation (Fig. 5.6). The electrolysis was undertaken at *ca.* 1.75 V (vs. NHE) with a stable current density (Fig. 5.5). A rich stream of oxygen is coming out of the Cat.**Ir**–PO_3H_2 modified ITO electrode at a rate of ~6.5 moles of oxygen per mole of catalyst per second. The catalytic system generates more than 2.1×10^5 turnovers for molecular oxygen in 13 hours. This implies that the surface bound iridium half sandwiched molecular catalyst Cat.**Ir**–PO_3H_2 exhibits a superior catalytic performance compared to the anodically deposited Cp*-Ir catalyst [23]. The Cat.**Ir**–COOH modified ITO electrode produces more than 300 μmol of molecular oxygen in 12 hours of controlled-potential electrolysis (inset Fig. 5.6). The current densities were only ~0.05 mA/cm^2 less than those for the Cat.**Ir**-PO_3H_2 modified ITO system at *ca.* 1.75 V potential (vs. NHE).

5.2.4. Water Oxidation and Oxygen Evolution Mechanism

It was recently described for $[(Cp^*)\text{-}Ir^{III}\text{-}(N–C)\text{-}OH_2]^+$ and $[(Cp^*)\text{-}Ir^{III}\text{-}(N–N)\text{-}OH_2]^{2+}$ complexes that the mono iridium-oxo species $[Ir^V{=}O)]^{n+}$ (n=1 for N–C and n=2 for N–N) are generated by two step oxidation of the $[Ir^{III}\text{-}(OH_2)]^{n+}$ with simultaneous proton removal. The important point is the O–O bond formation, possibly by the nucleophilic attack of a OH_2 molecule to the $[Ir^V{=}O)]^{n+}$ complex. At the same time, a proton is thought to leave from the arriving water molecule to make a hydroxide ion that enhances the nucleophilicity for the attack at the oxo complex [26]. The CV's presented in the above section (Fig. 5.4) point to a mechanism where, after the second aqua insertion, the next step of electron removal is not coupled with the proton transfer and *vice versa*, as the oxygen onset potential is not following the pH dependence according to the Nernst law.

Scheme 5.1. Proposed hexacyclic catalytic mechanism for electro-assisted water oxidation and dioxygen formation by the mono iridium $[(N–N)Ir^{III}(Cp^*)\text{-}OH_2]^{2+}$ complex derived from the electrochemistry measurements. Red and green arrows represent the four electron and proton removal events, respectively. The $[(Ir^{III}–O(OH)]^{+}$ and $[(Ir^{IV}–O(OH)]^{2+}$ complexes are generated via consecutive proton transfer and electron removal steps, respectively, on second water insertion. Path (2) is proceeded without the formation of the intermediate $[(Ir^{IV}–(OO)]^{2+}$ and makes a pentacycle reaction route.

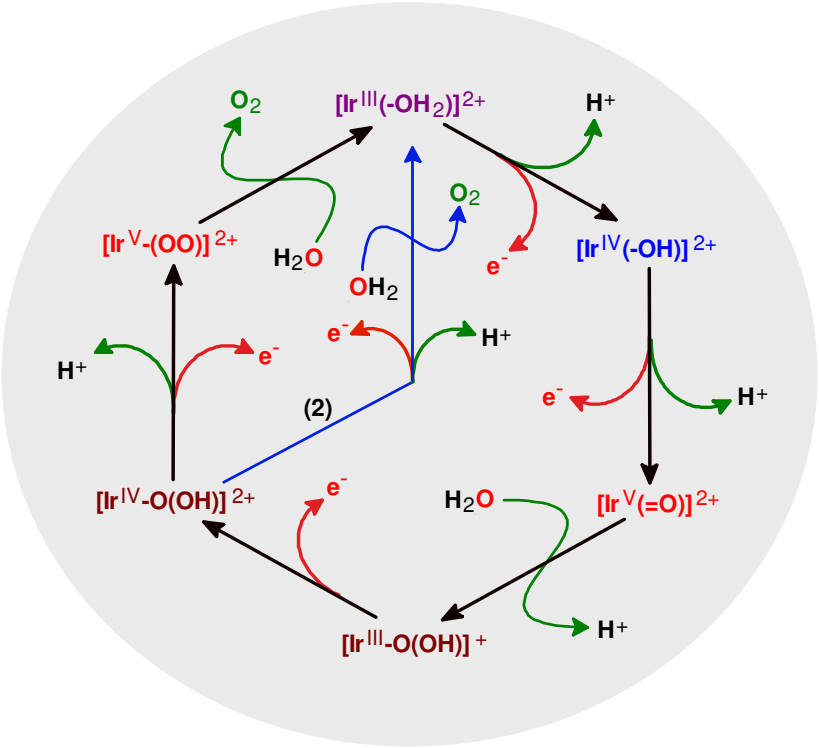

Probably a proton is removed during the second water insertion to the complex $[Ir^{V}=O)]^{n+}$ to generate a $[Ir^{III}–OOH)]^{n+}$ type intermediate with a charge n–1. This can lose two electrons and a proton and generate dioxygen while re-coordinating to another OH_2 to recharge the aqua complex for the next catalytic water oxidation cycle [26]. To enable the possibility of the electron and proton transfer in two steps, most likely the $[Ir^{III}–OOH)]^{n+}$ complex is formed by deprotonation accompanying the second aqua ligation of the complex. When this ejects an electron a $[Ir^{IV}–OOH)]^{n+1}$ type intermediate can be formed in the next step (Scheme 5.1). As the catalyst shows a fast rate for oxygen evolution, the OH_2 ligation may not be the

limiting factor. Most probably the small switchable Cp* provides space for a facile aqua insertion at the beginning of the second half of the water oxidation cycle. In the last step of the mechanism proposed in scheme 5.1, the fourth electron is removed along with a proton release with simultaneous water molecule insertion and dioxygen generation, thereby regenerating the $[Ir^{III}\text{-}(OH_2)]^{n+}$ complex for the next catalytic operation of water oxidation.

5.3. CONCLUSIONS

Stable and easy accessible mono iridium Cp* aqua catalysts $[(bpy)Ir^{III}(Cp^*)\text{-}OH_2]^{2+}$ (Cat.**Ir**–bpy), $[(phen)Ir^{III}(Cp^*)\text{-}OH_2]^{2+}$ (Cat.**Ir**–phen) and $[(bpm)Ir^{III}(Cp^*)\text{-}OH_2]^{2+}$ (Cat.**Ir**–bpm), are developed for homogeneous oxygen evolution. The catalysts avoid the initial lag time for water oxidation and show higher catalytic activity and rate during 5 hours operation than the chloro and iodo derivatives reported recently [26]. The linker modified iridium catalysts are electrocatalytically active and robust when tethered to an ITO electrode surface by anchoring groups (PO_3H_2 or COOH). Cat.**Ir**–PO_3H_2 and Cat.**Ir**–COOH modified ITO electrodes were able to generate molecular oxygen for more than 12 hours of operation without significant loss of activity during controlled-potential water electrolysis. The overall catalyst turnover numbers were more than 2.1×10^5 in 13 hours at a turnover rate of ~6.5 moles of oxygen per mole of catalyst per second. The initial average current densities were more than 1.7 mA/cm^2. This study helps to pave the way for photo-electrocatalytic devices with immobilized mono iridium complexes for future fuel generation from water splitting.

5.4. MATERIALS AND METHODS

Synthesis of the compounds, ligands and complexes was conducted in an argon/nitrogen atmosphere. ITO coated glass slides (10 cm × 2.5 cm), the iridium dimer $[IrCl_2(Cp^*)]_2$ and the ligands 2,2′-bipyridine (bpy) 2,2′-bipyrimidine (bpm), and 1,10-phenanthroline (phen) were obtained from Sigma-Aldrich Co., and used

as received. 4,4′-dicarboxylic acid-2,2′-bipyridine (H_2dcabpy) and 4,4′-diphosphonic acid-2,2′-bipyridine (H_4dphbpy) were obtained as described in chapters 4.

Solutions for electrochemical investigations were prepared in ultra-pure water (Millipore MilliQ® A10 gradient, 18.2 MΩ cm, 2–4 ppb total organic content). All electrochemical measurements were carried out in carefully Ar-purged deoxygenated aqueous solutions at room temperature. Cyclic voltammetry and controlled-potential water oxidation experiments are conducted in a three electrode configuration pyrex glass cell. The potentiostat, working, counter and reference electrodes are the same as described in chapters 3 and 4. The electrode preparation, degassing of the aqueous solution, catalyst loading on ITO slides and *in situ* oxygen measurement are the same as described in the previous chapter.

Synthesis

5.4.1. Chloro Complex [(bpy)Ir^{III}(Cp*)-Cl]Cl (**Ir**–bpy)

2,2′-bipyridine (bpy: 0.156 g, 1.0 mmol) in MeOH (10 mL) was added to a stirred mixture of $[IrCl_2(Cp^*)]_2$ dimer (0.399 g, 0.5 mmol) in ab. MeOH (15 mL). The mixture was further stirred for 1 hour at 40-45 °C. The solution was filtered with a sintered funnel of fine porosity and the solvent was evaporated under vacuum. The solid yellow complex [(bpy)Ir^{III}(Cp*)-Cl]Cl thus obtained was re-precipitated from acetone or MeOH by addition of ether/hexane. Yield 0.37 g, 66 %. ^{1}H NMR (CD_3OD, 295 K, δ ppm, *J* Hz): 8.99 (d, 2H, $H^{6,6'}{}_{bpy}$, *J* 5.41); 8.64 (d, 2H, $H^{3,3'}{}_{bpy}$, *J* 8.11); 8.28 (t, 2H, $H^{4,4'}{}_{bpy}$, *J* 7.92); 7.85 (t, 2H, $H^{5,5'}{}_{bpy}$, *J* 6.66); 1.72 (s, 15H, $CH_3{}^{1\text{-}5}{}_{Cp^*}$), Analysis found: C, 43.24%; H, 4.85%; N, 5.0%. Calculated: C, 43.24%; H, 4.35%; N, 5.04% for $C_{20}H_{24}N_2Ir_1Cl_2$ complex.

5.4.2. Chloro Complex [(phen)Ir^{III}(Cp*)-Cl]Cl (**Ir**–phen)

The bright yellow chloro complex [(phen)Ir^{III}(Cp*)-Cl]Cl was prepared in a similar manner as described above (section 5.4.1) using 1,10-phenanthroline (phen: 0.18 g, 1.0 mmol) instead of 2,2′-bipyridine. Yield 0.39 g, 67 %. ^{1}H NMR (CD_3OD, 295

K, δ ppm, *J* Hz): 9.37 (dd, 2H, $H^{2,9}{}_{phen}$, *J* 1.20, *J* 5.31); 8.87 (dd, 2H, $H^{4,7}{}_{phen}$, *J* 1.20, *J* 8.29); 8.28 (s, 2H, $H^{5,6}{}_{phen}$); 8.18 (dd, 2H, $H^{3,8}{}_{phen}$, *J* 5.25, *J* 8.73); 1.80 (s, 15H, $CH_3{}^{1\text{-}5}{}_{Cp^*}$), Analysis found: C, 43.52%; H, 4.47%; N, 4.71%. Calculated: C, 44.22%; H, 4.39%; N, 4.70% for $C_{22}H_{24}N_2Ir_1Cl_2.H_2O$ complex.

5.4.3. Chloro Complex [(bpm)Ir^{III}(Cp*)-Cl]Cl (**Ir**–bpm)

The yellow chloro complex [(bpm)Ir^{III}(Cp*)-Cl]Cl was prepared in similar manner as described above (section 5.4.1) using 2,2′-bipyrimidine (bpm: 0.158 g, 1.0 mmol) instead of 2,2′-bipyridine. Yield 0.31 g, 55 %. ^{1}H NMR (CD_3CN, 295 K, δ ppm, *J* Hz): 9.27 (dd, 2H, $H^{6,6'}{}_{bpm}$, *J* 2.03, *J* 4.85); 9.11 (dd, 2H, $H^{4,4'}{}_{bpm}$, *J* 2.03, *J* 5.85); 7.92 (t, 2H, $H^{5,5'}{}_{bpm}$, *J* 5.31); 1.70 (s, 15H, $CH_3{}^{1\text{-}5}{}_{Cp^*}$), Analysis found: C, 36.30%; H, 4.33%; N, 9.73%. Calculated: C, 37.56%; H, 4.20%; N, 9.73% for $C_{18}H_{22}N_4Ir_1Cl_2.H_2O$ complex.

5.4.4. Chloro complex [(H_2dcabpy)Ir^{III}(Cp*)Cl]Cl (**Ir**–COOH)

To a mixture of [Ir^{III}(Cp*)(Cl_2)]$_2$ dimer (0.399 g, 0.5 mmol) in ab. MeOH (15 mL) stirred for 15 minutes under argon, 4,4′-dicarboxylic acid-2,2′-bipyridine (H_2dcabpy: 0.244 g, 1.0 mmol) in 0.5 mL water containing NaOH (0.08 g, 2.0 mmol), was slowly added. The mixture was further stirred for 3 hours at 45-50 °C. The solution was cooled to room temperature and the pH was lowered to 1-2 by addition of 0.5 M HCl. The free ligand was filtered off and the solvent mixture was evaporated under vacuum. The solid yellow chloro complex [(H_2dcabpy)Ir^{III}(Cp*)Cl]Cl thus obtained was re-precipitated from MeOH or acetone by addition of ether/hexane. Yield 0.39 g, 61 %. ^{1}H NMR (CD_3OD, 295 K, δ ppm, *J* Hz): 8.99 (d, 2H, $H^{6,6'}{}_{dcabpy}$, *J* 5.79); 8.95 (s, 2H, $H^{3,3'}{}_{dcabpy}$); 8.17 (dd, 2H, $H^{5,5'}{}_{dcabpy}$, *J* 1.59, *J* 5.80); 1.71 (s, 15H, $CH_3{}^{1\text{-}5}{}_{Cp^*}$), Analysis found: C, 36.59%; H, 3.66%; N, 4.0%. Calculated: C, 37.88%; H, 4.33%; N, 4.02% for $C_{22}H_{24}N_2O_4Ir_1Cl_2.3H_2O$ complex.

5.4.5. Chloro complex [$(H_4$dphbpy$)Ir^{III}(Cp^*)Cl]Cl$ (**Ir**–PO_3H_2)

The chloro complex [$(H_4$dphbpy$)Ir^{III}(Cp^*)Cl]Cl$ was prepared in a similar manner as described above (section 5.4.4) using 4,4′-diphosphonic acid-2,2′-bipyridine (H_4dphbpy: 0.316 g, 1.0 mmol) in 0.5 mL water containing NaOH (0.16 g, 4.0 mmol) instead of 4,4'-dicarboxylic acid-2,2′-bipyridine. Yield 0.40 g, 56 %. ^{1}H NMR (CD_3OD, 295 K, δppm, J Hz): 9.02 (s, 2H, $H^{3,3'}{}_{dphbpy}$); 8.80 (d, 2H, $H^{6,6'}{}_{dphbpy}$, J 6.09); 8.08 (dd, 2H, $H^{5,5'}{}_{dphbpy}$, J 2.01, J 6.15); 1.72 (s, 15H, $CH_3{}^{1\text{-}5}{}_{Cp^*}$), Analysis found: C, 32.11%; H, 3.14%; N, 4.10%. Calculated: C, 33.57%; H, 3.66%; N, 3.92% for $C_{20}H_{26}N_2O_6P_2IrCl_2$ complex.

5.4.6. General Synthesis of the Catalyst Complexes:

The mono iridium chloro complexes $[(L)Ir^{III}(Cp^*)\text{-}Cl]^+$ were converted into aqua catalysts $[(L)Ir^{III}(Cp^*)\text{-}OH_2]^{2+}$ by stirring in a water methanol mixture (1:1) containing (2.1 mmol) silver nitrate or hexafluorophosphate salt for 35 minutes at 40-50 °C. The white precipitates were filtered off and the solvent mixture was evaporated under vacuum. The solid bright yellow aqua complexes $[(bpy)Ir^{III}(Cp^*)\text{-}OH_2]^{2+}$, $[(phen)Ir^{III}(Cp^*)\text{-}OH_2]^{2+}$, $[(bpm)Ir^{III}(Cp^*)\text{-}OH_2]^{2+}$ $[(H_2dcabpy)Ir^{III}(Cp^*)\text{-}OH_2]^{2+}$ and $[(H_4dphbpy)Ir^{III}(Cp^*)\text{-}OH_2]^{2+}$ thus obtained were recrystallized from MeOH or acetone by addition of ether/hexane. The aqua exchange was monitored by following the colour change of the solution from orange to yellow visually or by UV-Vis spectral investigation (Fig. A5.2).

REFERENCES

01- M. Calvin, *Science* **1974**, *184*, 375–381.

02- E. L. Lebeau, S. A. Adeyemi and T. J. Meyer, *Inorg. Chem.* **1998,** *37,* 6476–6484.

03- R. Rarnaraj, A. Kira and M. Kaneko, M. *Angew. Chem. Int. Ed. Engl*. **1986,** *25*, 1009–1011.

04- F. P. Rotzinger, S. Munavalli, P. Comte, J. K. Hurst, M. Graetzel, F.-J. Pern and A.J. Frank, *J. Am. Chem. Soc*. **1987**, *109*, 6619–6623.

05- J. Limburg, J. S. Vrettos, L. M. Liable-Sands, A. L. Rheingold, R. H. Crabtree and G.W. Brudvig, *Science* **1999**, *283*, 1524–1527.

06- J. K. Hurst, *Coord. Chem. Rev*. **2005**, *249*, 313–328.

07- J. P. McEvoy and G. W. Brudvig, *Chem. Rev*. **2006,** *106*, 4455–4483.

08- Y. Naruta, M. Sasayama and T. Sasaki, *Angew. Chem. Int. Ed*. **1994**, *33*, 1839–1841.

09- M. Yogi and K. Narita, *J. Am. Chem. Soc*. **2004**, *126*, 8084–8085.

10- X. Sala, I. Romero, M. Rodríguez, L. Escriche and Antoni Llobet, *Angew. Chem. Int. Ed. Engl*. **2009**, *48*, 2842–2852.

11- Z. Chen, J. J. Concepcion, J. W. Jurss and T. J. Meyer, *J. Am. Chem. Soc*. **2009**, *131*, 15580–15581.

12- L. Tong, L. Duan, Y. Xu, T. Privalov and L. Sun, *Angew. Chem. Int. Ed*. **2011**, *50*, 445–449.

13- S. W. Kohl, L. Weiner, L. Schwartsburd, L. Konstantinovski, L. J. W. Shimon, Y. Ben-David, M. A. Iron and D. Milstein. *Science* **2009**, *324*, 74–77.

14- N. D. McDaniel, F. J. Coughlin, L. L. Tinker and S. Bernhard, *J. Am. Chem. Soc*. **2008**, *130*, 210–217.

15- J. F. Hull, D. Balcells, J. D. Blakemore, C. D. Incarvito, O. Eisenstein, G. W. Brudvig and R. H. Crabtree, *J. Am. Chem. Soc*. **2009**, *131*, 8730–8731.

16- D. G. H. Hetterscheid and J. N. H. Reek, *Chem. Commun.* **2011**, *47*, 2712–2714.

17- R. Lalrempuia, N. D. McDaniel, H. Müller-Bunz, S. Bernhard and M. Albrecht, *Angew. Chem. Int. Ed*. **2010**, *49*, 9765–9768.

18- F. Liu, T. Cardolaccia, B. J. Hornstein, J. R. Schoonover and T. J. Meyer, *J. Am. Chem. Soc*. **2007**, *129*, 2446–2447.

19- J. Mola, E. Mas-Marza, X. Sala, I. Romero, M. Rodriguez, C. Viñas, T. Parella and A. Llobet, *Angew. Chem. Int. Ed*. **2008**, *47*, 5830–5832.

20- R. Zong and R. P. Thummel, *J. Am. Chem. Soc*. **2005**, *127*, 12802–12803.

21- T. Wada, K. Tsuge and K. Tanaka, *Angew. Chem. Int. Ed. Engl*. **2000**, *39*, 1479–1482.

22- J. J. Concepcion, J. W. Jurss, P. G. Hoertz and T. J. Meyer, *Angew. Chem. Int. Ed*. **2009**, *48*, 9473–9476.

23- J. D. Blakemore, N. D. Schley, G. W. Olack, C. D. Incarvito, G. W. Brudvig and R. H. Crabtree, *Chem. Sci*. **2011**, *2*, 94–98.

24- N. D. Schley, J. D. Blakemore, N. K. Subbaiyan, C. D. Incarvito, F. D'Souza, R. H. Crabtree and G. W. Brudvig, *J. Am. Chem. Soc.* **2011**, *133*, 10473–10481.

25- K. S. Joya and H. J. M. de Groot, *Netherlands Patent Application* no. 2005512, Oct., **2010**.

26- J. D. Blakemore, N. D. Schley, D. Balcells, J. F. Hull, G. W. Olack, C. D. Incarvito, O. Eisenstein, G. W. Brudvig and R. H. Crabtree, *J. Am. Chem. Soc*. **2010**, *132*, 16017–16029.

27- M. Yagi, E. Tomita and T. Kuwabara, *J. Electroanal. Chem*. **2005**, *579*, 83–88.

28- D. J. Wasylenko, C. Ganesamoorthy, M. A. Henderson, B. D. Koivisto, H. D. Osthoff and C. P. Berlinguette, *J. Am. Chem. Soc*. **2010**, *132*, 16094–16106.

29- A. Savini, G. Bellachioma, G. Ciancaleoni, C. Zuccaccia, D. Zuccaccia and A. Macchioni, *Chem. Commun.* **2010**, *46*, 9218–9219.

30- J. J. Concepcion, J. W. Jurss, J. L. Templeton and T. J. Meyer, *J. Am. Chem. Soc.* **2008**, *130*, 16462–16463.

Appendix A5

[(bpy)-Ir^{III}-(Cp*)Cl]Cl

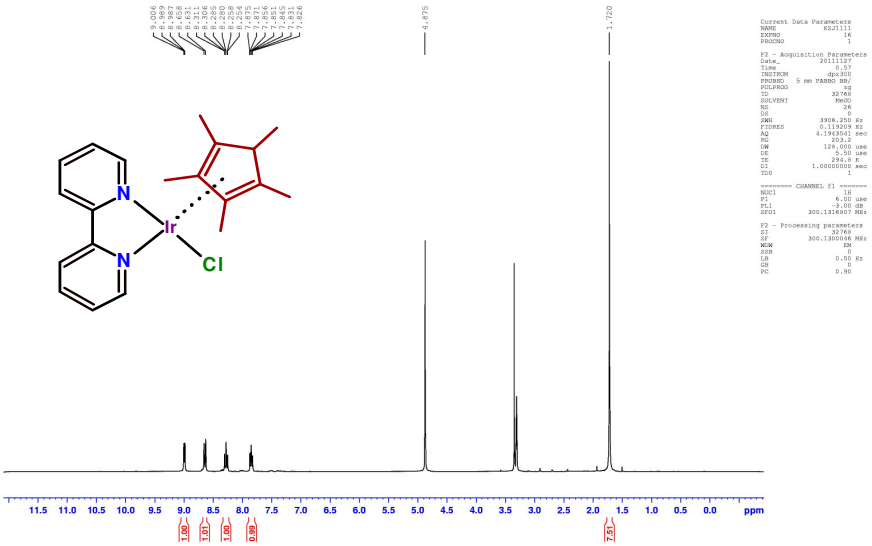

[(phen)-Ir^{III}-(Cp*)Cl]Cl

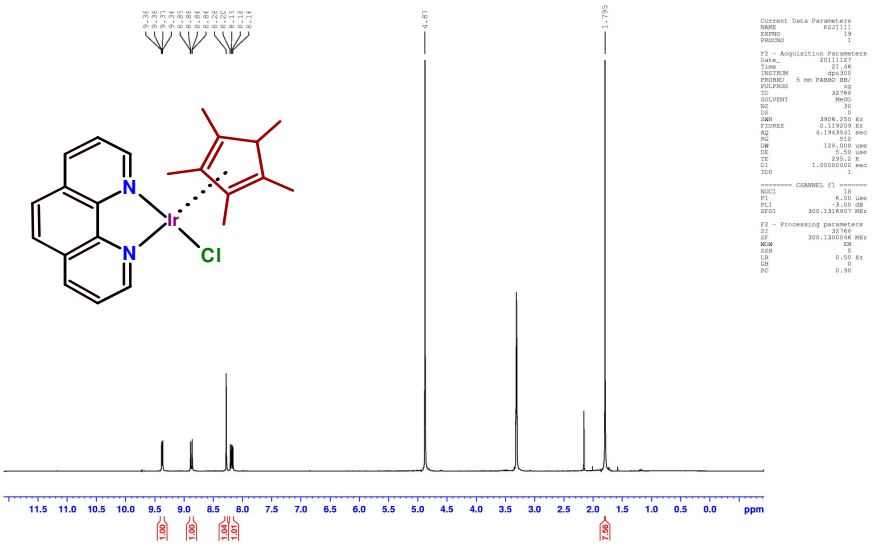

[(bpm)-Ir^{III}-(Cp*)Cl]Cl

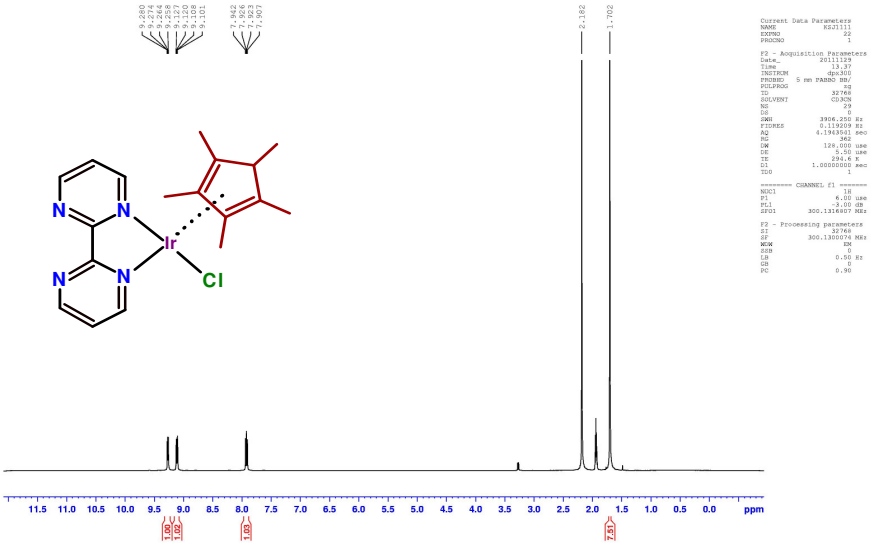

[{$(COOH)_2$-bpy}-Ir^{III}-(Cp*)Cl]Cl

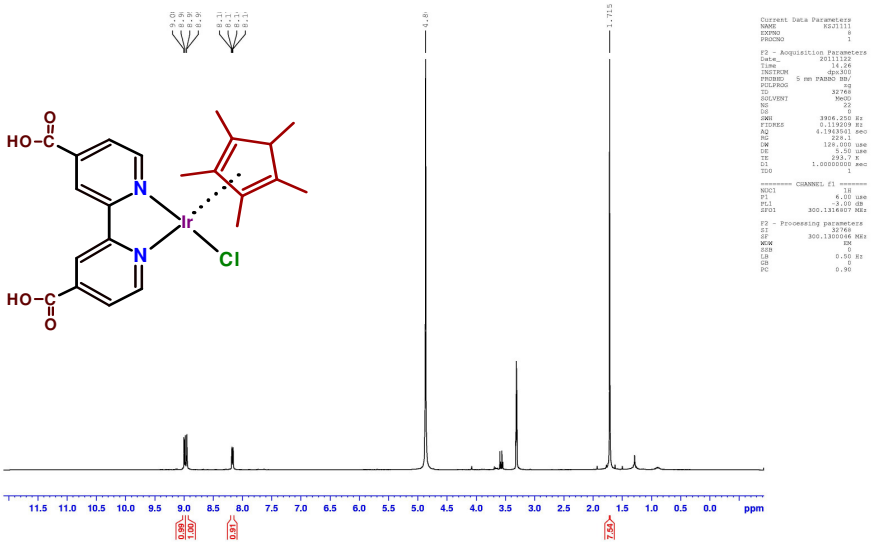

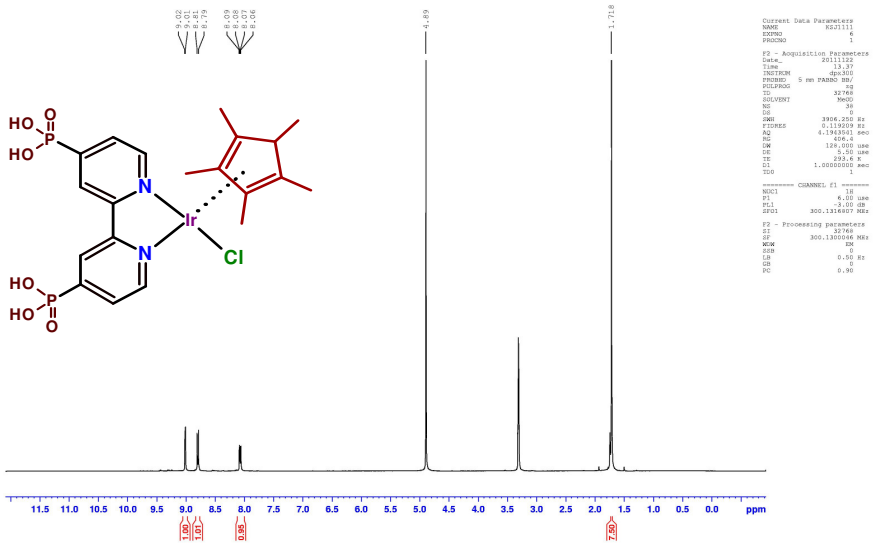

Figure A5.1. Proton NMR spectra of **Ir**-bpy, **Ir**-phen and **Ir**-bpm complexes and linker modified **Ir**-COOH and **Ir**-PO_3H_2 complexes.

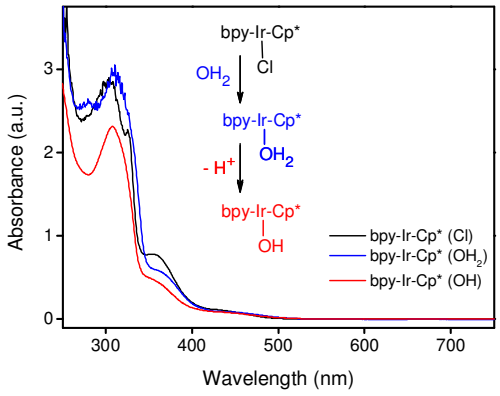

Figure A5.2. Electronic absorption spectra of $[(bpy)Ir(Cp^*)-(Cl)]^+$ complex (black line) following blue curve ascribed to the formation of aqua catalyst $[(bpy)Ru(cy)-(OH_2)]^{2+}$ induced by OH_2 exchange and deprotonation of the aqua catalyst to form $[(bpy)Ru(cy)-(OH)]^+$ complex (red line). For all measurements a concentration of the complex of 7.5×10^{-5} M was used.

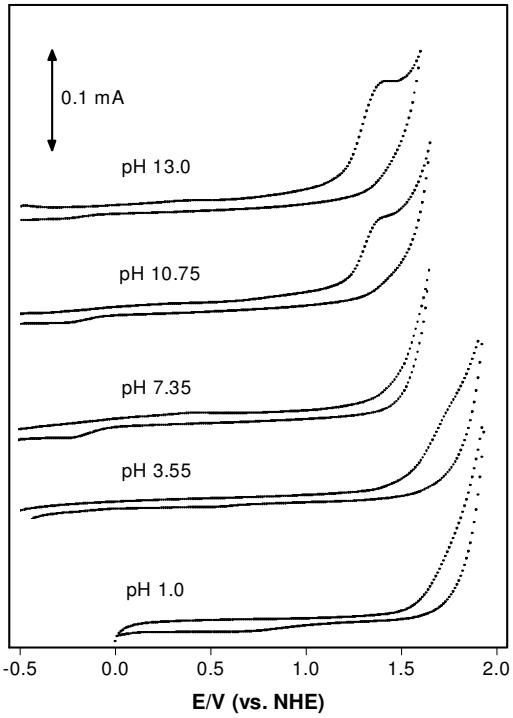

Figure A5.3. Cyclic voltammetry for $[(H_2dcabpy)\text{-}Ir^{III}(Cp^*)]^{2+}$ complex in 0.1 M deoxygenated aqueous solutions with different pH at glassy carbon disk working electrode (WE). Catalyst concentration was 2.5 mM in all experiments, scan rate was 50 mV/sec and the glassy carbon disk diameter was d=5mm.

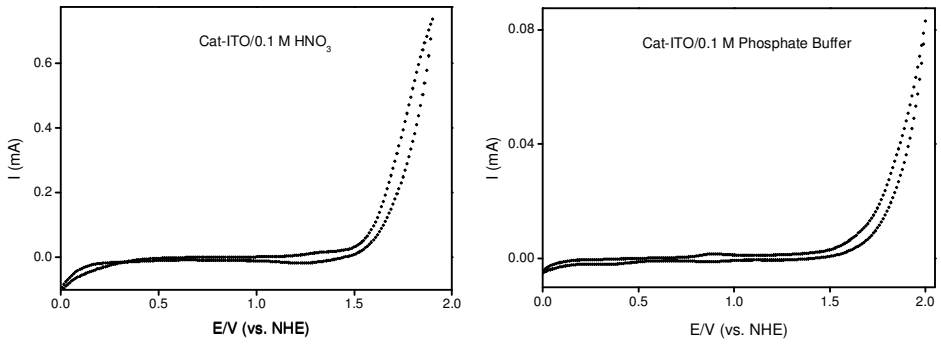

Figure A5.4. Cyclic voltammetry for the $[(L_2bpy)\text{-}Ir^{III}\text{-}(Cp^*)]^{2+}$ complex anchored on an ITO electrode in deoxygenated aqueous (left) 0.1 M HNO_3 (and) 0.1 M phosphate buffer solution pH ~ 7.35. (Scan rate: 50 mV/sec. ITO area A= 1 cm^2).

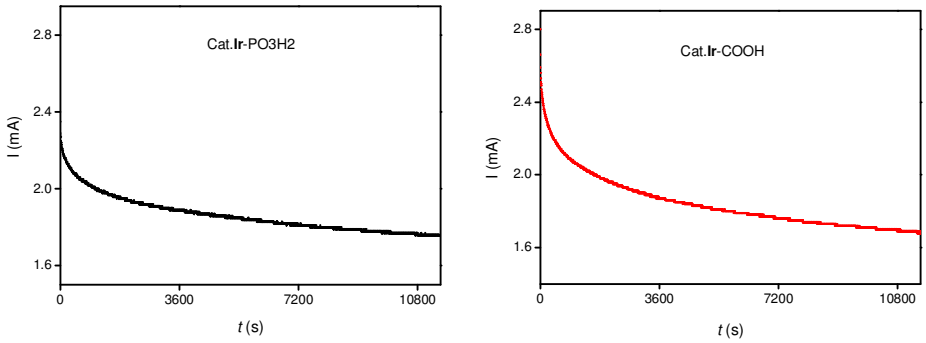

Figure A5.5. Initial oxygen evolution current (3 hrs) during controlled-potential water electrolysis with the (left) Cat.**Ir**–PO_3H_2 and (right) Cat.**Ir**–COOH modified ITO electrodes in deoxygenated buffer (pH=4) solution at *ca*. 1.75 V (vs. NHE), ITO area A=1 cm^2, (catalyst loading ~1.55–1.70 × 10^{-10} mol/cm^2), average initial current density >1.7 mA/cm^2.

Chapter 6

General Discussion and Outlook

ABSTRACT

The future perspectives of this research dissertation regarding water oxidation catalysis, oxygen evolving complexes and electro-assisted surface immobilized catalytic assemblies are presented in this chapter. A glance at my current work and upcoming research projects is described in section 6.2. Finally, the future outlook of water splitting catalysis by molecular complexes for stand alone solar to clean fuel conversion system is described along with integrated photo-electrochemical systems.

6.1. GENERAL DISCUSSION AND OUTLOOK

Being a young scientist, my enthusiasm has always been fueled by the desire to contribute something new for future energy supply and renewable materials. For this research work, my interest was focused on water splitting catalysis with the specific aim to contribute to the design, synthesis and testing of new molecular complexes for oxygen evolution, and full cell electrochemical water oxidation into molecular hydrogen and oxygen on surface immobilized catalytic assemblies. This chapter presents a number of novel opportunities that can be explored along this line, based on the results presented in the previous chapters.

6.2. FUTURE WORK

6.2.1. Dinuclear Complexes for Water Oxidation

One of the future directions worth studying would be the development of water oxidation catalysis with two iridium centers involved and the mechanism of O-O bond formation during the dioxygen generation process. In a first step to demonstrate the viability of this approach, some dinucleating nitrogen based ligands have been prepared that can accommodate two metal centers (Fig. 6.1). These ligands can also be extended with anchoring groups to implement electrochemical devices and photocatalytic systems.

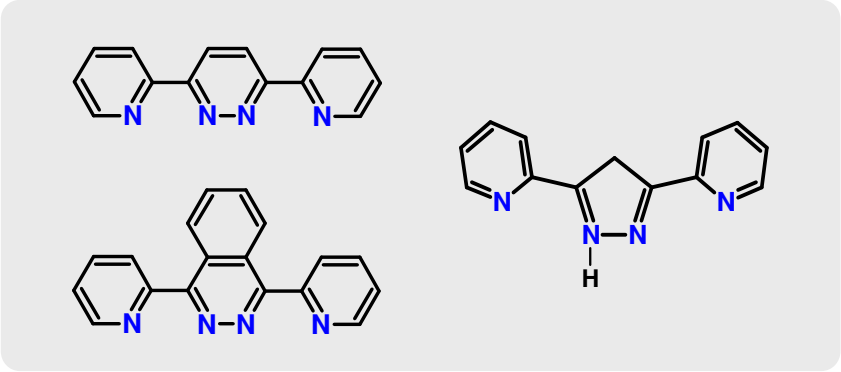

Figure 6.1. (left) A 3,6-bis(2-pyridyl)pyridazine, 3,6-bis(2-pyridyl)phthalazine, and **(right)** a Hbpp ligand [2,2′-(1H-pyrazole-3,5-diyl)bis(pyridine)] for dinuclear complexes.

6.2.2. Water Splitting via Tunneling Linker

Another avenue that can be explored is to introduce an alkyl tunneling barrier between the catalytic site and the electron sink (electrode) to increase the residence time of charge in the complex for enhanced catalysis. There are different ways to position alkyl chain modified catalyst molecules on a solid surface. In Fig. 6.2, an alkyl wire with a length of C_{12}-C_{19} is connected to the catalyst molecules while it has an electrode anchoring group on the other side of the chain. Since it is an insulating material, the alkyl layer provides a tunneling bridge that delays the backflow of electrons. This will also present a working model of a device that can modulate the rate of electron flow by adjusting the length of the alkyl chain [1].

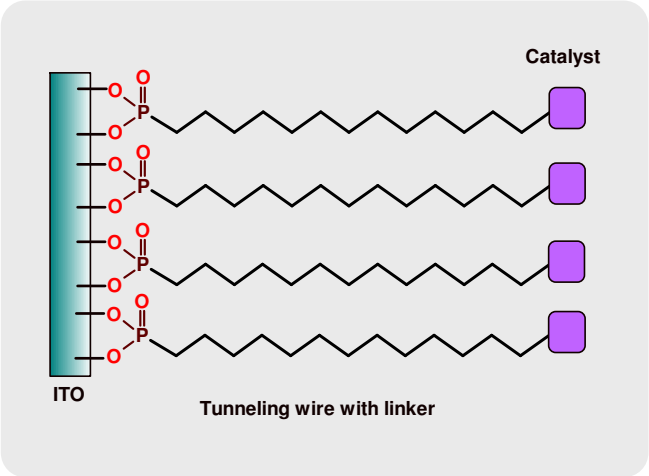

Figure 6.2. Alkyl chain with anchoring units modified catalyst-electrode assembly for electro-driven water splitting system.

6.2.3. Chromophore Sensitized Photo-Electrocatalytic Oxygen Evolving Assembly

Recently, it has been shown that a linker modified electrochemical water oxidation system can be extended with synthetic photo sensitizer molecules like Ru-$(bpy)_3$ (bpy is 2,2′-bipyridine) [2,3]. One difficulty for optimization is a very close proximity of the catalytic site to the photo harvesting molecule. Separating the two elements by a bridge or a tunneling barrier may enhance the performance of the light harvesting molecule by allowing it to act as an organometallic photovoltaic (PV) unit that can extract electrons from the catalyst when exposed to light. A chromophore sensitized catalytic assembly is under preparation and this line can be pursued for the development of a photo-electrocatalytic device system for light and electricity driven oxygen evolution in aqueous solution.

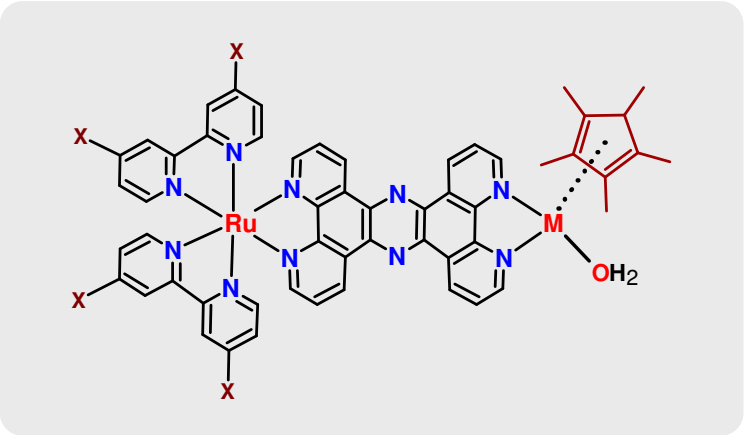

Figure 6.3. A chromophore sensitized water splitting catalyst for photo-electrocatalytic oxygen generation (X= COOH or PO_3H_2; M = Ru, Ir).

A Ru-$(bpy)_3$ type sensitizer with the mono ruthenium or iridium catalysts as shown in Figure 6.3, can be used in photoanode systems operating at moderate overpotential when exposed to visible light. The system may be integrated with a photocathode PV system with a hydrogen generation molecular catalyst or a thin layer of platinum.

6.2.4. The Artificial Leaf: Integrating Water Splitting Catalysts with a Multi-Junction Solar Cell

Recently, progress has been reported in the development of multi-junction solar cells with a thin coating of a water splitting catalyst [4,5]. Miller *et al*. reported that a composite oxide material coated on an ITO layer on a triple-junction silicon solar cell can operate at ~7.8 % efficiency for solar to hydrogen conversion and efficiencies of 4.7 % and 2.5 % were obtained recently with a cobalt phosphate catalyst, both in a wired and in a wireless configuration using a ternary alloy system at the cathode for proton reduction [6,7]. The corrosion protection of such PV based systems during water oxidation and oxygen evolution is an important issue to be addressed for future solar to fuel conversion applications.

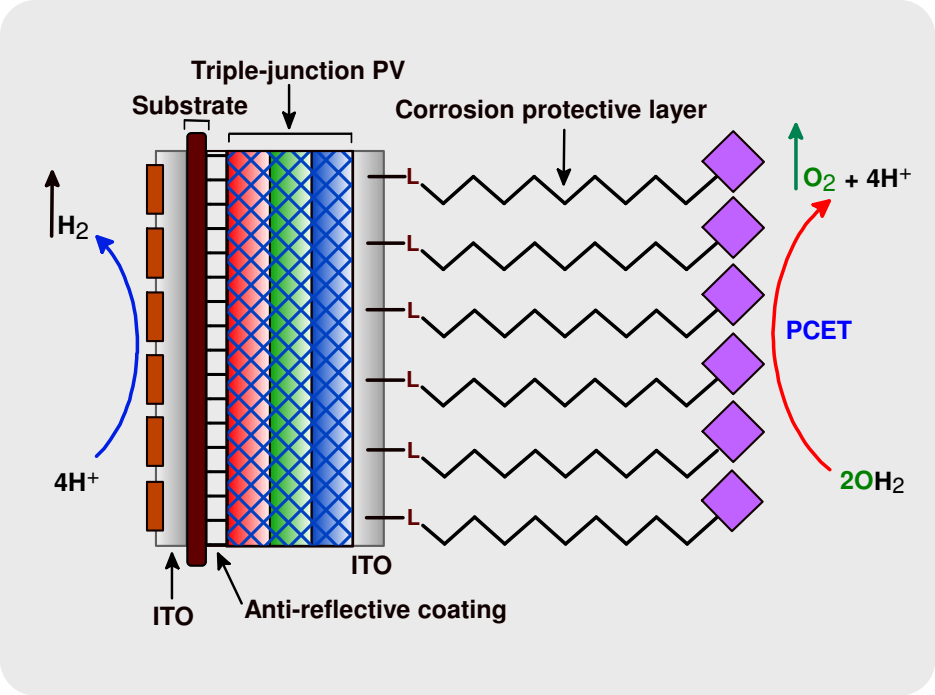

Figure 6.4. Water splitting catalysts can be attached to a molecular layer integrated with a Multi-Junction solar cell for corrosion protective coating/tunnelling bridge in Artificial Leaf configurations for stand-alone water oxidation and hydrogen production (L= COOH or PO_3H_2).

Another follow-up to the research presented in this thesis is the development of an integrated molecular system with a triple-junction solar cell, where the catalyst will be modified with a corrosion protective layer or anti corrosion coating for deposition on the PV surface, for photo-electrochemical water splitting. The other side of the device is wired or coated with hydrogen reduction catalysts or a thin platinum film for H_2 generation (Figure 6.4). Such photo-electrocatalytic devices are suitable for stand-alone applications, since they allow the conversion of sunlight to fuel using water as the raw material without the need for an external energy source.

This work is targeted to explore new materials and designs for the artificial man-made apparatus that makes use of natural resources like water and sun light for clean fuel production. The bottom line is that water splitting catalysis for solar to fuel conversion offers a potential alternative for future green energy supplies based on renewable materials. The electrochemical water splitting systems with molecular catalysts have potential application in *e.g.* rooftop devices to make personalized energy carriers. The proposed "Artificial Leaf" will soon be the future outcome of the present day technology and efforts in this field. Cheap and easy accessible hydrogen will not only serve as fuel for transportation but also as driving force for green power generation.

REFERENCES

01- C. C. Page, C. C. Moser, X. Chen and P. L. Dutton, *Nature* **1999**, *402*, 47–52.

02- Z. Chen, J. J. Concepcion, J. W. Jurss and T. J. Meyer, *J. Am. Chem. Soc.* **2009**, *131*, 15580–15581.

03- J. J. Concepcion, J. W. Jurss, P. G. Hoertz and T. J. Meyer, *Angew. Chem. Int. Ed.* **2009**, *48*, 9473–9476.

04- O. Khaselev and J. A. Turner, *Science* **1998**, *280*, 425–427.

05- M. G. Walter, E. L. Warren, J. R. McKone, S. W. Boettcher, Q. Mi, E. A. Santori and N. S. Lewis, *Chem. Rev.* **2010**, *110*, 6446–6473.

06- R. E. Rocheleau, E. L. Miller and A. Misra, *Energy & Fuels* **1998**, *12*, 3–10.

07- S. Y. Reece, J. A. Hamel, K. Sung, T. D. Jarvi, A. J. Esswein, J. J. H. Pijpers and D. G. Nocera, *Science* **2011**, DOI: 10.1126/science.1209816.

SUMMARY

The focus of this dissertation is the development of synthetic molecular water oxidation catalysts that are easily accessible and stable in light and moisture, with efficient oxygen generation capability at high rate in integrated electrochemical assemblies. While making hydrogen from water is important, it is not the only future target, since the protons released from water splitting could be effectively utilized in systems for CO_2 reduction into useful products and low carbon fuels like methanol and formic acid.

This research manuscript begins with ***Chapter 1*** that introduces the concept of the present and future global energy requirements, fossil based power supply, automotive transportation and its relation to the alarming level of carbon dioxide in the earth's atmosphere. The mechanism of water oxidation and a new model of the Mn_4CaO_x cluster in the PS-II is described that can be helpful in designing new synthetic molecular catalytic systems. The emphasis is on the revision of literature on evolutionary stages in the chemistry of water splitting by various kinds of molecular complexes. After a brief discussion of early research dealing with binuclear manganese and ruthenium complexes of dinitrogen ligands, this chapter describes the polypyridyl ligand based Ru and Mn complexes that were synthesized later in the 20^{th} century, along with a few mono nuclear analogues. This is followed by a view on electro-assisted water oxidation systems with immobilized molecular catalysts. The chapter concludes with summing up the challenges in the field and outlines the scope of the thesis and the structure of this research work.

Advanced electrochemical techniques for catalytic water oxidation studies, have been implemented on an existing tri-ruthenium catalyst and are presented in ***Chapter 2***. Oxygen formation at a Ru-red/Au_{disk} and detection by a platinum ring is investigated with a rotating ring-disk electrode assembly that was not used before for studying oxygen evolution by a molecular catalyst. The chapter also describes a successful application of *in situ* surface-enhanced Raman spectroscopy for catalyst transitions at the electrode-electrolyte interface and shows that the formation of

some type of oxide of metal during catalysis cannot be excluded. Finally, online electrochemical mass spectrometry analyses are applied that validate oxygen evolution for Ru-red adsorbed on the gold electrode.

After validating the electrochemical techniques, the next step of this project was to design and synthesize new bio-inspired water oxidation complexes containing a single catalytic site, aiming for a consecutive four-step proton coupled electron transfer (PCET) catalytic cycle for oxygen evolution. A new class of mononuclear ruthenium *p*-cymene derived half sandwiched aqua complexes with dinitrogen ligands for homogeneous catalysis is reported in ***Chapter 3***. The complexes are synthesized in good yield and purity by stirring the ingredients in an alkanol mixture at ambient temperature. The catalytic induction was performed with Ag salts in aqueous solution. Using an external catalyst activator, the molecular complexes show activity for water oxidation by generating a fair amount of TON's for molecular oxygen. Their electrochemistry reveals an important feature of following a four PCET step reaction coordinate, as evidenced by the pH dependent behaviour of the intermediates shown in the Pourbaix diagram (Figure 3.3). The catalysts undergo rapid aqua exchange in the catalyst induction step and facilitate the insertion of the second OH_2 without transforming into a higher oxidation state $[Ru^{V}(=O)]^{3+}$ complex.

The surface immobilized catalytic system derived from the mono ruthenium complexes for electrochemical water oxidation is discussed in ***Chapter 4***. The dinitrogen 2,2′-bipyridine ligand as mentioned in chapter 3, was modified with electrode linker groups like –COOH or $–PO_3H_2$ as anchoring sites for the indium-doped tin oxide (ITO) coated glass surface. The $[(L_2bpy)Ru^{II}(cy)\text{-}OH_2]^{2+}$ catalyst modified ITO assembly also shows a PCET behaviour in aqueous solution at pH up to 12. CV's obtained for oxygen evolution reveal the onset potential at *ca*. 1.45 V in neutral solution and >1.83 V (vs. NHE) for the acidic electrolytes. The controlled-potential water electro-splitting was conducted in deoxygenated solution revealing remarkable efficiency and stability under electrochemical conditions. During neutral water catalysis, more than 400 μmol of oxygen was produced in 11

hours with a current density >1.5 mA/cm^2. With a TOF of ~7.14 moles of oxygen per mole of catalyst per second, the catalyst turnovers were more than 3.1×10^5 in 12 hours. On the other hand, in aqueous acids, the turnover numbers were in excess of 6×10^5 in 35 hours at a rate of ~5.33 per second. More than 800 μmol of oxygen is generated in 30 hours with one cm^2 of ITO/Cat system at a current density of ~1.65 mA/cm^2. Further increase of the potential up to 2.20 V (vs. NHE) results in ~450 μmol of oxygen per hour in neutral water at a rate up to 80 mol O_2 per mol of catalyst per second, with a current density of >14 mA/cm^2. The investigation thus discloses a catalytic system with tremendously high turnover number at rapid rate of oxygen evolution for an electrochemical water oxidation assembly based on a single metal molecular oxygen evolving complex.

The next target of the project was to explore the mono-site iridium complexes for electrochemical water oxidation as these were not tested before on electrode surfaces. A homogeneous catalysis study was conducted with three aqua inducted iridium-Cp* complexes, $[(bpy)Ir^{III}(Cp^*)\text{-}OH_2]^{2+}$ (Cat.**Ir**–bpy), $[(phen)Ir^{III}(Cp^*)\text{-}OH_2]^{2+}$ (Cat.**Ir**–phen) and $[(bpm)Ir^{III}(Cp^*)\text{-}OH_2]^{2+}$ (Cat.**Ir**–bpm) as detailed in ***Chapter 5***. The study reveals that the $[(Cp^*)\text{-}Ir^{III}\text{-}(N\text{–}N)\text{-}OH_2]^{2+}$ catalysts are twice as efficient as their chloro analogues, reported earlier by another group. A pre-aqua insertion prevented the initial lag period. The iridium catalyst with bpy motif was also modified with –COOH and $–PO_3H_2$ units for immobilization at the inert oxide anode. The complexes Cat.**Ir**–PO_3H_2 and Cat.**Ir**–COOH on ITO generate molecular oxygen for several hours during controlled-potential water electrolysis. The overall catalyst turnover numbers were in excess of 2.1×10^5 in 12 hours at a turnover rate of ~6.5 moles of oxygen per mole of catalyst per second. The initial current densities were more than 1.7 mA/cm^2 and the system produces >350 μmol of molecular oxygen during half a day catalytic operation. This study is important to pave the way for photo-electrocatalytic systems with immobilized mono iridium complexes for water splitting and hydrogen generation.

To conclude, this thesis, entitled "Molecular Catalytic System for Efficient Water Splitting" provides an account of a class of mono catalytic centre molecular complexes for homogeneous water oxidation, as well as surface electrochemical oxygen evolving assemblies, based on ruthenium and iridium catalysts. It is anticipated that the study presented here introduces new possibilities for efficient and stable water splitting catalytic systems for clean fuel generation leading towards a greener energy technology and sustainable future.

SAMENVATTING
(SUMMARY IN DUTCH)

Het onderwerp van dit proefschrift is de ontwikkeling van synthetische moleculaire water oxidatie katalysatoren die gemakkelijk toegankelijk zijn en stabiel zijn in licht en vochtige omgevingen, met efficiënte en snelle zuurstofontwikkeling in geïntegreerde elektrochemische structuren. Ofschoon het maken van waterstof uit water belangrijk is, is dit niet het enige doel, omdat de protonen die vrijkomen bij het splitsen van water gebruikt kunnen worden in systemen voor CO_2 reductie naar nuttige producten en brandstoffen als methanol of mierenzuur.

In ***hoofdstuk 1*** wordt een overzicht gegeven van de essentiële stappen die in het verleden gemaakt zijn bij de ontwikkeling van moleculaire katalysatoren voor wateroxidatie op basis van ruthenium en mangaan, en worden deze kunstmatige systemen vergeleken met plant fotosysteem 2. Ook worden katalysatoren geadsorbeerd aan een electrode voor elektrochemische wateroxidatie beschreven. Het hoofdstuk eindigt met een opsomming van de uitdagingen in het veld en geeft een overzicht van het onderzoek beschreven in het proefschrift.

Geavanceerde technieken voor onderzoek van wateroxidatie worden gepresenteerd in ***hoofdstuk 2*** aan de hand van een modelstudie van een bestaande tri-ruthenium katalysator. Voor detectie van de zuurstofontwikkeling wordt gebruik gemaakt van een roterend ring disk systeem. Het hoofdstuk beschrijft ook hoe in-situ Surface Enhanced Raman Spectroscopy (SERS) gebruikt kan worden voor onderzoek van katalyse aan het grensvlak, tussen de katalysator en de oplossingsomgeving. Uit deze experimenten werd duidelijk dat de vorming van metaaloxiden niet kan worden uitgesloten. Vervolgens werd met online electrochemical mass spectrometry (OLEMS) de ontwikkeling van zuurstof gevalideerd.

De volgende stap in het onderzoek is het ontwerp en de synthese van nieuwe, van de natuur afgeleide complexen voor de oxidatie van water met een enkel katalytisch metaalion, die in staat zijn om het 4-staps proton gekoppeld elektron overdrachtsregime van het natuurlijke systeem te evenaren. ***Hoofdstuk 3*** beschrijft een nieuwe klasse van mononucleaire ruthenium paracymeen aqua complexen voor homogene katalyse met di-stikstof liganden. De complexen zijn eenvoudig te bereiden en zijn actief in oplossing. Elektrochemische metingen laten een pH-afhankelijkheid van de tussenproducten in het katalyse-proces zien in het Pourbaix diagram. De inductie van de katalysator met OH_2 verloopt snel, en gedurende de cycli wordt een tweede OH_2 opgenomen zonder dat het $Ru^{V}(=O)]^{3+}$ complex, in een hogere oxidatietoestand, gevormd wordt.

In ***hoofdstuk 4*** worden de complexen uit het vorige hoofdstuk bestudeerd na hechting aan een TiO2 elektrode oppervlak. De di-stikstof 2,2′-bipyridine ligand werd daartoe gemodificeerd met –COOH of $–PO_3H_2$ als linker groepen. Het $[(L_2bpy)Ru^{II}(cy)\text{-}OH_2]^{2+}$ (Cat.**Ru**–PO_3H_2 or Cat.**Ru**–COOH) katalysator gemodificeerde ITO oppervlak laat ook proton gekoppelde elektron overdracht zien, in waterige oplossing tot pH=12. Met cyclische voltammetrie worden water oxidatieve signalen bij 1.45 V in neutrale oplossing en bij 1.83 V in zuur milieu. De katalysator is opvallend stabiel, en produceert in neutrale oplossing meer dan 400 μmol zuurstof in 11 uur met een stroomdichtheid van meer dan1.5 mA/cm^2. Ook in zuur milieu worden goede resultaten waargenomen: meer dan 6×10^5 cycli in 35 uur, met een frequentie van ~ 5 per seconde. Meer dan 800 μmol zuurstof werd geproduceerd met een electrode van 1 cm^{-1} en een stroomdichtheid van ~1.65 mA/cm^2. Bij hogere potentialen worden katalyse frequenties tot 80 mol O_2 per mol katalysator per seconde waargenomen, met een stroomdichtheid >14 mA/cm^2. Dit onderzoek toont de ontdekking van een katalysator systeem met een enkele metaalpositie voor een snelle omzetting voor de oxidatie van water met hoge opbrengst.

In ***hoofdstuk 5*** wordt de ruthenium in het complex vervangen door iridium, worden de katalytische eigenschappen op de electrode van dit systeem onderzocht, en wordt de invloed van liganden op de katalysator eigenschappen in oplossing bestudeerd. Dit onderzoek laat zien dat de $[(Cp^*)\text{-}Ir^{III}\text{-}(N\text{–}N)\text{-}OH_2]^{2+}$ complexen twee keer zo efficiënt zijn als de chloro analoga bestudeerd in andere onderzoekslaboratoria, en dat pre-aqua activatie vertraging van het katalytische proces voorkomt. De Cat.**Ir**–PO_3H_2 of Cat.**Ir**–COOH op een ITO electrode genereren moleculaire zuurstof voor een aantal uren met de electrode op een vaste potentiaal in een elektrolyse opstelling. Meer dan 2.1×10^5 cycli in 12 uur werden gemeten, met een frequentie van ~6.5 mol zuurstof per mol katalysator per seconde. De stroomdichtheid aan het begin van het experiment was 1.7 mA/cm^2 en het systeem produceert >350 μmol zuurstof gedurende een halve dag. Dit onderzoek draagt bij aan het effenen van de weg naar foto-elektrolyse systemen met geïmmobiliseerde mono iridium complexen voor water oxidatie en waterstof productie.

Tot besluit, dit proefschrift, getiteld "Molecular Catalytic System for Efficient Water Splitting", geeft een weergave van het onderzoek dat geleid heeft tot een nieuwe klasse van moleculaire complexen voor homogene water oxidatieve en daarvan afgeleide heterogene complexe systemen voor elektrochemische splitsing van water, gebaseerd op ruthenium en iridium katalysatoren. Verwacht mag worden dat het onderzoek beschreven in dit proefschrift nieuwe mogelijkheden introduceert voor efficiënte en stabiele katalysatoren voor het splitsen van water voor de productie van schonen brandstof, op weg naar een groenere toekomst.

List of Publications/Patents

Patents:

Khurram Saleem Joya and Huub J.M. de Groot, Metal complex and use as multi-electron catalyst. *Netherlands Patent Application* no. 2005512, Oct., 2010.

Khurram Saleem Joya and Huub J.M. de Groot, Metal complex and use as multi-electron catalyst. *International Patent Application* no. PCT/NL2011/050673; Oct., 2011.

Publications:

1- K.S. Joya and H.J.M. de Groot, Electroassisted water splitting by single site half sandwiched molecular complexes anchored on the electrode surface via a tunneling barrier, *in preparation*.
2- K.S. Joya and H.J.M. de Groot, Rapid and efficient water oxidation by aqua induced mononuclear iridium complexes, *in preparation*.
3- K.S. Joya and H.J.M. de Groot, Surface enhanced electrocatalytic water splitting by single site iridium complexes, 2011, *submitted.*
4- K.S. Joya and H.J.M. de Groot, Biomimetic molecular water splitting catalysts for hydrogen generation. *Int J. Hydrogen Energy, 2011, in revision*.
5- K.S. Joya and H.J.M. de Groot, Molecular water oxidation catalysts with bifunctional aqua induction and proton management for a four step PCET pathway, *in preparation.*
6- K.S. Joya and H.J.M. de Groot, A mononuclear water splitting mimic of Photosystem-II with a four-step proton coupled electron transfer regime, 2011, *submitted.*
7- K.S. Joya and H.J.M. de Groot, Efficient water splitting by single site ruthenium catalyst. *Proceedings 4th European conference on chemistry and life sciences*, 2011, *submitted*.
8- K.S. Joya, H.J.M. de Groot and M.T.M. Koper, Rotating ring-disc electrode and surface enhanced raman spectroscopy studies of water splitting by trinuclear ruthenium catalyst adsorbed on gold, *to be submitted.*
9- J.L. Vallés-Pardo, M.C. Guijt, M. Iannuzzi, K.S. Joya, H.J.M. de Grout and F. Buda, Ab-initio molecular dynamics study of water oxidation reaction pathways in mono-Ru catalysts. *ChemPhysChem* 2011, *in press*.

Publications before PhD:

10- Y. Faheem and K.S. Joya, Phase transformation and freestanding nanoparticles formation in lead zirconate titanate derived by sol-gel. *Appl. Phys. Lett.,* 2007, *91*, 063115-1 – 06315-3.
11- M. Amjad and K.S. Joya, Electrochemical hydrogen evolution reactions on cobalt-molybdenum electrodes. *Pak. J. Sci. Res.,* 2007, *59* (1-2), 16–21.
12- K.S. Joya and F. Tahira, Synthesis of zeolite 4A molecular sieves from kaolin by clay mineral conversion process. *Pak. J. Sci. Res.*, 2007, *59* (1-2), 44–48.
13- K.S. Joya, M. Amjad, Y. Faheem and A. Siddiqa, Electrodegradation of 2-Chlorophenol at Modified Cylindrical Vitreous Carbon Electrode. *Pak. J. Sci. Res.,* 2007.
14- K.S. Joya, M. Amjad, Y. Faheem and S. Akhtar, Electrochemical oxidation of alkyl benzene sulfonate at modified platinum microdisk. *Pak. J. Sci. Res.,* 2007.
15- K.S. Joya, M. Amjad , M.A. Khurram and S. Waheed, Anodic polarization of Pb-Sb and Sn-Pb electrodes in sulphuric acid soluton. *Pak. J. Sci. Res.,* 2007.
16- K.S. Joya, M. Amjad and S. Waheed, Investigation of corrosion rate in certain alloys used for industrial cooling water system. *J. Pak. Inst. Chem. Engg.*, Vol. XXXIV 2007.

17- K.S. Joya, M. Amjad and A. Siddiqa, Study of various parameters involved in electrochemical machining of mild steel in sodium nitrate and sodium chloride electrolytes. *J. Pak. Inst. Chem. Engg*., Vol. XXXIV 2007.
18- M. Amjad and K.S. Joya, Effect of silver as an alloying additive on the anodic behaviour of lead dioxide electrode. *Pak. J. Sci.,* 2006, *58* (3-4), 79–83.
19- K.S. Joya, M. Amjad and A. Khurram, Comparative study on the anodic oxidation of normal butanol at Pb, Pb-Sb, Pb-Sn And Sn-Pb alloy electrodes. *Pak. J. Sci.,* 2006, *58* (3-4), 84–88.
20- K.S. Joya, M. Amjad and A. Sadia, Linear sweep voltammerty for electrochemical oxidation of alkyl benzene sulfonate in waste water. *Pak. J. Sci., Res*. 2006, *58* (3-4), 26–30.
21- K.S. Joya and M. Amjad, A comparative study on the anodic behaviour of arsenic and bismuth doped lead dioxide electrodes. *Pak. J. Sci. Res*., 2005, *57* (3-4), 104–108.
22- M. Amjad, K.S. Joya and U.A. Bilal, Electrochemical oxidation on PbO_2 electrodes electrodeposited from Cs^+ containing Pb^{++} electrolytes. *Pak. J. Sci. Res*., 2005, *57* (3-4), 159–162.
23- K.S. Joya, M. Amjad and Asif Ali, Investigation of oxidation processes at different Pb-Sb alloy anodes. *J. Pak. Inst. Chem. Engg*., 2004, *32*, 41–46.
24- M. Amjad and K.S. Joya, Anodic behaviour of antimony and arsenic doped lead dioxide electrodes. *J. Pak. Inst. Chem. Engg*., 2003, *32* (1-4), 43–46.

Curriculum Vitae

I, ***Khurram Saleem Joya***, the author of this dissertation, was born on 5th of January, 1979 in Lahore, Pakistan. While growing in a scientific family, I inherited interest and curiosity for science from my parents, especially from my Father. At the age of 8, I passed a junior school test and entered fourth class in 1987. After spending one and a half year at Govt. Muslim Model Junior School, I moved to the High School and passed my SSC/Matric. I was 14 when I got admission in Govt. Forman Christian (F.C.) College Lahore, and obtained my HSSC/FSc diploma in 1996. After this, I joined Govt. College (G.C.) Lahore, and did my graduation with Botany/Zoology/Chemistry combination, and obtained my BSc degree, in 1998. At the age of 19, I entered the Faculty of Chemistry of the University of Engineering and Technology (UET), Lahore, and got my MSc in Applied Chemistry in January, 2001. During my MSc research, I worked with Prof. Dr. M. Amjad on an electrochemistry project and developed new doping for PbO_x matrix for electro-oxidation of alkanols.

In February 2001, I joined the same department as a faculty member and became a regular Lecturer in Chemistry at UET, Lahore in December 2001. While continuing my teaching and research at UET, Lahore, I also obtained my M.Phil in Applied Chemistry in 2006 and did my research on Zeolite Molecular Sieves, Synthesis and Application, with Prof. Dr. F. Tahira. In the meantime, I also supervised six MSc research projects dealing with Electrochemistry, Electrochemical Machining (ECM), Zeolites and Corrosion Science, which resulted in 6 MSc theses and 9 publications. My early research in Pakistan has generated more than 15 research papers in local journals. During my professional carrier at UET, Lahore, I was also involved in many activities, such as: Proctoral Board, Library Committee, Tutorial Board and Guidance Bureau (2003-2007), elected member of UET Syndicate, Senate, Admission Cell (2004-2007), Head Sports, Tour, Functions Committee (Chemistry Department) (2002-2007).

In early 2007, I was granted with the HEC (Higher Education Commission) Pakistan, overseas PhD Scholarship and in September 2007, I started my PhD with Prof. Dr. H.J.M. de Groot (SSNMR) and Prof. Dr. M.T.M. Koper (CASC) at Leiden Institute of Chemistry, Leiden University, The Netherlands. While working on the water splitting project that is the

topic of the research in this thesis, I discovered a new class of oxygen evolving catalysts in 2010, and this invention has been filed as a Patent Application as well.

During my four years of PhD, I participated in various international and local conferences, courses and schools, where I presented my work. Among more than 20 meetings/conferences I have attended, the most important include: *NCCC IX* (2008), *XI* (2010) and *XII* (2011), and *Annual HRSMC Symposiums* (2008-2011) The Netherlands; *Solar-H2 Meeting*, 2008, Bochum, Germany; *Solar Fuels/Energy Meeting*, 2008, Berlin, Germany; *59th ISE Annual Meeting*, 2008, Seville, Spain; *International Conference Molecular Science for Solar Fuels*, 2009, Sigtuna, Sweden, *ISACS 2011: Challenges in Renewable Energy*, 2011, MIT, Boston, USA; *Photosynthesis Research for Sustainability*, 2011, Baku, Azerbaijan (Invited speaker); *Towards Global Artificial Photosynthesis, Energy, Nanochemistry & Governance*, 2011, Lord Howe Island, Australia (Invited plenary lecture); *4ECCLS*, 2011, Budapest, Hungary and *SolarFuelsTandem Meeting*, 2011, Mülheim, Germany.

I have also participated in *Solar-H2 Summer School*, 2008, Uppsala University, Sweden, and *EBSA Biophysics Course on Solar Energy - Biological and Biomimetic Solutions*, 2011, Szeged, Hungary. In 2009, I obtained two consecutive LUF grants from Leiden University and conducted two research internships in the group of Prof. Dr. J.S. Siegel at Institute of Organic Chemistry, University of Zürich, Switzerland. I was also invited for a practical demonstration of my catalytic water splitting system at the *BioSolar Cells (TBSC) Project Meeting*, 2011, Wageningen, The Netherlands.

Besides this, I joined Pakistan Tehreek-e-Insaf Holland Chapter (PTI-Holland) in 2010 and served as General Secretary and currently Vice President of the party.

Acknowledgments

It is important to realize that I would have never arrived at this point without the continuous educational support of many people, all my School and College teachers, who nourished me with knowledge and guidance. My university teachers showed me the beauty and wonders of science, in particular chemistry that has inspired me to do research in this field. It is worth mentioning the input of my MSc research supervisor Prof. Dr. Muhammad Amjad and Prof. Dr. Fazeelat Tahira during my MPhil project, for giving me a broader spectrum of research and confidence to explore new things in science and chemistry. My kind regards to Lt. Gen. (R) M. Akram Khan, vice chancellor University of Engineering and Technology (UET), Lahore for his interest in my PhD progress and the partial ownership of our Patent. The bold and steady steps taken by our ex-president Gen. Pervez Musharraf for the development of science and technology in Pakistan and for establishing the HEC (Higher Education Commission) are highly acknowledged. My sincere gratefulness to HEC for the overseas PhD scholarship and financial support for my four years stay in Netherlands.

I would like to mention my colleagues in the SSNMR group, our secretary Liesbeth van der Velden, members of CASC, MCBIM and Leiden University for their collaboration during my PhD research. I am very happy that Prof. Dr. Gijs A. van der Marel facilitated me in the organic synthesis lab and Dr. Rob van der Steen (LIC/Buchem B.V) for helping my students. I appreciate the useful discussions with Prof. Dr. Jan Reedijk, Dr. Francesco Buda, Dr. Partik Gamez and Dr. Sylvestre Bonnet during my work. Fons Lefeber and Cees Erkelens are acknowledged for their help in NMR measurements. Working with Dr. Reza Fallahpour at University of Zürich, Switzerland, was a good experimental experience for my initial learning of the polypyridyl compounds and heterocyclic synthesis. I also appreciate help of Michiel Cramwinkel and Art Bos for preparation and filing patent applications and suggestions of K.C. Daniël and Paul Hedges.

The community of HEC friends created a nice Pakistani MAHOL in Leiden. Nailah and Akram, Husnain and Masooma, Shoaib and Sadia, Lubna and Burhan, Shahbaz and Nadia, Shaukat and Neelam, Kamran and Mumtaz, Nadeem and Sonia, Khurshid and Rabia, Tariq and Sara, Subhan, Jahangir, Asghar, Qamar, Kashif, Faiza, Amer, Muzamal, Zakia, Yahya, Tayyab, Fraz, Imran, are being thanked for their hospitality, friendship and kindness. Manzoor (Hoofdorp), Idrees, Ilyaas and Ismail (Leiden), Ishaque (Utrecht), Zahid Butt (Nijmegen), Sohail Anjum (Utrecht), Sana (Delft), Dr. Akhtar Hussain (Eindhoven), Abdul Ghaffar (Amsterdam) and Ejaz ul Mohsin (Vienna, Austria) are highly indebted for their sincere wishes for my PhD research work and future.

Working in the laboratory has definitely become easier due to a nice and relaxing social environment and communication with special people: Nauman Javed (FCU Lahore), Dr. Umar Farooq Rizvi/Kalia (Lahore), M. Shahzad Yousaf/Sundar-Sundi (Gujranwala), Dr. Irfan Ashiq/Paa-G (Lahore), M. Farooq, M. Raza and Irfan Jajja (London, UK), Bilal Ahmad Farooqi (Islamabad), Frid ullah momin (Copenhagen, Denmark), Shahid Akram Javed (Sahiwal), Ahmad Raza, Masood and M.P. Sajid (Lahore), Majeed Ullah Niazi (Mianwali), Imran Qaisar (Sheikhupura). I value the friendship of Abubakar (Saudi Arabia), M. Fahad (Dubai), Kashif Ali Khan/Rook (UET, Lahore) and Ehsan Ullah/Cheunti (Boston, USA).

Faisal and Sarah Chaudhary (Canada), Ali and Rowida Marashdeh, M. Miqiyaas and Kinza and Mahmood (Leiden, The Netherlands) always had a kind attitude towards me and my family, and their hospitality and openness is highly commendable. Muhammad Hissi, Khaled and Taleb (Leiden, The Netherlands) were nice companions and gym-mates. The officials of Pakistan Tehreek-e-Insaf Holland Chapter (PTI-Holland), Dr. Gulsher Khaliq, Baber Bhatti, Bilal Ahmad, Ghulam Hussain and Rizwan Akhtar for gave me respect and trust, and I appreciate the optimistic thinking we have for the better future of Pakistan.

I lack words to express my infinite gratitude, feelings, regards, love and respect to my Parents. Thanks for your continuous prayers, love and care for me. My father, Dr. Abdul Khaliq Asim, is an amazing person, a great chemical scientist with excellent skills in technology and mechanics. I learned from him that a scientist is supposed to be a thinker and patient individual. My father is the head of Joya's home but the heart of our family is my Great Respectable Mother, Safia Rasheed. ***Ammi Gee***, I always miss the warmth, coziness, love, patience and gentleness, with which you nourish me. Dear Abbu Gee and Ammi Gee, I love both of you so much and may you live long with sound health and peaceful happy life, AMIN. My brothers Shams Kaleem and Dr. Yasir Faheem, and my sisters Shamsa, Saima and Sidra always gave me support, love and kind words during my PhD project. Javeria, Rimsha, Hassan, Husnain, Hamza, Abdul Ahad, Abdul Samad and little cute Hajira, I love you all.

In the end, I would like to express my thanks, regards and admiration to my lovely Wife Valeria/Lerochka and a lot of sparkling love to my little Darling KAREENA Janoo who is one of the most beautiful gifts I ever had. **شکریہ** Lera for your love, care and support, and for helping me and easing my life at home, so that I can work more and concentrate better on my research and thinking. You learnt to cook delicious food that made me a bit heavy man, "thanks" for this as well. Together with me, Lera and Kareena, we have a nice combination of chemistry, physics and naughtiness at our home in Boerhaavelaan 128.

اپنے والدین کے لیے لامحدود شکریہ، عزت، محبت اور احساسات کے اظہار کے لیے میرے پاس الفاظ نہیں ہیں میں کہنا چاہتا ہوں کہ آپ کی مسلسل دعاوں محبت اور دیکھ بھال کا بہت شکرگزار ہوں، میرے والد ڈاکٹر عبدالخالق عاصم ایک بہترین شخصیت، کیمائی سائنسدان ہیں اور میٹلکس اور ٹیکنالوجی میں بہترین مہارت رکھتے ہیں، مجھے اپنے والد سے معلوم ہوا کہ سائنسدان ایک مفکر اور بہترین صبر کرنے والے انسان ہوتے ہیں، میرے والد جو کیا گھر کے سربراہ ہیں لیکن میری والدہ ایک عظیم والدہ ہیں اور وہ ہی ہمارے گھر کا دل ہیں، امی جی میں ہمیشہ آپ کی گرم جوشی، پیار صبر اور محبت یاد کرتا ہوں، جس کے ساتھ آپ نے میری پرورش کی ہے، پیارے امی جی اور ابو جی میں آپ دونوں سے بہت پیار کرتا ہوں اور آپ کی لمبی عمر اور اچھی صحت کے لیے دعا گو ہوں، آمین

میرے بھائی Shams Kaleem اور Dr. Yasir Faheem اور میری بہنیں Shamsa, Saima and Sidra نے ہمیشہ میری حوصلہ افزائی کی اور میری PHD تحقیق کے دوران حمایت کی ہے، اس کے علاوہ Javeria, Rimsha, Hassan, Husnain, Hamza, Abdul Ahad, Abdul Samad اور میری چھوٹی سی پیاری سی Hajira میں تم سب سے بہت پیار کرتا ہوں،

آخر میں میں اپنی بیوی Valeria/Lerochka اور میری پیاری چھوٹی کرینہ جو میرے لیے سب سے خوبصورت تحفہ ہے میں شکرگزار ہوں جس کی محبت اور حمایت سے آج اس مقام تک پہنچا ہوں، جب سے تم میری زندگی میں آئی ہو میرے لیے بہت آسانی پیدا کر دی ہیں جس کی وجہ سے میں اپنی تحقیق میں پوری طرح توجہ دے سکا، اور اب تو تم بڑے لزیز کھانے پکانا جان چکی ہو شاید جس کی وجہ سے میں تھوڑا وزن بھی بڑھ گیا ہے، سب چیزوں کا بہت شکریہ، میں سمجھتا ہوں کہ ہماری فیملی کا زبردست کیمات، طبیعیات اور شرارت کا بہترین جوڑ ہے، جو کہ Boerhaavelaan 128 ہے،

Khurram Saleem Joya

2011, Leiden, The Netherlands